DEVELOPMENT AND KINETIC ANALYSIS OF COBALT GRADIENT FORMATION IN WC-Co COMPOSITES

by

Jun Guo

A dissertation submitted to the faculty of
The University of Utah
in partial fulfillment of the requirements for the degree of

Doctor of Philosophy

Department of Metallurgical Engineering

The University of Utah

August 2011

Copyright© Jun Guo 2011

All Rights Reserved

The University of Utah Graduate School

STATEMENT OF DISSERTATION APPROVAL

The dissertation of **Jun Guo**

has been approved by the following supervisory committee members:

Zhigang Zak Fang	, Chair	**4/21/2011** Date Approved
Hong Yong Sohn	, Member	**4/21/2011** Date Approved
Ravi Chandran	, Member	**4/21/2011** Date Approved
Sivaraman Guruswamy	, Member	**4/21/2011** Date Approved
J. Daniel Belnap	, Member	**4/21/2011** Date Approved

and by **Jan D. Miller** , Chair of the Department of **Metallurgical Engineering**

and by Charles A. Wight, Dean of The Graduate School.

ABSTRACT

Functionally graded cemented tungsten carbide (FG WC-Co) is one of the main research directions in the field of WC-Co over decades. Although it has long been recognized that FG WC-Co could outperform conventional homogeneous WC-Co owing to its potentially superior combinations of mechanical properties, until recently there has been a lack of effective and economical methods to make such materials. The lack of the technology has prevented the manufacturing and industrial applications of FG WC-Co from becoming a reality.

This dissertation is a comprehensive study of an innovative atmosphere heat treatment process for producing FG WC-Co with a surface cobalt compositional gradient. The process exploited a triple phase field in W-C-Co phase diagram among three phases (solid WC, solid Co, and liquid Co) and the dependence of the migration of liquid Co on temperature and carbon content. WC-Co with a graded surface cobalt composition can be achieved by controlling the diffusion of carbon transported from atmosphere during sintering or during postsintering heat treatment. The feasibility of the process was validated by the successful preparations of FG WC-Co via both carburization and decarburization process following conventional liquid phase sintering.

A study of the carburization process was undertaken to further understand and quantitatively modeled this process. The effects of key processing parameters (including heat treating temperature, atmosphere, and time) and key materials variables (involving

Co content, WC grain size, and addition of grain growth inhibitors) on the formation of Co gradients were examined. Moreover, a carbon-diffusion controlled kinetic model was developed for simulating the formation of the gradient during the process. The parameters involved in this model were determined by thermodynamic calculations and regression-fit of simulation results with experimental data.

In summary, this research first demonstrated the principle of the approach. Second, a model was developed to predict the gradients produced by the carbon-controlled atmosphere heat treatment process, which is useful for manufacturing WC-Co with designed gradients. FG WC-Co materials produced using this method are expected to exhibit superior performance in many applications and to have a profound impact on the manufacturing industries that use tungsten carbide tools.

TABLE OF CONTENTS

LIST OF TABLES

LIST OF FIGURES

ACKNOWLEDGMENTS

I would like to thank all those who made it possible for me successfully complete my doctoral study.

First of all, I would like to express my sincere appreciation to my advisor, Prof. Zhigang Zak Fang, for his expert guidance, encouragement and continuous support throughout the Ph.D study. I would also like to acknowledge many valuable discussions with Prof. Hong Young Sohn and Dr. Peng Fan and their expertise and insight on this research. Special thanks go to my thesis committee members, Prof. Ravi Chandran, Prof. Sivaraman Guruswamy, and Dr. Dan Belnap, for their assistance and review of this dissertation.

Second, I would like to thank all the colleagues in the laboratory of Prof. Fang. In particular, I would like to thank Dr. Haibo Zhang and Kyu Sup Hwang, who helped and inspired me during the course of this study.

Last but not the least, I would like to express my deepest gratitude to my husband Xu Wang, my parents and all my family for their endless love and support. This dissertation would have been simply impossible without them.

Finally, financial support from US DOE, Utah State COE program, National science foundation, and industrial companies is greatly acknowledged.

CHAPTER 1

INTRODUCTION

1.1 Background

Cemented tungsten carbide (WC-Co), one of the most widely used industrial tool materials, consists of a high volume fractions of tungsten carbide (WC) particles embedded in cobalt (Co) binder [1, 2]. The compatibility between the hard WC grains and the ductile Co binder phase renders the composite to have unique and superior combinations of mechanical properties including high modulus, high hardness, high wear resistance and moderate fracture toughness. These mechanical properties make WC-Co materials indispensable for a variety of manufacturing industries such as metal cutting, gas and oil drilling, mining, construction, and other applications requiring extreme wear resistance.

The applications of cemented tungsten carbide are limited by its relatively low fracture toughness. Typically the wear resistance and the fracture toughness of conventional WC-Co materials are inversely related to each other. In other words, the fracture toughness is improved at the expense of decrease in hardness and wear resistance, and vice versa. Functionally graded WC-Co (FG WC-Co) provides a viable solution to the trade-off between the wear resistance and fracture toughness by tailoring Co content and/or WC grain size within the microstructure. For example, a WC-Co with lower cobalt content near surface and higher cobalt content in the core provides FG WC-Co with

characteristics of hard-surface-tough-core structure [3-5]. Such a hard-surface-tough-core structure combines high wear resistance and high fracture toughness in a single component giving rise to significant performance gains in comparison to homogeneous WC-Co materials [6].

Because of the potential advantages of FG WC-Co, there has been considerable research on means for manufacturing WC-Co with microstructure gradients [7-24]. The different methods for producing FG WC-Co can usually be divided into two classes: “Powder Consolidation Process” and “Atmosphere Heat Treatment Process”. In the first class of processes, the gradient is built based on the use of powders of different compositions of either cobalt, or grain size, or carbon, or a combination of them in a powder compact and then the powder compact is consolidated/sintered to full density [9, 12]. As there is a variety of methods available for producing powder compacts with gradients, such as die compaction, injection molding, electrophoretic deposition, and tape casting etc. [9, 12, 13, 16, 21], the powder consolidation process is commonly used to make FG WC-Co. Yet the consolidation of FG WC-Co still has many technical or economical challenges. Typically WC-Co is consolidated via a liquid phase sintering process. Although the liquid phase sintering is very economical for producing homogeneous WC-Co materials, it is hard when employing it for manufacturing WC-Co with graded cobalt composition primarily because the liquid Co phase will homogenize through migration during the liquid phase sintering process. A solution to this homogenization problem is to employ high-pressure-assisted solid state sintering processes. During the solid state sintering, since there is no liquid phase formed and hence no risk of the migration of the liquid, the gradient structure may be preserved.

Unfortunately, these high-pressure-assisted solid state sintering techniques have limited industrial applications either because they are very expensive or because they fail to produce materials with desirable properties.

Distinguished from the first class of the processing methods for making FG WC-Co, the "Atmosphere Heat Treatment Process" relies on natural phenomenon of mass transport to create compositional gradients in WC-Co components by controlling atmospheres during sintering or post-sintering heat treatment. An example is the method for manufacturing the so-called dual phase (DP) carbides. According to the process developed by Fisher et al. [3-5], DP carbides can be prepared by heat-treating pre-sintered η-phase-containing WC-Co specimens in a carburizing atmosphere. As a result of the carburization heat treatment, the surface layer is characterized by a very low surface cobalt content rising with depth into the material. Beyond the surface layer, the core still contains η-phase. Since the brittle η-phase is usually considered detrimental to the mechanical properties of WC-Co composites [25, 26], it is desirable for many applications using such graded WC-Co materials without η-phase. To completely remove η-phase using the DP carbides process as described above, however, it requires a long heat treatment time at the liquid phase sintering temperature, which may eliminate the Co gradient, and may also be economically unfeasible.

Among the many available methods for manufacturing functionally graded WC-Co composites, liquid phase sintering remains the most economically viable option if the problem of the gradient homogenization due to the migration of liquid phase can be overcome. In order to maintain the gradient in the sintered WC-Co composite, the theories behind the liquid migration phenomenon need to be understood. Fang et al. [27-

35] found that the migration of liquid phase in the WC-Co system depends on three key factors: difference in the volume fraction of liquid Co, difference in grain size, and difference in carbon content. In general, liquid phase tends to migrate from regions with higher volume fraction of liquid phase to regions with lower fraction of liquid phase, from regions with coarser grain size to regions with finer grain size, and from regions with higher carbon content to regions with lower carbon content. Although the fundamental principles of the liquid migration phenomenon are now understood, the manufacturing of FG WC-Co remains a challenge. To date, the process that could be applied to manufacture FG WC-Co in a cost effective fashion on an industrial scale is still lacking.

1.2 Research Scope, Hypothesis and Objectives

The main objective of this research is to study the innovative process that is used for manufacturing functionally graded WC-Co materials with desirable gradient microstructures. Compared with the exiting technologies, the new process is more versatile and economic. Based upon the principles of liquid migration and the thermodynamic equilibrium of WC-Co system, it is hypothesized that functionally graded WC-Co that has a surface with reduced/enriched cobalt content can be created as a result of a surface carburization/decarburization heat treatment. Experiments should be conducted to demonstrate the feasibility of the proposed concept. Further experimental and theoretical studies should be carried out to grain a comprehensive understanding of the process.

The objectives for this research are summarized as follows:

1. Design a process based on the theories of the liquid migration and the thermodynamic equilibrium of the W-C-Co system.
2. Study the principle of the new process for forming Co gradient in WC-Co composites.
3. Experimentally investigate the effects of various process parameters and material variables on the formation of gradients during the carburization process. The process parameters include temperature, atmosphere, and length of heat treating time. The material parameters include Co content, WC grain size, and addition of grain growth inhibitors.
4. Theoretically model and simulate the kinetics of the gradient formation during the carburization process to predict the formation of the gradient structure as function of various process and material parameters.

1.3 References

[1] Fang Z. ASM Handbook. Materials Park: ASM International; 1998.

[2] Upadhyaya GS. Cemented Tungsten Carbides - Production, Properties, and Testing. New Jersey: Noyes; 1998.

[3] Fischer UKR, Hartzell ET, Akerman J. US Patent No.4743515, 1988.

[4] Fischer UKR, Hartzell ET, Akerman J. US Patent No.4820482, 1989.

[5] Akerman J, Fischer UKR, Hartzell ET. US Patent No.5453241, 1995.

[6] Metal Powder Report 1992;47:48.

[7] Taniguchi Y, Sasaki K, Ueki M, Kobori K. US Patent No.4830930, 1989.

[8] Okada Y, Sugawara J. US Patent No.5106674, 1992.

[9] Colin C, Durant L, Favrot N, Besson J, Barbier G, Delannay F. Int J Refract Met H 1993;12:145.

[10] Nakano M, Nomura T. US Patent No.5283030, 1994.

[11] Favrot N, Colin C, Besson J, Barbier G, Delannay F. 3rd International Symposium on Structural and Functional Gradient Materials, Switzerland. 1995. p.555.

[12] Greenfield MS. US Patent No.5623723, 1997.

[13] Put S, Vleugels J, Van der Biest O. Scripta Mater 2001;45:1139.

[14] Cheng JG, Wu YC, Xia YH. Mater Sci Forum 2003;423-425:45.

[15] Mirchandani PK, Keller BA. US Patent No.6511265, 2003.

[16] Tokita M. Mater Sci Forum 2003;423-425:39.

[17] Wei L, Xinde B, Yunhan L, Zuozhong J, Zhipeng X. Mater Sci Forum 2003;423-425:55.

[18] Colin M, Norgren S. Proceedings of the 16th international Plansee seminar, Metallwerk Plansee, Reutte, Austria. 2005.

[19] Yang JG, Wang HB, Liu Y, Huang BY, Zhang WZ. Journal of Central South University 2005;36:349.

[20] Matula G, Dobrzanki LA, Dozanska B. Int J Mater Prod Tec 2008;33:280.

[21] Li T, Li QF, Fuh JYH, Yu PC, Lu L. Int J Refract Met H 2009;27:95.

[22] Rassbach S, Moseley S, Bohlke S. Proceedings of the 17th international Plansee seminar, Metallwerk Plansee, Reutte, Austria, vol. 2. 2009. p.HM48/1.

[23] Konyashin I, Hlawatschek S, Ries B, Lachmann F, Sologubenko A, Weirich T. Int J Refract Met H 2010;28:228.

[24] Sorlier E, Colin C, Dourfaye A. Adv Mater Res 2010;83-86:810.

[25] Bolton D, Keely RJ. Int J Refract Met H 1982;1:103.

[26] Cho KH, Lee JW, Chung IS. Switzerland, vol. A209. 1996. p.298.

[27] Fang ZZ, Eso OO. Scripta Mater 2005;52:785.

[28] Eso OO, Fang ZZ, Griffo A. Int J Refract Met H 2005;23:233.

[29] Eso OO, Fang ZZ, Griffo A. Int J Refract Met H 2007;25:286.

[30] Fan P, Fang ZZ, Sohn HY. Acta Mater 2007;55:3111.

[31] Eso OO, Fan P, Fang ZZ. Int J Refract Met H 2008;26:91.

[32] Fan P, Eso OO, Fang ZZ, Sohn HY. Int J Refract Met H 2008;26:98.

[33] Fan P, Fang ZZ. Int J Refract Met H 2009;27:37.

[34] Fan P, Guo J, Fang ZZ, Prichard P. Int J Refract Met H 2009;27:256.

[35] Fan P, Guo J, Fang ZZ, Prichard P. Metall Mater Trans A 2009;40:1995.

CHAPTER 2

LITERATURE REVIEW

Functionally graded material (FGM) belongs to a class of advanced materials featured by gradual transitions in composition, phase distribution, porosity, texture, and grain size within a component, resulting in gradual changes in the physical, chemical and mechanical properties [1-5]. The concept of FGM is not new and is commonly observed in many biological organs and tissues such as animal bone, squad beak, fish scale, plant stem, bamboo and many others [6-9]. These graded structures are created by nature over millions of years of evolution. In modern engineering, the most famous example of FGM is the surface hardened/carburized steel characteristic of relatively high carbon content at the surface than that in the bulk [10]. Owning to improved performances achieved by FGM, a wide range of processes have been developed to produce FGM involving powder metallurgy, pulsed laser deposition, centrifugal casting, infiltration, combustion synthesis, slip casting, etc. [1-5, 11-23]. The research of FGM has received great attention and is spreading into the fields of mechanical, optical, electrical, thermal, nuclear and medical applications [24-27].

Functionally graded cemented tungsten carbide (FG WC-Co) is a typical example of FGM. In FG WC-Co, it has a graded distribution of WC grain size and/or Co content giving rise to varying wear resistance and fracture toughness throughout the microstructure. Compared with the conventional WC-Co material with a homogeneous

distribution of composition and microstructure, the performance of FG WC-Co is optimized and their service life is extended by the superior combinations of fracture toughness and wear resistance [28-30].

In the past decades, although there are many methods emerged to produce FG WC-Co [31-48]. An economic processing method for making FG WC-Co is liquid phase sintering. However, the manufacture of FG WC-Co with graded Co composition via liquid phase sintering process is difficult because the liquid Co phase tends to migrate and the gradient is homogenized within the material [33, 37, 40]. To meet this challenge, extensive fundamental research on the liquid phase migration (LPM) has been carried out for the purse of solving the gradient homogenization problem [49-55]. Although the principles of LPM have been well understood, there is to date no process that could be used to manufacture FG WC-Co in industrial scale except in special cases such as processes for making so-called dual properties (DP) carbide [56-59] and WC-Co with cobalt enriched surfaces [60-62], both of which form only under special conditions and generate only limited microstructure gradients. Other processes for making FG WC-Co that are available in literature rely on solid state sintering process or premixing powder with different compositions, all of which have severe limitations with regard to their versatility and practicality [33, 37, 44, 48]. It is imperative to develop a cost-effective process for manufacturing a wide range of FG WC-Co with desirable gradient and improved properties, which is the focus of this dissertation.

In the following sections, first of all, it introduces that important aspects of WC-Co system related to the development of FG WC-Co including sintering, phase equilibria, composition and microstructure. Second, two examples of FG WC-Co and their practical

applications are described. Third, current status of the various methods for fabricating FG WC-Co and their limitations are addressed in detail. Fourthly, the fundamental theories on LPM during liquid phase sintering are presented. Finally, two models relevant to the process of manufacturing FGM are reviewed.

2.1 Cemented Tungsten carbide

As one of the oldest and most successful powder metallurgy products, cemented tungsten carbide (WC-Co) or hardmetal is a two-phase composite material in which relatively hard, brittle WC grains are bonded together or cemented by tough, ductile Co binder [63]. In Figure 2.1, the phase with dark contrast is the Co binder and the phase with light contrast is the WC grains. The manufacturing of WC-Co is based on a powder metallurgy route through the following consecutive steps: powder synthesizing, compact forming, and sintering. Sintering is a process whereby powder compacts are heated and consolidated into a coherent bonded solid body. In this section, the sintering of WC-Co composites is described. Furthermore, the phase relationship and the microstructural aspects of WC-Co are discussed.

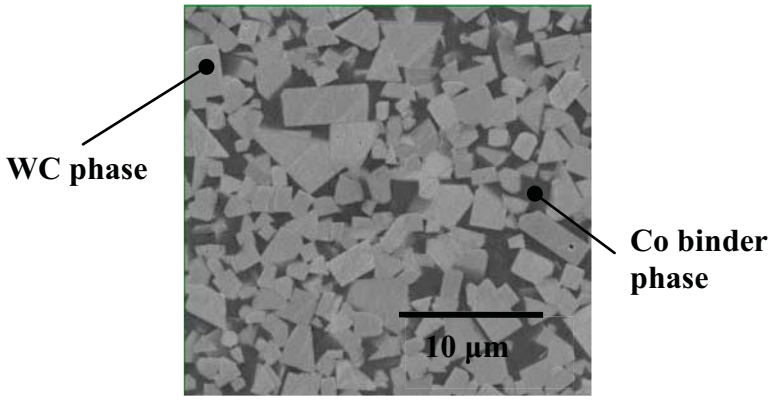

Figure 2.1 Typical microstructure of WC-Co composites.

2.1.1 Sintering of WC-Co

WC-Co is typically sintered by employing the most economically viable liquid phase sintering process which accomplishes full densification without the need of any external pressure. In the WC-Co system, the lower melting phase is Co phase and the higher melting phase is WC phase. The liquid phase sintering of cemented WC-Co is performed at temperatures above the solidus of Co phase. Hence the consolidation of WC-Co is completed in the presence of liquid [64]. Reduction of surface energy is the primary driving force for densification. A successful liquid phase sintering should meet the minimum criteria involving: (i) a low temperature; (ii) solubility of the solid in liquid and (iii) liquid wetting of the solid grains. These conditions will lead to a reduction in surface energy with liquid spreading. For the W-C-Co system, the liquid Co phase produced during sintering satisfies all the basic conditions required for liquid phase sintering owing to the good wettability and solubility of WC in the Co phase [63]. The densification process during liquid phase sintering of WC-Co proceeds in three stages: (i) an initial liquid flow stage in which rearrangement of the particles occurs; (ii) a subsequent solution-reprecipitation stage that gives closer packing; and (iii) a final coalescence stage in which densification slows to the rate pertinent to the solid phase sintering.

An alternative way to sinter WC-Co is by means of solid phase sintering. During the solid phase sintering, WC-Co is consolidated below the solidus temperature of Co phase without involving any liquid phase [63, 64]. Compared to the liquid phase sintering, the solid phase sintering requires much longer sintering time and is very difficult to accomplish full densification. The remaining porosity that plays an important part in initiating fracture is detrimental to the mechanical properties of materials. Therefore, in

order to eliminate the remaining porosity, it often uses pressure-assisted solid phase sintering techniques, such as hot isostatic pressing or spark plasma sintering. However these pressure-assisted solid phase sintering processes are limited in industrial applications because of two reasons. The first is that pressure-assisted solid phase sintering needs high pressure, which is expensive, and the second is that the mechanical properties of WC-Co achieved in solid phase sintering process are not as desired as those produced by liquid phase sintering.

2.1.2 Phase Equilibria in W-C-Co System

The phase relation of W-Co-C system is crucial for the production of WC-Co. There have been considerable efforts devoted to develop the W-C-Co ternary phase diagram to study the phase relations in this system. The approach initially is completely via experiments using X-ray diffraction, metallographic techniques and differential thermal analysis. Later on the phase diagrams are established based on combining experimental and thermodynamic calculations.

The phase diagram serves a very useful tool for the process control of the manufacture of WC-Co materials. It can be used to determine what phases in existence and in what quantities. As an example, Figure 2.2 shows a vertical section of the ternary phase diagram of W-C-Co system with a constant Co content at 6.0 weight percent (wt%) constructed by Guillermet [65]. It indicates what phases exist as a function of temperature. From Figure 2.2, given a WC-Co material carbon content of 5.75 wt%, there is a three phase region in which WC, liquid Co, and solid Co coexist in temperature range between 1300 and 1320^{o}C; at the temperature above 1320^{o}C, only liquid Co and WC phase exist; while at temperature below 1300^{o}C, only solid Co and WC phase exist. Additionally, this

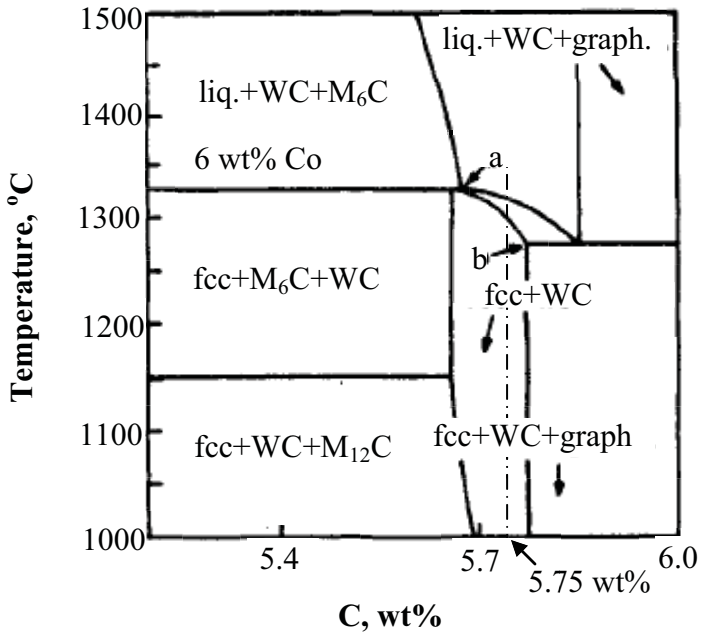

Figure 2.2 Vertical sections of the W-C-Co phase diagram, adapted from [65].

vertical section of phase diagram can be used for selecting the carbon content of the system such that the formations of the undesirable phases including the graphite and the η-phase can be avoided [66]. As clearly shown in Figure 2.2, if the alloy with a carbon content falls between the points indicated by “a” and “b”, it will consist of only WC and Co phase without any third phase. However, noting that the range of favorable carbon contents will be narrowed if considering the fact that the precipitation of graphite or the η-phase usually takes place at lower temperatures. Figure 2.3 is another example of phase diagram of W-C-Co system [67], which is an isothermal section of the ternary phase diagram of W-Co-C system with 10 wt% of Co at 1400^{o}C

Though there are differences among the various phase diagrams, phase diagrams share some similarities: (1) for compositions corresponding to a W/C atomic ratio close to one, the phase WC, solid, and liquid Co are stable; (2) at lower carbon contents, brittle

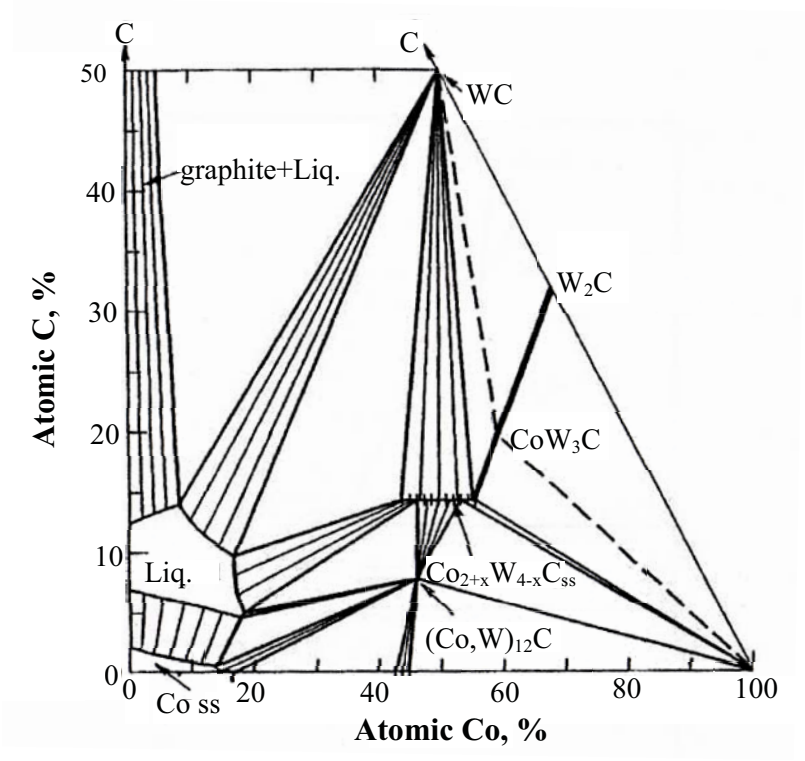

Figure 2.3 Isothermo section of W-C-Co phase diagram, adapted from [67].

η-phase, which is essentially W_3Co_3C or Co_6W_6C, occurs. Other ternary phase of W_2C will be stable only at a much lower carbon content or at a very low cobalt content respectively; (3) at W/C below 1, primary carbon will precipitate and remain in equilibrium with WC and Co phase in solidified alloys. (4) the two phase WC-Co exists only in a narrow range of carbon concentration [63].

2.1.3 Microstructural and Compositional Aspects of WC-Co

Microstructural and compositional studies of WC-Co alloys are of great importance for understanding their properties and engineering performances. The mechanical properties of WC-Co composites have a strong dependence on the following microstructure and composition parameters include (i) Co binder phase volume fraction

and its composition; (ii) Phase size and size distribution and (iii) Contiguity, angularity, and misorientation of WC phase. Characterizations of these microstructural and compositional variables are mostly based on image analysis using different techniques including optical microscopy (OM), scanning electron microscopy (SEM), orientation imaging microscopy (OIM), transmission electron microscopy (TEM), X-ray diffraction (XRD), energy dispersive spectroscopy (EDS), etc.

2.1.3.1 Volume Fraction and Composition of Co Binder Phase

The volume fraction of Co phase is a very important factor influencing the mechanical properties of WC-Co materials. In industrial practice, the WC-Co hard materials is also characterized in terms of weight percent (wt%). However, the volume fraction is more informative than weight percent because the density of Co binder phase (8.8-9.5 g/cm^3) varies with the composition of tungsten, carbon or other alloying elements dissolved in the Co phase. Figure 2.4 shows the general trend of various mechanical properties variation with Co content. Generally, for a given WC grain size, an increase in the volume fraction of Co binder phase gives rise to increased toughness but decreased hardness.

The control of the composition of Co binder phase, particularly carbon composition, is equally important. It was reported that an increase in the carbon content of the WC-Co material during sintering can cause an abnormal grain growth [68]. However, too high as well as too low carbon content can bring about the precipitation of a third phase (either graphite phase or η phase) besides the tungsten carbide and cobalt phases [66]. The occurrence of either the graphite phase or η phase will decrease the strength of WC-Co materials and should be avoided.

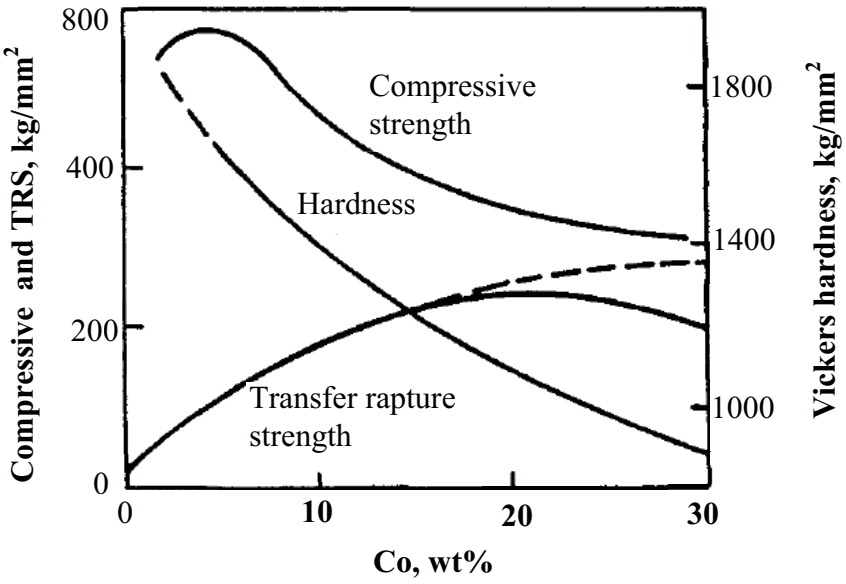

Figure 2.4 Effect of cobalt content on vickers hardness, compressive and transverse rupture strength of WC-Co hardmetal with grain size of about 2 μm, adapted from [63].

To determine the carbon compositions, standard analytical methods are available, such as inductively coupled plasma emission (ICP) spectroscopy and infrared (IR) absorption carbon determination. Alternatively, the carbon content can be determined by measuring magnetic saturation (represented by σ_S) for a nondestructive evaluation [69]. For a given Co content, the magnitude of the saturation magnetization is sensitive to the carbon content of WC-Co alloys and σ_S rises as carbon content increases. Specifically, the carbon content can be measured according to the following equation:

$$w/oC = 6.13 - [0.053 f_{Co}(160 - \frac{\sigma_S}{f_{Co}})] \tag{2.1}$$

where *w/oC* is the carbon content of the WC phase of the alloy, f_{Co} is the weight percent of Co content.

2.1.3.2 Contiguity, Angularity and Misorientation of WC Phase

The contiguity is a measure of the degree of contacts between WC grains and is defined as the ratio of the WC/WC grain boundary surface area to the entire interface area of WC/WC interfaces plus WC/Co interfaces. The study of the contiguity is crucial as it affects the mechanical properties. The hardness generally increases and fracture toughness decreases with the increasing contiguity. The contiguity can be calculated using a linear intercept analysis, which is derived from the equation [70]:

$$C = \frac{2N_{CC}}{2N_{CC} + N_{BC}} \tag{2.2}$$

where N_{CC} and N_{BC} are the average number of intercepts per unit length of test lines with the traces of WC/WC grain boundaries and WC/Co interfaces. It was found that contiguity decreases with the increase of Co content and the WC grain size.

The angularity and the misorientation relationship among WC grains are two important features of WC phase in WC-Co materials. The angularity of WC phase refers to the degree of surface faceting of the grains. It is well known that the presence or the absence of special crystallographic relations between neighboring grains alters the properties of materials to a large extent.

2.1.3.3 Phase Size and Size Distribution

The mechanical properties of WC-Co materials also depend on the size of individual phase and its size distribution. For example, a trend of transverse rupture strength variation with grain size of WC phase is presented in Figure 2.5. In general, finer WC grain size leads to higher hardness and strength but the trade-off is the lower toughness.

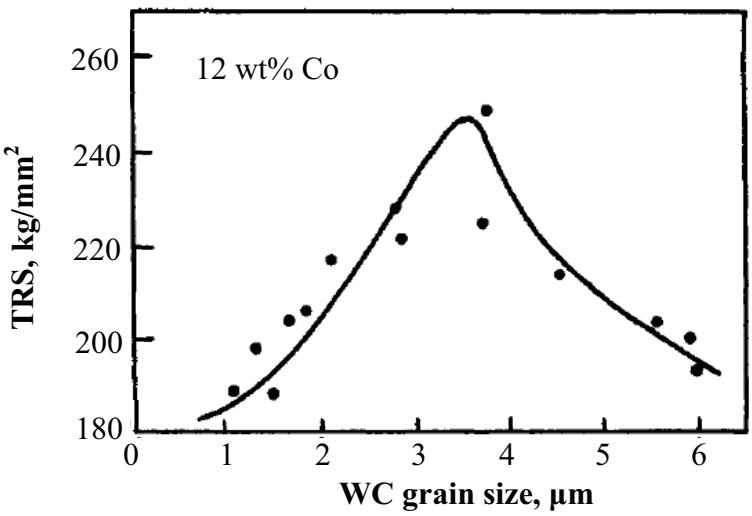

Figure 2.5 Effect of WC grain size on transverse rupture strength of WC-Co hardmetal with Co of 12 wt%, adapted from [63].

Traditionally, WC grain sizes are determined from optical micrographs or electron micrographs of polished cross-sections of specimens [71]. In this class of image analysis methods, the mean linear intercept length method is commonly used in WC-Co specimens. In this method, the WC grain size (d) is measured by laying a series of uniformly distributed test lines on the planar section and counting the number of times that grain boundaries are intercepted, which is calculated from:

$$d = \frac{L}{N} \tag{2.3}$$

where L is the total length of line across WC grains and N is the number of the WC grains traversed. Beyond that, this image analysis can be used to analyze the grain size distribution. Usually, the linear intercepts in the carbide grains show a distribution very close to a logarithmic Gaussian distribution [72].

Another method for characterizing WC grain size is performed by the magnetic coercivity (H_c) measurement. The magnetic measurements are possible due to the ferromagnetic Co phase despite the nonmagnetic WC phase. In fact, the average WC grain size is approximated from its linear dependence on the magnetic field required to restore zero magnetization. Qualitatively, the coercivity rises with a decrease in WC grain size if the cobalt content and carbon content are maintained the same. Quantitatively, the WC grain size (L_{WC}) can be calculated from the empirical equation established by Fang et al. [69]:

$$L_{WC} = 73\left[1 - 1.03\exp(-5V_{Co})\right]\left[\frac{1 - V_{Co}}{H_C V_{Co}}\right] \tag{2.4}$$

where V_{Co} is the volume fraction of Co phase and H_c is the magnetic coercivity. This simple and convenient technique provides a nondestructive grain size evaluation.

The size of binder Co phase is a measure of the thickness of the Co layer, which is also referred to the mean free path of Co phase. It is defined by the arithmetic means of the distance from one WC/Co interface to the other as measured in Co phase. The mean Co free path (d_{Co}) depends on both the Co content and the WC grain size, which is usually determined from the following formula [73]:

$$d_{Co} = \frac{1}{1 + C} d_{WC} \frac{V_{Co}}{V_{WC}} \tag{2.5}$$

where d_{WC} is the mean WC grain size, C is the contiguity of WC phase, and V_{Co} and V_{WC} are the volume fractions of Co phase and WC phase, respectively.

2.1.4 Grain Growth Inhibitor Doped Ultrafine Grain WC-Co

As mentioned in Section 2.1.3.3, WC-Co materials with fine grain microstructure exhibit marked increase in wear resistance, and transverse rupture strength [63]. It thus becomes a trend to use finer and finer grades of WC-Co for the manufacture of machines tools and wear parts. For such applications, the tool made of ultrafine WC-Co has the ability to maintain very sharp cutting edge during use because of their higher hardness and improved fracture toughness.

To obtain the fine grain WC-Co materials, the major technical obstacle is to be able to limit the WC grain growth during sintering. It is typical to add grain growth inhibitors to address the problem of grain growth. The most commonly used grain growth inhibitors are vanadium carbide VC and chromium carbide Cr_3C_2 with TaC and NbC used less frequently. Lately, a number of studies were contributed to understand the mechanism for the grain growth inhibition but the exact mechanism is still unknown [74-80]. It is known that the additions of various grain growth inhibitors can reduce the melting point of Co enriched binder phase in WC-Co [78]. Therefore, the inhibitor added WC-Co materials are able to consolidate at lower temperature. Sadangi et al. [74] speculated that the lower consolidation temperature may contribute to limiting the grain coarsening.

Moreover, it is found that the effects of grain growth inhibition enhances with the increasing amount of addition. However, the inhibition effect does not increase when the addition exceeds its solubility in the binder phase. Except for that, the excessive addition of inhibitor will be detrimental to the mechanical properties of WC-Co itself due to the precipitation of brittle phase at the WC/Co interface. It is thus preferable that the inhibitor level can be lowered while still maintaining the grain refining effects.

2.2 Functionally Graded WC-Co

Different from the homogeneous WC-Co materials, functionally graded WC-Co materials (FG WC-Co) are featured by a nonuniform distribution of the Co content and/or WC grain size from the surface to the bulk of the part or from one reference position to another reference position within the microstructure. Because the wear resistance and the fracture toughness of WC-Co materials strongly depend on their Co content and WC grain size, a property gradient can be achieved by introducing a compositional and/or microstructural gradient in the microstructure. This property gradient offers a superior combination of wear resistance and fracture toughness and therefore the engineering performance of materials are greatly optimized. In current practical applications, there are two famous graded WC-Co products, both of which are described as follows.

2.2.1 Dual Phase (DP) carbide

The first example is the Dual phase (DP) carbides that were described as “the most significant innovation in the history of cemented carbides since the early 1950s [56-58]. DP carbides are primarily applied in the tools for drilling of rock and mineral. The body of DP carbides is characterized by a three-layered structure with different Co contents in each layer. To illustrate, the Co distributions in the three distinct layers are shown by a schematic plot of Figure 2.6. It is clear that, within the outermost surface layer with a thickness of around 1-3 mm, the surface Co content is lower than the nominal Co content in the bulk and the Co content is increasing continuously with the distance from the outmost surface into the interior. In the middle layer, the Co content is increased to a maximum Co value which is higher than the nominal value in the bulk. In the bulk, Co is

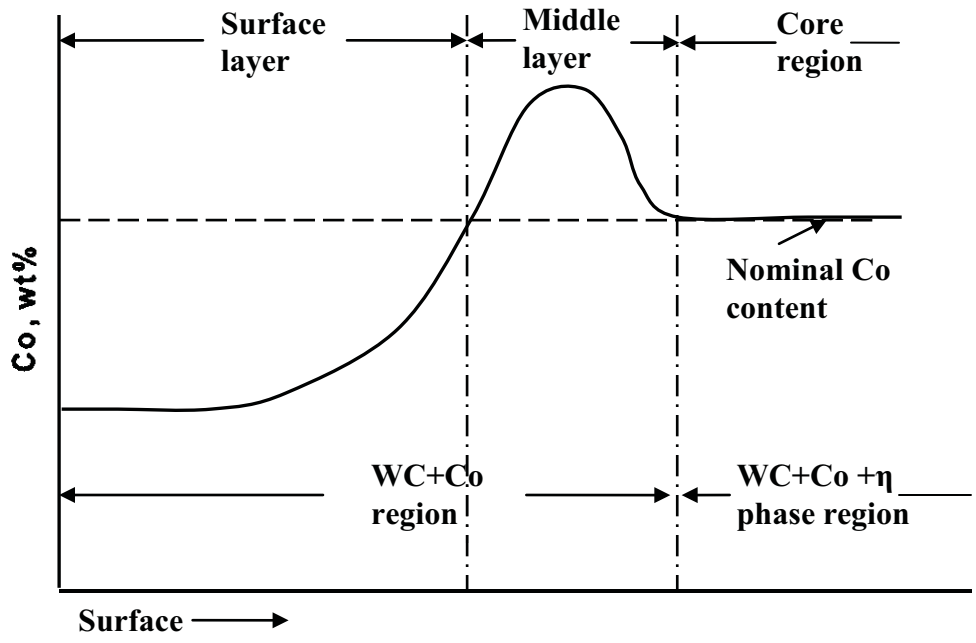

Figure 2.6 Schematic diagram of the cobalt distribution in DP carbides.

uniformly distributed at the nominal value. With this type of Co compositional gradient, desirable mechanical properties and performances are acquired. For instance, when the DP carbides are utilized in rock drilling, the surface layer with relatively low cobalt content provides high wear resistance and high hardness for penetration in rocks or mineral. The middle layer between the low cobalt surface and the core of the part establishes an enrichment of cobalt content, which gives rise to high toughness that can effectively prevent cracks from propagation. Owing to the superior combinations of wear resistance and toughness, the drilling tools made of DP carbides display an improved efficiency and prolonged life. It was reported that the tools made of DP carbides have an increase of 40 % in service life when compared to the tools made of conventional WC-Co materials.

2.2.2 WC-Co with Cobalt Enriched Surface

Another example of FG WC-Co is WC-Co with a Co-enriched surface layer, which has been commercialized in fields of metal cutting tools since 1980s [60-62]. This graded structure is often used in substrates for coating a thin layer of high abrasive wear resistance material, such as TiC, TiN and Al_2O_3. Prior to the introduction of this type of FG WC-Co, the high wear resistant materials are directly coated on the homogeneous WC-Co substrates. The coating is usually performed by a chemical vapor deposition (CVD) process. Due to differences in thermal expansion, cracks are unavoidably formed in the coatings during cooling after the CVD process. When the coated tools are used for machining, these cracks might propagate into the substrate and cause failure. The enrichment of Co at the surface of the FG WC-Co substrates provides a tough layer that prevents cracks emanating the hard but brittle coating from propagating into the material thereby the life the tool made of FG WC-Co is elongated. Figure 2.7 shows the cobalt distribution present in the WC-Co substrate of the cutting insert.

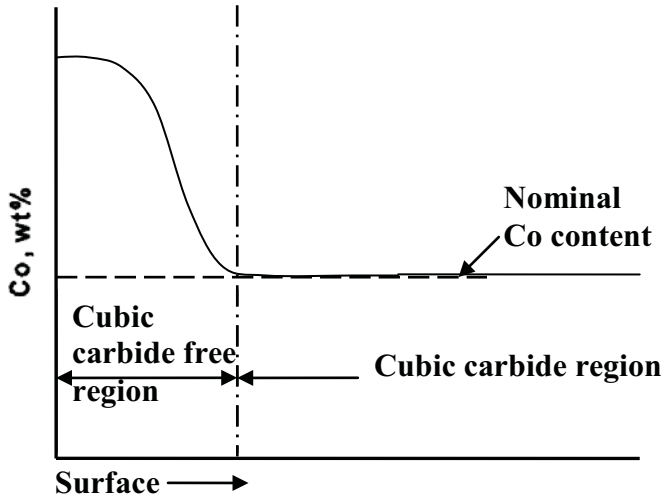

Figure 2.7 Schematic diagram of the cobalt distribution in a cutting insert with cobalt enrichment at the surface region.

2.3 Processes for Manufacturing Functionally Graded WC-Co

The manufacturing processes for making FG WC-Co can usually be distinguished into two classes. The first class is termed as “Powder Consolidation Process” by building compositional and/or microstructural gradients in powder compacts then densifies the compacts into bulk materials. The second class is termed as “Atmosphere Heat Treatment Process” which relies on heat treatment in specific atmospheres to induce mass transport and form the gradients at the near-surface region. The following section discusses these two classes of processes.

2.3.1 Powder Consolidation Process

The powder consolidation process is usually based on two steps that are gradation and consolidation. During the gradation step, the gradient is built in the powder compacts by the use of mixture powders with varying grain size or compositions. A smooth or stepwise changed gradient will be obtained depending on the method applied for producing the graded powder compacts. In the subsequent consolidation step, the green compacts are sintered to dense bulk materials.

2.3.1.1 Die Compaction

A straightforward means for creating graded compact is through pressing layers of powders with difference in compositions and/or WC grain sizes in the compacting die [33, 40, 41, 46] as illustrated in Figure 2.8. Afterwards, the graded powder compact is sintered to full densification. This simple method is effective in creating gradients in powder compacts. However, the disadvantages in the creation of graded powder compacts are also obvious, like it is only convenient for processing FG WC-Co with

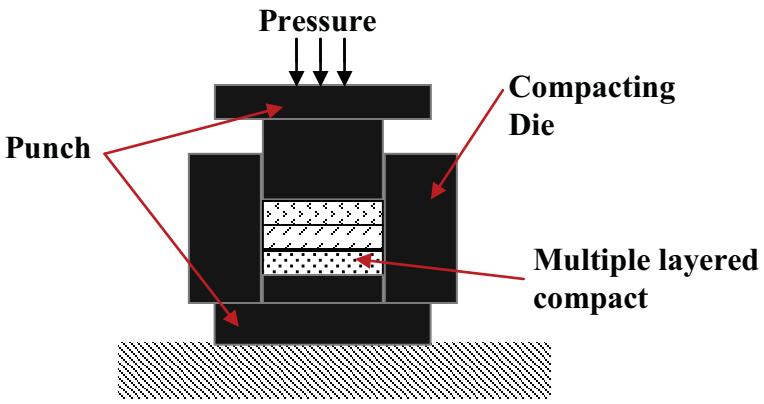

Figure 2.8 Schematic diagram of the uniaxial die for compacting layered functionally graded WC-Co parts.

simple geometry, e.g., unidirectional gradient in flat-shaped compacts. The disadvantages also include: discontinuous gradients, the minimum layer thickness of individual layers is often larger than a few hundreds of micrometers as well as discontinuous manufacturing with low productivity.

Besides, the consolidation of the powder compact faces many challenges. Although the liquid phase sintering is an economical option for consolidating WC-Co, it is not easy using it to consolidate FG WC-Co. The first challenge is that the powder compact is prone to significant distortion during sintering. The distortion problem is caused by the uneven shrinkage of compacts as their sintering behaviors differ with the particle size and the composition of the powders. Studies by Rassbach et al. [46] have shown that distortions of the parts can be alleviated by adjusting the powders in the different layers. The second and the most difficult challenge is that it is difficult to preserve the gradient that has been built in the powder compacts. This is because when the powder compact is heated to the temperature of liquid phase sintering, the Co binder phase is melted in

liquid state and the liquid Co phase tends to flow or migrate, resulting in a rapid homogenization of gradient that has been built in the green compacts. The homogenization of liquid Co phase during liquid phase sintering is attributed to a physical phenomenon proposed as liquid phase migration. Extensive studies have been dedicated to investigating the phenomenon of liquid phase migration, the details of which are introduced in Section 2.4. It has been demonstrated that FG WC-Co materials can be manufactured by controlling liquid phase migration during liquid phase sintering [46, 53, 55, 81-87].

In order to retain the compositional gradient in powder compact, an alternative sintering approach is by employing pressure assisted solid phase sintering, such as hot isostatic pressing (HIPing) or solid phase sintering plus HIPing or high-pressure-assisted rapid sintering processes like spark plasma sintering (SPS) [33, 40, 41]. These sintering methods not only overcome the gradient homogenization problem but also meet the densification requirements. However, these high pressure assisted processes are very costly and will cause negative effect to the mechanical properties of materials due to the extreme conditions of high temperature and high pressure. Overall, this die compacting method is easy and effective and convenient. The biggest difficulty lies in the consolidation of powder compacts without homogenizing the gradients.

2.3.1.2 Powder Injection Molding

The powder injection molding (PIM) is an industrial manufacturing process for forming objects by injecting powders into a mold. Compared to the simple die compaction method, this technique allows the production of more uniform and more complex green parts. Li et al. [45] utilized PIM to mold a double layered graded WC-Co

component. During the molding process, the melted feedstock of powders of low Co content is injected into cavity A to form a small core. After that this small molded core is moved to a bigger cavity B and another melted feedstock of powders with high Co content is injected into cavity B to cover this molded core. A double layered compact is produced in this process. Subsequently the molded part is sintered to produce an integrated component with lower-Co-higher-hardness in its outer layer and higher-Co-higher-toughness in the core. For PIM, it has the same difficulties during the consolidation step as the die compaction method has.

2.3.1.3 Electrophoretic Deposition

The electrophoretic deposition (EPD) is an efficient and low cost process capable for fabricating objects with complicated shapes. It has a fairly wide application in many industries like coatings, laminated materials and functionally graded materials, etc. This process provides a way for producing continuously changed gradients by continuously depositing different powder mixtures in the green body. In an EPD process developed by Put et al. [37], it is composed of two subprocesses which are the movement of charged particles in suspension in the electric field between two electrodes and the subsequent deposition of the particle on either of the electrodes. A smooth gradient with varying composition and/or thickness can be achieved by changing the process parameters such as the supplying rate of different powders as well as other elctrodeposition conditions. Then the deposits were removed from the electrode, slowly dried and sintered to bulk functionally graded WC-Co. Similar to the other powder consolidation processes, the sintering remains a major challenge for EPD.

2.3.1.4 Local Addition of Grain Growth Inhibitor

As is well known, for given Co content, the hardness increases with decreasing WC grain size. However it is difficult to vary grain sizes continuously though powder deposition methods. Greenfiled [36, 42] invented a process that is able to produce the continuous gradient by varying grain size. This approach is based on selectively introducing WC grain growth inhibitors (mainly Cr and V) into the near-surface-layer of WC-Co composites. As a result of this technology, the near-surface region contains higher concentration of Cr or V than the core region, which causes the grain size at the surface is much finer than that in the core. Finally, FG WC-Co with high wear resistant surface and tough core is obtained. However, with a longer sintering time, the high surface hardness tends to be offset by the increasing Co content due to the migration of the liquid phase from the core region with coarser grain size to the surface zone with finer grain size. Hence the sintering condition needs to be optimized to minimize the liquid phase migration.

Beyond that, there might be difficulties associated with applying the grain growth inhibitors or their precursors to the surface of the WC-Co green compacts with complicated geometries. Also, the application of Cr or V may lead to decreased mechanical properties due to the precipitation of brittle carbides at the WC/Co interfaces which have been mentioned earlier in Section 2.1.4.

2.3.2 Atmosphere Heat Treatment Process

The atmosphere heat treatment process is often used to improve the metallurgical and mechanical properties. It has a long history of industrial applications and one of its most famous application is the carburizing heat treatment for steel surface hardening [10].

During the carburizing heat treatment of steels, work pieces are heat treated in carburizing atmospheres to produce products having hard surfaces and tough cores, which is a typical example of functionally graded material. The atmosphere heat treatment process is viewed as an economical and promising manufacturing technique because it is a low cost and effective process with high flexibility in the geometries of the treated parts.

Considering the advantages of the atmosphere heat treatment process, it is appealing to apply it in the fabrication of FG WC-Co materials. In WC-Co system, it is well known that carbon and nitrogen can induce the redistribution of liquid Co, which can be exploited to acquire the Co gradient by atmosphere heat treating. The DP carbides and WC-Co with Co-enriched surface that have been introduced earlier exemplify that the graded Co composition can be developed via undertaking atmosphere heat treatments.

2.3.2.1 Carburizing Atmosphere Heat Treatment

The carburizing atmosphere heat treatment process can be used for producing DP carbides with Co compositional gradients [56-59, 88-93]. According to the process invented by Fisher et al. [56-58], DP carbides were prepared by heat treating presintered η-phase-containing WC-Co specimens in a carburizing atmosphere at a typical liquid phase sintering temperature. During the carburizing process, the reaction between carbon and η-phase produces an η-phase-free surface layer. The surface layer is characterized by a very low surface cobalt content rising gradually with the depth into the material. Beyond the surface layer, the core still contains η-phase in the as-sintered material. Because brittle η-phase is detrimental to mechanical properties of WC-Co, it is desirable for many applications that FG WC-Co materials to be made without η-phase. To

completely remove η-phase using the DP carbide process as described above; however, it requires a long heat treatment time at the liquid phase sintering temperature, which may eliminate Co gradient, and may also be economically unfeasible [57].

2.3.2.2 Denitriding Atmosphere Heat Treatment

Another example of atmosphere heat treatment process is employing the denitriding process for manufacturing FG WC-Co with its surface enriched in Co phase [60-62, 94-106]. Prior to the treatment process, the first step is to obtain a WC-Co parts containing nitrogen either by direct addition of nitrogen containing compounds (TiN, Ti(C,N)) or by flowing nitrogen gas during heating. Then these nitrogen containing materials are exposed in vacuum or denitriding atmospheric condition, in which the outward diffusion of nitrogen and the inward diffusion of titanium result in the surface zone enriched in Co phase. Currently, this process is widely used in the substrates for coated machining tools. Yet, this process still has limitations for wider applications as the gradient only forms under special conditions requiring the addition of nitrides.

2.4 Liquid Phase Migration during Liquid Phase Sintering

In both classes of the processes, “Powder Consolidation Process” and “Atmosphere Heat Treatment Process”, a common feature of the two classes of processes is the occurrence of liquid phase migration (LPM) during sintering or post-sintering heat treatment as introduced in Section 2.3. During the “Powder Consolidation Process”, the phenomenon of LPM plays a role in the elimination of the gradient. However, in the “Atmosphere Heat Treatment Process”, the liquid phase migration plays an opposite role in inducing the gradients. It is therefore necessary to conduct a comprehensive study on

the LPM process and then we are able to take advantage of LPM for making functionally graded materials. A brief review of the phenomenon of LPM will be given in following section.

2.4.1 Introduction

The phenomenon of LPM was first revealed by Lisovsky [107] who studied the process of spontaneous imbibitions of binder melts into pore-free composite materials over 20 years ago. He found that when a porosity-free WC-Co (initial Co content 5.9 wt%) composite composed of WC skeleton filled with a Co enriched phase at 1390 ^{o}C was put into contact with a Co melt pool at the same temperature, the composite body imbibed a large amount of the Co melt as shown in Figure 2.9. First, it should be noted that the composition of the Co binder phase is in chemical equilibrium with the Co melt and therefore this liquid flow cannot be explained on the basis of diffusion of components. Second, this type of spontaneous liquid imbibition is similar but essentially different from a conventional capillary driven flow. Regarding the flow driven by the capillary force, the liquid is spontaneously imbibed into a porous medium when a porous medium is putting in contact with a liquid pool. This capillary driven flow is attributed to the capillary force at the solid-liquid-gas interface [108]. Therefore, the theories of capillary force cannot be used to explain the liquid flow in a pore-free medium without the presence of gas phase. The term “liquid phase migration” (short for LPM) is thus defined to specifically refer to the flow of the liquid phase in the solid-liquid-two-phase system in the absence of any pore space, so as to distinguish it from that in the solid-liquid-gas-three-phase system.

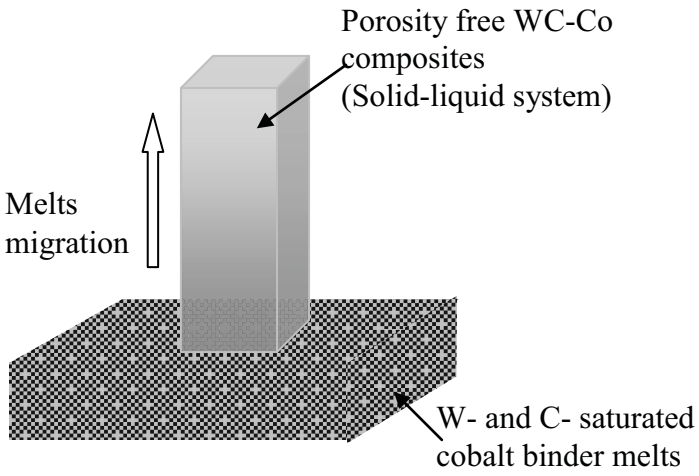

Figure 2.9 Schematic diagram of the process of spontaneous imbibitions of binder melts into pore-free WC-Co composite materials at 1390^{o}C under vacuum.

A fundamental understanding of LPM is important for manufacturing of various functionally graded materials, including FG WC-Co, via the liquid phase sintering process. Currently, considerable efforts have been devoted to explore the thermodynamics and kinetics principles governing the liquid phase migration process [49-55, 81-87, 109-117], which are described as follows.

2.4.2 Thermodynamics of Liquid Phase Migration

2.4.2.1 Driving Force

Lisovsky [114] studied the driving force of LPM by modeling the changes in the interfacial energy during the imbibition of the metal (Co) melt, which can be described by the equation below:

$$\Delta F = \frac{K}{3}\gamma_{sl}\left(1-\frac{\gamma_{ss}}{2\gamma_{sl}}\right)\frac{1}{d}\left(\frac{1-u}{u}\right)^{\frac{1}{3}}\Delta V_l \qquad (2.6)$$

where γ is the surface tension. d is the particle size. u is the volume fraction of liquid phase. K is a coefficient. ΔV_l is the volume of the liquid imbibed. The subscripts "*ss*" and "*ls*" represent the solid/solid and solid/liquid interfaces, respectively.

It follows from the equation (2.6) that the migration process happens spontaneously when $\Delta F < 0$ and $\gamma_{xx}/(2\gamma_{sl}) > 1$. It serves a criterion to define a class of composite materials, such as WC-Co, WC-Ni, Co-Cu, W-Fe, and Fe-Cu etc., having the ability to imbibe their own melts. Therefore, Lisovsky's model theoretically demonstrated that the driving force for the liquid phase migration in the solid-liquid system is the reduction of the total interfacial energy of the system.

The driving force of liquid phase migration can also be described by the term "liquid migration pressures", designated by P_m [49]. If P_m is not homogeneous within a system, liquid phase will flow from a location with relatively low P_m to a location with relatively high P_m. It is worth noting that the liquid migration pressure acts as an imbibition pressure or negative pressure, according to its physical effect. The liquid migration does not stop until P_m reaches homogeneity everywhere in the system. In other words, the liquid distribution reaches equilibrium when the liquid migration becomes homogeneous in the system. Therefore, the liquid migration pressure will influence the equilibrium distribution of liquid phase and in turn determine the final compositional gradient.

2.4.2.2 Dependence of Liquid Phase Migration Pressure

Conceptually, it has been clarified that the liquid migration process is driven by the reduction of total interfacial energy of the system. The driving force of liquid phase migration can be measured by liquid phase migration pressure, P_m. From a practical point

of view, in order to control liquid phase migration, it is necessary to identify the key factors that affect P_m and establish a quantitative relationship of P_m as a function of these factors.

As liquid phase migration is an interfacial-energy-driven phenomenon, any factor that affects the total interfacial energy in a system will affect both the liquid migration pressure and the equilibrium liquid distribution. Based on the analysis on the interfacial energy in a simplified model system by Delannay et al. [51] P_m is dependent of the following five factors: (1) the volume fraction of the liquid phase, u, (2) the grain size of solid phase, d, (3) the interfacial energy between the solid and the liquid phase, γ_{sl}, (4) the interfacial energy between grains of the solid phase, γ_{ss}, and (5) the coordination number of the solid grains, n_c. In many practical sintering systems, the coordination number n_c is found to depend on the other three factors (u, γ_{sl}, and γ_{ss}). For a system with a given solid phase, the solid/solid interfacial energy γ_{ss} is fixed, while the solid/liquid interfacial energy γ_{sl} varies depending on the composition of the liquid phase. In summary, there will be only three key factors determining P_m: the volume fraction of the liquid (u), the solid grain size (d), and the composition of the liquid phase [55].

Take the W-C-Co system as an example, it has been experimentally demonstrated that P_m is dependent on these three key factors mentioned above. Fang et al. [53, 55, 81-87] documented that liquid phase migrates from the regions with higher volume fraction of liquid Co phase to the regions with lower fraction of liquid Co phase, from the regions with coarser grain size to the regions with finer grain size, and from the regions with higher carbon content to the regions with lower carbon content, as illustrated in Figure 2.10.

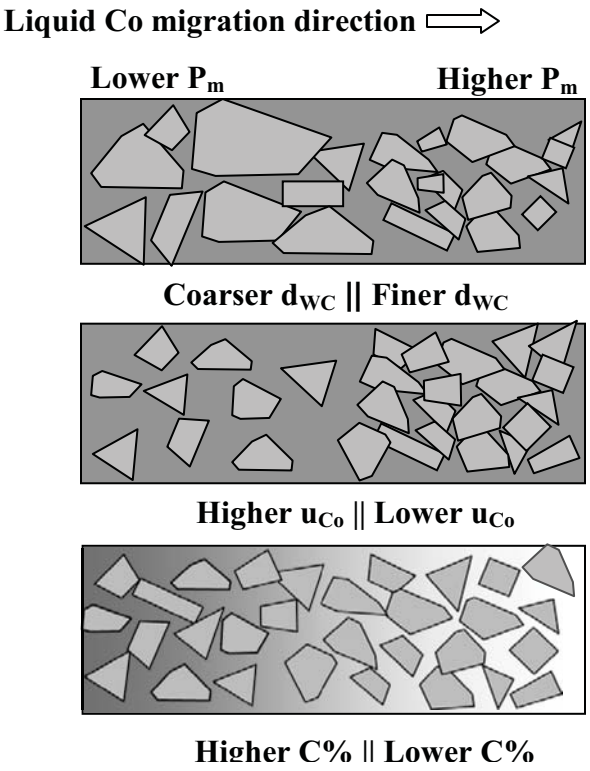

Figure 2.10 Schematic diagram of the direction of liquid Co migration in sintered bi-layered sample dependent on the gradients of grain size (d_{WC}), liquid volume fraction (u_{Co}) and carbon content ($C\%$).

Based on an experimental study by Lisovsky [49, 107, 118], the migration pressure P_m was determined by measuring the radius of liquid Co surface filled in V-shaped capillary and expressed as:

$$P_m = dF / du = k_0[(1/u - 1)^{1/3} - 1.41u]/d \tag{2.7}$$

where k_0 is a coefficient.

According to equation (2.7), P_m is predicted to diminish when u=0.61, which matches with the experimental data of the variation of P_m with u. The dependence of P_m on u was determined based on a wide range of u, the relationship of P_m and u is considered

satisfactory. However as pointed by the later studies [113] that the simulated results have a poor agreement with the experimental data when using this equation (2.7) to predict the dependence of P_m on WC grain sizes (d). The linear relationship of P_m with $1/d$ was derived theoretically with the assumption of mono-sized solid WC grains with the same regular shape uniformly distributed in the liquid Co phase matrix. This assumption fails to hold in the true WC-Co system with a wide distribution in WC grain size and irregular shapes of WC grains. Therefore, the discrepancy between equation (2.7) and experiments is attributed to the linear dependence of P_m on d.

A recent study by Fan et al. [85] modified the relationship between liquid migration pressure and WC grain size through experimentally examining the equilibrium cobalt distribution in the liquid phase sintered WC-Co bi-layer samples, with each layer having different WC particle sizes. The corrected empirical equation of the liquid migration pressure, P_m as a function of liquid volume fraction, u and the WC grain size, d is expressed as:

$$P_m = 2048[(1/u - 1)^{1/3} - 1.41u]/d^{0.4} \tag{2.8}$$

Equation (2.8) is satisfactory to describe the variance of P_m with u, d in WC-Co systems with a stoichiometric carbon content. In order to describe the effects of the carbon content when WC-Co is not at stoichiometry, however, the equation has to include additional terms. In the work by Fan et al. [87], the equation (2.8) is modified to be:

$$P_m = 2048[(1/u - 1)^{1/3} - 1.41u]/d^{0.4} \times (1 + b_1\Delta x_{[C]} + b_2\Delta x_{[C]}^2) \tag{2.9}$$

where $\Delta x_{[C]}$ is the difference in the molar fraction of carbon in the liquid Co phase with respect to stoichiometry and b_1 and b_2 are empirical coefficients to be determined. In this work, the effect of the liquid phase composition on the liquid migration pressure was obtained through experimentally examining the equilibrium cobalt distribution in the liquid-phase-sintered WC-Co bi-layer samples, with each layer having a different controlled liquid phase composition. The dependence of P_m as a function of u, d and $\Delta x_{[C]}$ is thus obtained as:

$$P_m = 2048[(1/u-1)^{1/3} - 1.41u]/d^{0.4} \times (1 - 9\Delta x_{[C]} + 155\Delta x_{[C]}^2) \qquad (2.10)$$

The establishment of the dependence of the liquid migration pressure as a function of the volume fraction of liquid Co phase, carbon content, and WC particle size is valuable for the design and manufacture of functionally graded WC-Co composite materials. A desired Co gradient can be acquired by pre-designing a suitable gradient of the carbon, cobalt or WC particle size, which can be readily used to design various bi-layered, multilayered, or continuously graded structure of WC-Co [53, 55, 81-87].

2.4.3 Kinetics of Liquid Phase Migration

Since the liquid migration process not only depends on the thermodynamics but also relies on the kinetics of the process, the kinetics of migration process also needs to be established. As mentioned earlier, during the liquid phase sintering of WC-Co system, liquid Co phase flows under the action of the gradient of liquid migration pressure. Lisovsky [114] found that the flow of liquid was of laminar character and proposed that the liquid flux is proportional to the gradient of the liquid migration pressure. Using the

Navier-Stokes equation which is used to describe the flow of a viscous non-compressible liquid at constant temperature, he formulated the basic equation for the liquid flow under liquid phase migration pressure:

$$q = -k_m grad(P_m) \tag{2.11}$$

where q is liquid flow, k_m is the migration coefficient.

Based on equation (2.11) as well as on the law of conservation of mass, the differential equation that describes the mass transfer of the liquid phase by the mechanism of migration is derived,

$$\Phi(P_m)\frac{\partial P_m}{\partial t} = -k_m \nabla^2 (P_m) \tag{2.12}$$

where t is the time and ∇^2 is the Laplacian operator.

As applied to cylindrical bodies, equation (2.12) is transformed to be:

$$\Phi(P_m)\frac{\partial P_m}{\partial t} = -k_m[\frac{1}{r}\frac{\partial}{\partial r}(r\frac{\partial P_m}{\partial r}) + \frac{\partial^2 P_m}{\partial z^2} + \frac{1}{r^2}\frac{\partial^2 P_m}{\partial \varphi^2}] \tag{2.13}$$

where r is the radius, z is the coordinate, and φ is the angle.

Fan et al. [53] derived an equation to describe the LPM phenomenon, in which three assumptions were made: first, the solid phase skeleton is not rigid but flexible during the process; second, the grain shapes and sizes are held constant; and third, there is no chemical gradient within the system except that the volume fraction of the liquid phase may vary with locations. In the model, a moving coordinate in the direction of LPM was

used. In the coordinate, the motion at any point is relative to the solid phase skeleton at that point, and thus the velocity of the solid phase skeleton at any point is zero. Consequently, the volume change of the selected control volume results solely from imbibing the liquid, bridging the relations between the volume, the cross-sectional area, and the liquid volume fraction in the controlled volume. The governing equation of LPM was thus obtained and expressed as:

$$A_0(1-u_0)^{2/3}\frac{\partial(1-u)^{-2/3}}{\partial t}=-\frac{2}{3}\left[\frac{\partial}{\partial l}\left(\frac{k_P}{\mu}(\frac{1-u_o}{1-u})^{2/3}A_o\right)\frac{\partial P_m}{\partial l}+\frac{k_P}{\mu}(\frac{1-u_o}{1-u})A_o\frac{\partial^2 P_m}{\partial l^2}\right] \quad (2.14)$$

where A_o is cross-sectional area (m^2) perpendicular to the LPM direction at initial time; t is time, s; u is liquid volume fraction ($=V_l/((V_l+V_s)$, where V_l and V_s are liquid volume and solid volume, respectively); u_o is liquid volume fraction at initial time; l is the distance (m) in the LPM direction; k_p is the permeability of the system, which has the unit of m^2; μ is the viscosity of liquid, kg $m^{-1}s^{-1}$; P_m is the liquid migration pressure, P_a. Since P_m and k_p are both dependent on liquid volume fraction u, equation (2.14) is an equation with u as the dependent variable, and t and l as the independent variables.

This equation is the governing equation of LPM that can be applicable to many other material systems that satisfy the three basic assumptions with regard to the microstructure parameters. It is noted, however, the governing equation has been derived without any assumptions with regard to the microstructure parameters such as dihedral angle and the shape of solid grains. The effects of the microstructure parameters of the material system are implicitly considered by taking their effects on the values of P_m and k_p into account.

2.5 Review of Models

Process control performed by the trial and error method is expensive and time consuming. Theoretical simulation of the process is indispensable because it can reduce the amount of experimental efforts. Viewing this, a mathematic model has been built in this dissertation work. There are majorly two models that have contributed in developing the model, namely the model of the steel carburization process and the model of the moving boundary problem. The following sections will review both models.

2.5.1 Modeling of the Gas Carburizing Treatment of Steel

Gas carburizing process [10, 119, 120] is a case hardening process. Carbon is absorbed in the surfaces of steel parts. The resulting gradient of carbon content causes a gradient of hardness, producing a strong, wear resistant surface layer in the material. In gas carburizing, the source of carbon is carbon-rich atmosphere produced either from the gaseous hydrocarbons (for example, methane (CH_4), propane (C_3H_3), and butane (C_4H_{10})), or from vaporized hydrocarbon liquids. Usually the evaluation of the quality of the carburized steel components is based on the surface carbon content and the case depth of the carburized layer. To ensure a satisfactory quality of the carburized parts with stable performance reliability, it is necessary to understand the mechanism of carbon transport during the carburization process and then simulate this process.

2.5.1.1 Mechanisms of Carbon Transport

Figure 2.11 schematically shows the mass transfer mechanism in the carburizing [121-123]. It shows that the carbon transport from atmosphere to material proceeds in the following steps: (i) chemical reactions in the gas phase; (ii) carbon diffusion from the

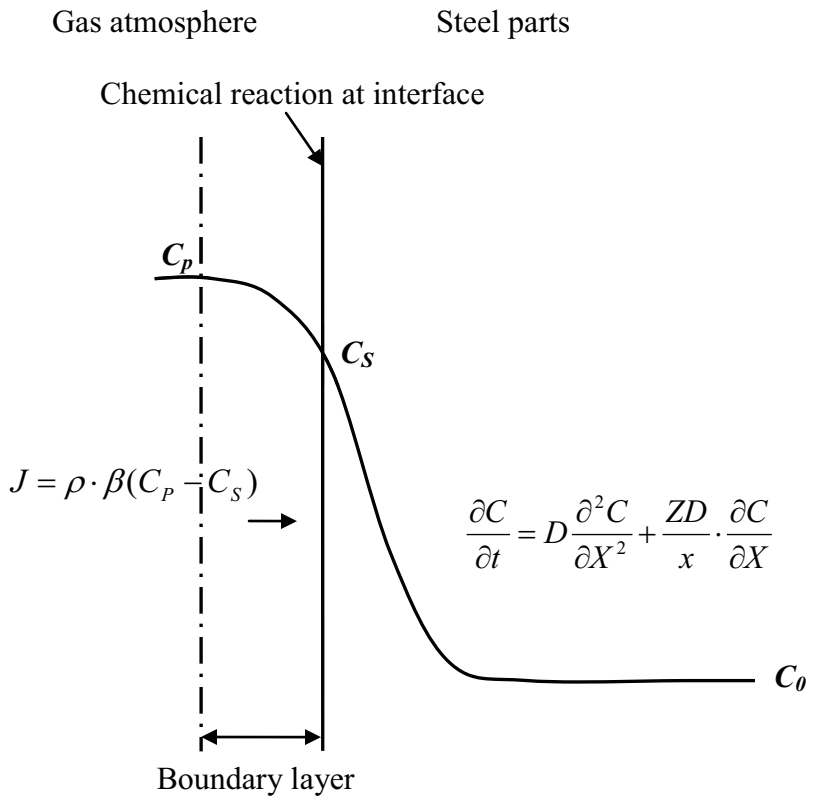

Figure 2.11 Schematic representation of carbon transport in carburization process.

atmosphere to the component surface through the boundary layer; (iii) surface chemical reaction; (iv) diffusion of carbon into the bulk of the material.

2.5.1.2 Formulations and Solutions

Formulations of the model of the gas carburization process depend on the assumption of the constant or nonconstant surface carbon composition.

When the rate of the carbon transfer from the atmosphere to the interface within the boundary layer is much faster than that of the diffusion within the material, it assumes that the carbon concentration at the surface (C_S) is constant and equals to the carbon

potential in the atmosphere (C_P) [124-126]. This assumption is justified since in that situation the carburization kinetics is controlled by the diffusion in the material which is the rate limiting process.

The carbon diffusion in materials is described by the Fick's second law. The diffusion coefficient (D) is assumed a constant independent of locations:

$$\frac{\partial C}{\partial t} = \frac{\partial}{\partial X}\left(D\frac{\partial C}{\partial X} \right) + u\frac{D}{r+uX}\cdot\frac{\partial C}{\partial X} \tag{2.15}$$

where C is carbon concentration as a function of time (t) and the distance (X). u=1 for concave surface, u=0 for plane surface, u=-1 for convex surface. r is the radius of the curvature. D is the diffusion coefficient.

For simplicity, it is considered a one-dimensional diffusion. To solve the diffusion equation (2.15), the simplest way is employing an analytical method [124] and the solution is obtained to be:

$$\frac{C - C_S}{C_0 - C_S} = erf\left(\frac{X}{2\sqrt{Dt}}\right) \tag{2.16}$$

where C_0 is the initial carbon content in the bulk, C_S is the surface concentration of carbon which is assumed to be equal to the atmosphere carbon potential (C_P).

In some circumstance, the carburization process is mixed controlled. The carbon concentration on the surface is not equal to the carbon potential in the atmosphere and is the combined results of the mass transfer in the gas boundary layer and the diffusion in the material [122, 123, 125, 127-136]. For example, in Rowan's model [134], the

carburizing process is modeled using a second-order parabolic partial differential equation for describing the carburization in the material and a set of boundary conditions accounting for the mass transfer coefficient at the surface and the kinetics of the interfacial reactions.

Based on the flux balance at the gas-material interface (Figure 2.11), it is assumed that the amount of carbon produced by the surface reaction is equal to the flux of carbon atoms at the surface, which is described by Fick's first law of diffusion:

$$\beta(C_P - C_S) = -D\frac{\partial C}{\partial X}\Big|_{Surf} \tag{2.17}$$

where β is the mass transfer coefficient of carbon transport within the boundary layer. C is the carbon content as a function of position X and time t. C_S is the surface concentration of carbon which is not equal to the atmosphere carbon potential C_P. D is the diffusion coefficient. From equation (2.17), the rate of carbon transport at the interface is directly proportional to the difference between C_S and C_P. Equation (2,17) serves as a boundary condition.

In this case, the carbon concentration profiles are computed iteratively and assuming a semi infinite geometry initially at uniform constant carbon concentration. The governing partial differential equation is expressed by the following finite difference equation:

$$C_i^{t+\Delta t} = \frac{\Delta t}{(\Delta x)^2}\left[D_i^t(C_{i-1}^t - 2C_i^t(\frac{(\Delta x)^2}{D_i^t \Delta t} - 2) + C_{i+1}^t) + \frac{(D_{i+1}^t - D_{i-1}^t)(C_{i+1}^t - C_{i-1}^t)}{4}\right] \tag{2.18}$$

where C corresponds to the carbon concentration at a particular location (node i) and specific time (t). ΔX is the space increment between the neighboring nodes and Δt is the time increment.

To account for the mass transfer at the interface, carbon concentration at the boundary nodes was computed as:

$$C_{surf}^{t+1} = \frac{\Delta X^2}{D \cdot \Delta t}\left[2\frac{\beta \Delta X}{D} \cdot C_P + (\frac{D\Delta t}{(\Delta X)^2} - 2\frac{\beta \Delta X}{D} - 2)C_{surf}^{t} + 2C_{x_1}^{t}\right] \tag{2.19}$$

There is a stability criterion needs to be fulfilled and is expressed as:

$$\Delta t < \frac{(\Delta X)^2}{2\beta \cdot \Delta X + 2D} \tag{2.20}$$

The governing diffusion equation (2.18) combined with the corresponding boundary equations can be solved numerically.

2.5.1.3 Choice of Kinetic Parameters

In order to solve the equations formulated above either analytically or numerically, it needs prior information regarding the kinetics or transport data. The primary kinetic parameters involve the carbon potential in the atmosphere (C_P), the carbon transfer coefficient in the boundary layer (β) as well the carbon diffusion coefficient (D) in the steel. Generally, these parameters are taken from literature or thermodynamic calculations. A brief review of the determination of these key parameters is given as follows.

The atmosphere carbon potential (C_P) is the amount of carbon in the atmosphere that is in thermodynamic equilibrium with the surface carbon content in the material. In thermodynamics, C_P can be calculated from the chemical reactions at given temperature and gas composition. The practical carburizing atmospheres are usually produced by mixing air and natural gas in a fixed proportion and composed of CO, CO_2, H_2O, CH_4, H_2, N_2, etc. [121-123, 127-131, 137-143]. Therefore the generation of carbon in the carburizing atmosphere is a complex process where various chemical reactions occur simultaneously. Three principle reactions contribute the most to the carbon transfer from atmosphere to the parts [122]:

$$2CO \rightarrow [C] + CO_2 \tag{2.21}$$

$$CH_4 \rightarrow [C] + 2H_2 \tag{2.22}$$

$$CO + H_2 \rightarrow [C] + H_2O \tag{2.23}$$

where $[C]$ represents the atomic carbon on the surface of treating parts.

Take the reaction (2.22) as an example to show how C_P is determined by the following equation [121]:

$$K_{eq} = \frac{C_P \cdot P_{H_2}^2}{P_{CH_4}} \tag{2.24}$$

where K_{eq} is the equilibrium constant. P_{H2} and P_{CH4} represent the partial pressure of hydrogen (H_2) and methane (CH_4).

According to the mechanism of the gas carburizing for steel, the mass transport from the atmosphere to the surface of the steel parts is through the boundary layer as shown in Figure 2.11. The carbon mass flux (J) in the unit of g $m^{-2}s^{-1}$ within the boundary layer can be expressed as:

$$J = \rho \cdot \beta(C_P - C_S) \tag{2.25}$$

where β is the mass transfer coefficient (m s^{-1}) in the boundary layer, ρ is the density of the part, C_P and C_S are the carbon potential in the atmosphere and carbon concentration at the surface of the material, respectively.

β is a value that describes the combined effects of all reactions that occurred within the boundary layer including the surfaced reaction, the mass transfer though the boundary layer, and the adsorption of atomic carbon by the surface [122, 123, 125, 127-136]. If the rates of the mass transport in the boundary layer and the surface adsorption are very large compared to the diffusion within the material, their effects can be neglected and the atmosphere carbon potential C_P equals to the carbon concentration C_S on the surface. However, if the mass transfer in the boundary layer is comparative to the mass diffusion in the material, the mass transfer coefficient β has an influence on the overall kinetics of carburization. Studies have shown that with the increase in β, both the case depth of the carbon gradient and the surface carbon content increase.

β relies mainly upon the gas carbon potential and the gas composition. To investigate the effects of the gas composition and gas carbon potential, several independent authors [127-131] measured β using thin foils in the carburizing atmospheres varied in ratios of CO and CO_2. Although some variances in the magnitude of β values, their findings

indicate a similar trend: (i) β changes drastically in the range of 0-30 % of each of these gas constituents; (ii) in such atmosphere, β is only slightly dependent on the atmosphere carbon potential. However, when the ratio of these gases is in the range of 30-70 %, β becomes independent of the atmosphere composition and is influenced by the carbon potential only.

Once the carbon atom is absorbed on the surface, the mechanism of the further carbon transport is determined by the carbon diffusion within the material. In the fundamental Fick's diffusion law, it uses the diffusion coefficient to describe the diffusion phenomenon. The diffusion coefficient (D) is considered as a proportional constant that depends on the nature of the substances. The carbon diffusion coefficient of a specific material varies both with carbon concentration and carburizing temperature. Extensive research [124, 134, 144-147] has been devoted to measure diffusion coefficient of carbon. For example, it was reported that the carbon diffusion coefficient in austenite as a function of the carbon concentration and temperature can be expressed in the following equation [146]:

$$D_{C(\gamma-Fe)} = (0.07 + 0.06C) \cdot \exp(\frac{-32000}{RT}) \tag{2.26}$$

where $D_{C(\gamma-Fe)}$ is the diffusivity of carbon in austenite. C is the carbon concentration in weight percent. T is the temperature in K. R is constant of 1.99 cal/mol/K.

Besides, diffusion of carbon is affected by the other alloying elements containing in the steel parts [145]. If the alloying elements tend to form more stable carbides than iron, the presence of these elements (like Cr, Mn, Mo, V) has a positive effect on the carbon

diffusion and the diffusion coefficient increases. However for a group of alloying elements (such as Si, Ni), they are not carbide formers and tend to decrease the diffusivity of carbon in steel. For low alloy steels, the influence of the alloying elements may be negligible, but for the medium- and high- alloyed alloys, their effects have appreciable influence to the total diffusivity. Presently little theoretical and experimental knowledge is available to quantitatively describe the effects of the alloying components on carbon diffusivity.

2.5.2 Modeling of Moving Boundary Problem

Boundary value problems occur in many engineering processes in which the solution has to satisfy certain conditions on the boundary of a prescribed domain. However, in many important processes involving the changing of states of matter, boundary separating different phases develops during the process. In these problems, the position of the boundary of the domain is not known in advance and has to be determined as part of the solution. The term “Moving Boundary Problem” is commonly used when the boundary is time dependent and the position of the boundary needs to be determined as function of time and space. Moving boundary problems are usually called Stefan problems, which were studied as early as 1831 by Lame and Clapeyron [148]. However, J. Stefan [149, 150] was given the major credit with reference to his work on the melting of the polar ice cap around 1890.

Many physical processes can be modeled as moving boundary problem [151-161]. The practical applications of the moving boundary problem are mainly but not exclusively concerned with heat transfer or mass diffusion incorporating a concurrent phase transformation, fluid flow in porous media, shock waves in gas dynamics and

cracks in solid mechanics. Moving boundary problem also occurs in many metallurgical processes, for example, heat treatment, electro-deposition, transient liquid phase bonding, aluminide coating, etc. [153, 155-161].

2.5.2.1 Formulation

The formulation of moving boundary problem requires not only the initial and boundary conditions to be known but also needs the boundary conditions at the moving interface [152, 154]. For explanation purpose, a simple example of moving boundary problems, ie., the melting of a semi infinite sheet of ice would be formulated and described. Although this simplified example may not reflect real moving boundary problem, it is very useful for illustrating the way of formulating the moving boundary problems.

A semi infinite sheet of ice is initially solid at a temperature (T_0) below the melting point (T_m). Subsequently, the surface of the ice sheet is heated and maintained at a constant temperature T_b, which is greater than the melting point, T_m. The melting of ice occurs immediately on the surface and it forms an interface separating a region of water from a region of ice. This moving interface moves from the surface into the ice-sheet. It is represented by $S(t)$ which is the position of the water phase at time t. X is the space coordinate measured from the outer surface of the sheet, X=0.

If $T_1(X, t)$ and $T_2(X, t)$, respectively, represent the temperature distributions in the water and ice phase at time t, the problem is to find the unknowns $T_1(X, t)$, $T_2(X, t)$, and $S(t)$ by solving the following set of heat flow equations:

$$\frac{\partial T_1}{\partial t} = \alpha_1 \frac{\partial^2 T_1}{\partial X^2},\ 0<X<S(t),\ t>0 \tag{2.27}$$

$$\frac{\partial T_2}{\partial t} = \alpha_2 \frac{\partial^2 T_2}{\partial X^2},\ S(t)<X<L,\ t>0 \tag{2.28}$$

where $\alpha=K_T/(\rho c)$ is thermal diffusivity. ρ is density. c is heat capacity and K_T is thermal conductivity. The subscripts 1 and 2 denote liquid water phase and solid ice phase, respectively. L is far boundary of the system.

The boundary equation and the initial equations are given as:

$$T(X,\ t)=T_b,\ X=0,\ t>0 \tag{2.29}$$

$$T(X,t)=T_0,\ X \to \infty,\ t \geq 0 \tag{2.30}$$

$$S(t=0)=0,\ t=0 \tag{2.31}$$

Two further conditions are needed on the moving boundary:

$$T_1=T_2=T_m,\ X=S(t) \tag{2.32}$$

$$K_T \frac{\partial T_2}{\partial X} - K_T \frac{\partial T_1}{\partial X} = \lambda \frac{dS}{dt},\ X=S(t) \tag{2.33}$$

where λ is latent heat of fusion per unit volume.

The equation (2.33) is also called the Stefan condition, which can be derived by referring to Figure 2.12, which shows the boundary moving a distance δX in time δt. In order to melt the ice contained per unit area perpendicular to X in the shaded region an

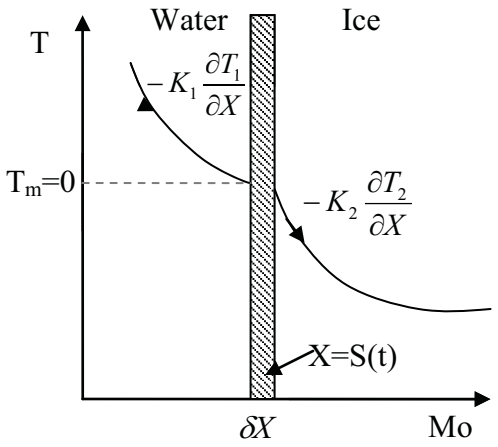

Figure 2.12 Schematic illustration of Stefan condition.

amount of heat ($\lambda \delta X$) is required. An amount of heat ($-K_T \delta t \delta T_1 / \delta X$) enters the shaded element from the water phase and ($-K_T \delta t \delta T_2 / \delta X$) escapes into the ice. Assuming there are no heat sources on the interface the heat balance of the shaded element requires that $K_T \partial T_2 / \partial X - K_T \partial T_1 / \partial X = \lambda \cdot dS / dt$, which is the equation (2.33).

2.5.2.2 Solution

Due to the wide range of applications of moving boundary problems in engineering and science, they have attracted considerable attention from the mathematicians to develop mathematical solutions to various moving boundary problems. Basically, the different solutions are classified into two categories: analytical and numerical solutions.

The Goodman's and Neumann's methods [152, 154] are well-known analytical methods. These analytical methods are mainly for the one-dimensional cases of an infinite or semi infinite region with simple initial and boundary conditions and constant thermal/diffusion properties.

As analytical solutions are frequently impossible for most engineering and scientific applications, numerical methods, such as finite difference methods are the most commonly used in solving moving boundary problems; however, in recent years, finite element methods and boundary elements methods have also been introduced. The advantage of finite element methods and boundary elements methods is their ability to handle complex geometries but they require more computation time and are less suitable to vectorisation and parallel computation than finite difference methods.

2.6 References

[1] Cherradi N, Kawasaki A, Gasik M. Compos Eng 1994;4:883.

[2] Mortensen A, Suresh S. Int Mater Rev 1995;40:239.

[3] Neubrand A, Roedel J. Z Metallkd 1997;88:358.

[4] Kieback B, Neubrand A, Riedel H. Mat Sci Eng 2003;362:81.

[5] Birman V, Byrd LW. Appl Mech Rev 2007;60:195.

[6] Bruet BJF, Juha S, Boyce MC, Ortiz C. Nat Mater 2008;7:748.

[7] Jandt KD. Nat Mater 2008;7:692.

[8] Messersmith PB. Science 2008;319:1767.

[9] Miserez A, Schneberk T, Sun C, Zok FW, Waite JH. Science 2008;319:1816.

[10] Davis JR. Surface hardening of steels. Materials park: ASM Int; 2002.

[11] Watanabe Y, Yamanaka N, Fukui Y. Compos A Appl Sci Manuf 1998;29A:595.

[12] Zhang J, Wang YQ, Zhou BL, Wu XQ. J Mater Sci 1998;17:1677.

[13] Jedamzik R, Neubrand A, Rodel J. J Mater Sci 2000;35:477.

[14] Watanabe Y, Eryu H, Matsuura K. Acta Mater 2001;49:775.

[15] Zhu JC, Lai ZH, Yin ZD, Jeon J, Lee S. Mater Chem Phys 2001;68.

[16] Won CW, Ahn JJ, Lee JH. J Mater Sci 2002;21:1407.

[17] Jin G, Takeuchi M, Honda S, Nishikawa T, Awaji H. Mater Chem Phys 2005;89:238.

[18] Burkes DE, Moore JJ. J Alloy Compd 2007;430:274.

[19] Jianguo L, Changjiang S, Zhenming X. Materials & Design 2007;28:1012.

[20] Peng XL, Yan M, Shi WT. Scripta Mater 2007;56:907.

[21] Tanaskovic D, Jokic B, Socol G, Popescu A, Mihailescu IN, Petrovic R, Janackovic D. Appl Surf Sci 2007;254:1279.

[22] Chen SP, Meng QS, Zhao JF, Munir ZA. J Alloy Compd 2009;476:889.

[23] Hassanin H, Jiang K. 23rd IEEE International conference on micro electro

mechanical systems, Piscataway, NJ, USA. 2010. p.368.

[24] Muller E, Drasar C, Schilz J, Kaysser WA. Metall Mater Trans A 2003;A362:17.

[25] Pompe W, Worch H, Epple M, Friess W, Gelinsky M, Greil P, Hempel U, Scharnweber D, Schulte K. Metall Mater Trans A 2003;A362:40.

[26] Witvrouw A, Mehta A. Mater Sci Forum 2005;492-493:255.

[27] Wosko M, Paszkiewicz B, Piasecki T, Prazmowska J, Paszkiewicz R, Szyszka A, Macherzynski W, Tlaczala M. 2006 International students and young scientists workshop: photonics and microsystems, Poland. 2006. p.69.

[28] Soderberg S. Scand J Metall 1997;26:65.

[29] Larsson C, Oden M. Materials Science & Engineering A (Structural Materials: Properties, Microstructure and Processing) 2004;A382:141.

[30] Liu Y, Wang HB, Long ZY, Yang JG, Zhang WZ. J Mater Sci 2005;40:5525.

[31] Taniguchi Y, Sasaki K, Ueki M, Kobori K. US Patent No.4830930, 1989.

[32] Okada Y, Sugawara J. US Patent No.5106674, 1992.

[33] Colin C, Durant L, Favrot N, Besson J, Barbier G, Delannay F. Int J Refract Met H 1993;12:145.

[34] Nakano M, Nomura T. US Patent No.5283030, 1994.

[35] Favrot N, Colin C, Besson J, Barbier G, Delannay F. 3rd International Symposium on Structural and Functional Gradient Materials, Switzerland. 1995. p.555.

[36] Greenfield MS. US Patent No.5623723, 1997.

[37] Put S, Vleugels J, Van der Biest O. Scripta Mater 2001;45:1139.

[38] Cheng JG, Wu YC, Xia YH. Mater Sci Forum 2003;423-425:45.

[39] Mirchandani PK, Keller BA. US Patent No.6511265, 2003.

[40] Tokita M. Mater Sci Forum 2003;423-425:39.

[41] Wei L, Xinde B, Yunhan L, Zuozhong J, Zhipeng X. Mater Sci Forum 2003;423-425:55.

[42] Colin M, Norgren S. Proceedings of the 16th international Plansee seminar, Metallwerk Plansee, Reutte, Austria. 2005.

[43] Yang JG, Wang HB, Liu Y, Huang BY, Zhang WZ. Journal of Central South University 2005;36:349.

[44] Matula G, Dobrzanki LA, Dozanska B. Int J Mater Prod Tec 2008;33:280.

[45] Li T, Li QF, Fuh JYH, Yu PC, Lu L. Int J Refract Met H 2009;27:95.

[46] Rassbach S, Moseley S, Bohlke S. Proceedings of the 17th international Plansee seminar, Metallwerk Plansee, Reutte, Austria, vol. 2. 2009. p.HM48/1.

[47] Konyashin I, Hlawatschek S, Ries B, Lachmann F, Sologubenko A, Weirich T. Int J Refract Met H 2010;28:228.

[48] Sorlier E, Colin C, Dourfaye A. Adv Mater Res 2010;83-86:810.

[49] Lisovsky AF. Int J Heat Mass Transf 1990;33:1599.

[50] Lisovsky AF, Gracheva TE. J Eng Phys 1990;59:1006.

[51] Delannay F, Pardoen D, Colin C. Acta Mater 2005;53:1655.

[52] Maximenko A, Roebben G, Van Der Biest O. J Mater Process Tech 2005;160:361.

[53] Fan P, Fang ZZ, Sohn HY. Acta Mater 2007;55:3111.

[54] Lisovsky AF. J Superhard Mater 2008;30.

[55] Fan P, Guo J, Fang ZZ, Prichard P. Metall Mater Trans A 2009;40:1995.

[56] Fischer UKR, Hartzell ET, Akerman J. US Patent No.4743515, 1988.

[57] Fischer UKR, Hartzell ET, Akerman J. US Patent No.4820482, 1989.

[58] Akerman J, Fischer UKR, Hartzell ET. US Patent No.5453241, 1995.

[59] Liu Y, Wang HB, Long ZY, Liaw PK, Yang JG, Huang BY. Mat Sci Eng 2006;426:346.

[60] Yohe WC. US Patent No.4548786, 1985.

[61] Yohe WC, Clemens M. US Patent No.4548786, 1985.

[62] Nemeth BJ, Grab GP. US Patent No.4610931, 1986.

[63] Upadhyaya GS. Cemented Tungsten Carbides - Production, Properties, and Testing. New Jersey: Noyes; 1998.

[64] German RM. Sintering theory and practice. New Jersey: Wiley; 1996.

[65] Guillermet AF. Metall Mater Trans A 1989;20A:935.

[66] Bolton D, Keely RJ. Int J Refract Met H 1982;1:103.

[67] Mchale AE. Phase diagrams for ceramists. Columbus: Ametical ceramic society; 1994.

[68] Gurland J. Journal of Metals 1954285.

[69] Fang Z, Eason JW. Int. J. Powder. Metall. 1993;29:259.

[70] German RM. Metall. Mater. Trans. A 1985;16A:1247.

[71] Engqvist H, Uhrenius B. Int J Refract Met H 2003;21:31.

[72] Exner HE, Walter A, Walter P, Petzow G. Metall 1978;32:443.

[73] Lee HC, Gurland J. Mat Sci Eng 1978;33:125.

[74] Sadangi RK, McCandlish LE, Kear BH, Seegopaul P. Int J Powder Metall 1999;35:27.

[75] Lee HR, Kim DJ, Hwang NM, Kim D-Y. J Am Ceram Soc 2003;86:152.

[76] Morton CW, Wills DJ, Stjernberg K. Int J Refract Met H 2005;23:287.

[77] Zheng Y, Liu WJ, Yuan Q, Wen L, Xiong WH. Switzerland, vol. 280-283. 2005. p.1413.

[78] Frisk K, Markstrom A. Int J Mat Res 2008;99:287.

[79] Sun L, Jia CC, Cao RJ, Lin CG. Int J Refract Met H 2008;26:357.

[80] Hashiva M, Kubo Y, Gierl C, Schubert WD. Proceedings of the 17th international Plansee seminar, Metallwerk Plansee, Reutte, Austria, vol. 2. 2009.

[81] Eso OO, Fang ZZ, Griffo A. Int J Refract Met H 2005;23:233.

[82] Fang ZZ, Eso OO. Scripta Mater 2005;52:785.

[83] Eso OO, Fang ZZ, Griffo A. Int J Refract Met H 2007;25:286.

[84] Eso OO, Fan P, Fang ZZ. Int J Refract Met H 2008;26:91.

[85] Fan P, Eso OO, Fang ZZ, Sohn HY. Int J Refract Met H 2008;26:98.

[86] Fan P, Fang ZZ. Int J Refract Met H 2009;27:37.

[87] Fan P, Guo J, Fang ZZ, Prichard P. Int J Refract Met H 2009;27:256.

[88] Liu Y, Wang HB, Yang JG, Huang BY, Long ZY. J Mater Sci 2004;39:4397.

[89] Yang JG, Wang HB, Liu Y, Zhang LQ, Li F, Long ZY. Chinese Journal of Nonferrous Metals 2004;14:424.

[90] Yong L, Haibing W, Yuehui H, Jiangao Y. Shrewsbury, UK. 2004. p.6 pp.

[91] Long ZY, Liu Y, He YH, Xiao YF, Zhou YG, Li F. Chinese Journal of Nonferrous Metals 2007;17:326.

[92] Liu Y, Liu FX, Liaw PK, He YH. Proceedings of AIP conference, USA, vol. 973. 2008. p.556.

[93] Xiao YF, He YH, Feng P, Xie H, Ma ZX, Zhang LJ, Huang ZQ, Huang BY. Chinese Journal of Nonferrous Metals 2008;18:465.

[94] Suzuki H, Hayashi K, Taniguchi Y. Trans Jpn Inst Met 1981;22:758.

[95] Chatfield C. Scand J Metall 1987;16:9.

[96] Schwarzkopf M, Exner HE, Fischmeister HF. Metall Mater Trans A 1988;A105-106:225.

[97] Yohe WC. Int J Refract Met H 1993;12:137.

[98] Tsuda K, Ikegaya A, Isobe K, Kitagawa N, Nomura T. Powder Metall 1996;39:296.

[99] Chen L, Lengauer W, Ettmayer P, Dreyer K, Daub HW, Kassel D. Int J Refract Met H 2000;18:307.

[100] Ekroth M, Frykholm R, Lindholm M, Andren HO, Agren J. Acta Mater 2000;48:2177.

[101] Andren H-O. Mater Chem Phys 2001;67:209.

[102] Frykholm R, Andren HO. Mater Chem Phys 2001;67:203.

[103] Frykholm R, Ekroth M, Jansson B, Andren HO, Agren J. Int J Refract Met H 2001;19:527.

[104] Frykholm R, Jansson B, Andren HO. Int J Refract Met H 2002;20:345.

[105] Lengauer W, Dreyer K. J Alloy Compd 2002;338:194.

[106] Frykholm R, Ekroth M, Jansson B, Agren J, Andren HO. Acta Mater 2003;51:1115.

[107] Lisovsky AF. Powder Metall Int 1987;19:18.

[108] Dullien FAL. Porous media: fluid transport and pore structure. San Diego: Academic Press; 1992.

[109] Lisovsky AF. Powder Metall Int 1990;26.

[110] Lisovskii AF. Sov Powder Metall Met Ceram 1991;30:10.

[111] Lisovsky AF. Sov Powder Metall Met Ceram 1991;30:183.

[112] Lisovsky AF. Metall Mater Trans A 1994;25A:733.

[113] Suresh S, Mortensen A. Fundamentals of functionally graded materials: processing and thermomechanical behaviour of graded metals and metal-ceramic composites. London: IOM Communications Ltd; 1998.

[114] Lisovsky AF. Powder Metall Met Ceram 1999;38:545.

[115] Lisovsky AF. J Superhard Mater 2001;23:1.

[116] Lisovsky AF. Sci Sintering 2004;36:81.

[117] Lisovskii AF. J Superhard Mater 2010;32:36.

[118] Lisovsky AF. Int J Refract Met H 1989;8:133.

[119] Carburizing and carbonitriding Metals park: ASM Int; 1977.

[120] Boyer HE. Case hardening of steel. Metals park: ASM Int; 1987.

[121] Colin R, Brachaczek M, Thulin D. J Iron Steel Int 1969.

[122] Collin R, Gunnarson S, Thulin D. J Iron Steel Int 1972;210:785.

[123] Collin R. 1975121.

[124] Goldstein JI, Moren AE. Metall Mater Trans A 1978;9A:1515.

[125] Gut S, Przybylowicz K. Defect diffusion forum, Liechtenstein, vol. 66-69. 1989. p.1401.

[126] Prasannan PC. Indian J Eng Mater S 1994;1:221.

[127] Moiseev BA, Brunzel YM, Shvartsman LA. Met Sci Heat Treat 1979;21:437.

[128] Munts VA, Baskakov AP. Met Sci Heat Treat 1980;22:358.

[129] Munts VA, Baskakov AP. Met Sci Heat Treat 1983;25:98.

[130] Sobusiak T. Proceedings of the 3rd International Congress on Heat Treatment of

Materials, Shanghai, China. 1984. p.1. 79.

[131] Stolar P, Prenosil B. Kovove Materialy 1984;22:348.

[132] Sproge L, Agren J. J Heat Treating 1988;6:9.

[133] Thete MM. Surf Eng 2003;19:217.

[134] Rowan OK, Sisson Jr RD. J Phase Equlib Diff 2006;27:598.

[135] Stasiek M, Ochsner A. Defect and diffusion forum, Laubisrutistr, Switzerland, vol. 258-260. 2006. p.366.

[136] Rowan OK, Sisson Jr RD. J Phase Equlib Diff 2009;30:235.

[137] Ellis T, Davidson IM, Bodsworth C. J Iron Steel Int 1963582.

[138] Grabke H. Metall Mater Trans B 1970;1:2972.

[139] Buslovich NM, Makhtinger EY, Mikhailov LA. Met Sci Heat Treat 1979;21:442.

[140] Grabke HJ, Mueller EM, Konczos G. Scripta Mater 1980;14:159.

[141] Grabke HJ. International high temperature corrosion conference, San Diego, CA, USA. 1983. p.287.

[142] Grabke HJ, Muller EM, Speck HV, Konczos G. Steel Res 1985;56:275.

[143] Grabke HJ, Prasannan PC, Mueller EM. Metall Mater Trans A 1986;17 A:915.

[144] Asimow RM. Trans Metall Soc AIME 1964;230:611.

[145] Blazek KE, Cost JR. Trans Jpn Inst Met 1976;17:630.

[146] Gustafson P. Scand J Metall 1985;14:259.

[147] Agren J. Scripta Mater 1986;20:1507.

[148] Lame MM, Clapeyron BPE. Ann Chem Phys 1831;47:250.

[149] Stefan J, Akad S. Wiss Wien 1889473.

[150] Stefan J. Ann Chem Phys 1891;42:269.

[151] Ockendon JR, Hodgkins WR. Moving boundary problems in heat flow and diffusion. London: Clarendon Press; 1975.

[152] Crank J. Free and moving boundary problems. London: Clarendon Press; 1984.

[153] Zhou YH, North TH. Model Simul Mater Sci Eng 1993;1:505.

[154] Zerroukat M, Chatwin CR. Computational moving boundary problems. England: Research Studies Press; 1994.

[155] Matan N, Winand HMA, Carter P, Karunaratne M, Bogdanoff PD, Reed RC. Acta Mater 1998;46:4587.

[156] Schuh CA. J Appl Phys 2002;91:9083.

[157] Shi Z, Guo ZX, Song JH. Acta Mater 2002;50:1937.

[158] Pasquale MA, Marchiano SL, Vicente JL, Arvia AJ. J Phys Chem B 2004;108:13315.

[159] Illingworth TC, Golosnoy IO. J Comput Phys 2005;209:207.

[160] Luozzo ND, Fontana M, Arcondo B. J Mater Sci 2007;42:4044.

[161] Li JF, Agyakwa PA, Johnson CM. J Mater Sci 2010;45:2340.

CHAPTER 3

PRINCIPLE OF THE NEW APPROACH

In this chapter, an atmosphere heat treatment process is described and analyzed based on the understanding of liquid phase migration and thermodynamic equilibrium in W-C-Co system. It was hypothesized that a Co gradient can be achieved by controlling diffusion of carbon transported from the atmosphere during sintering or during a post-sintering heat treatment. In principle, carburizing or decarburizing atmosphere heat treat process can be conducted to make FG WC-Co with reduced or enriched Co gradient in the surface region. The atmosphere heat treatment process of straight WC-Co (without other additions) following conventional liquid phase sintering will be verified.

The chapter is organized as follows: the first section describes the concept of this process. In the second and third sections, carburizing and decarburizing atmosphere heat treatments are designed respectively for creating a Co gradient near the surface of WC-Co composites. The principles and mechanisms of the cobalt gradation formation in both the carburization and decarburization processes are detailed.

3.1 Concept of the Process

Figure 3.1 [1] is a vertical section of a ternary phase diagram of W-Co-C system with 10 wt% Co. There is a three phase region in which WC, liquid cobalt, and solid cobalt co-exist as shown by the shaded area in Figure 3.1. At a given temperature within the three-

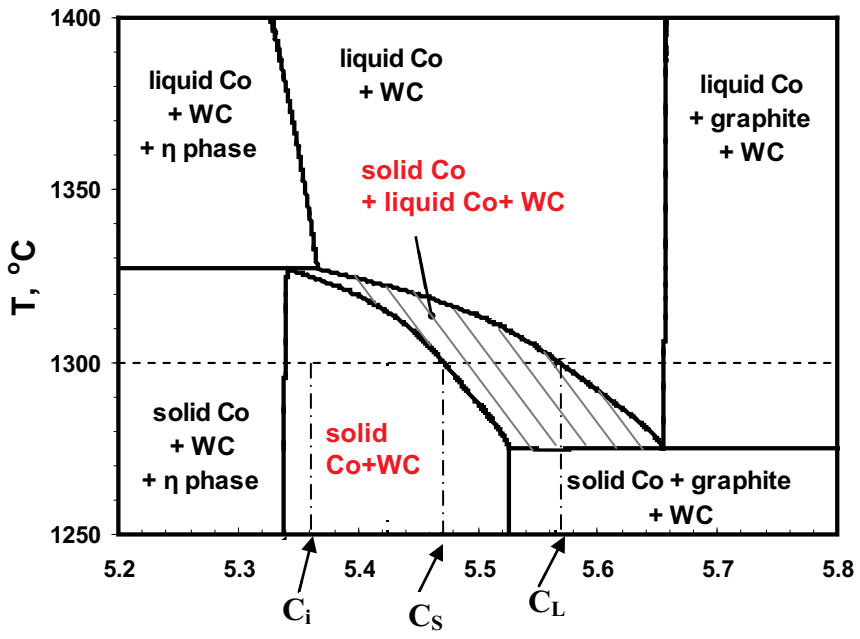

Figure 3.1 Vertical section of ternary phase diagram of W-C-Co at constant Co of 10 wt%, adapted from [1].

phase zone, the volume fraction of the liquid is a function of the carbon content. For example, at 1300°C, the volume fraction of the liquid phase with carbon content at point C_L (as marked in Figure 3.1), is maximum and at point C_S, the volume fraction of the liquid approaches zero. Thus, if there is a gradient of carbon content in a WC-Co material that traverses the range between point C_S and C_L, there will also be a gradient in the volume fraction of liquid, which would give rise to migration of the liquid Co phase. In this research, the carbon gradient is established by heat treating fully sintered WC-Co in a carburizing atmosphere or a decarburizing atmosphere.

For the WC-Co material that is heat treated in the carburizing atmosphere, it should have an initial carbon content that is less than C_L, and preferably less than C_S. During the carburization heat treatment, a small increase in the carbon content near surface will lead

to a carbon gradient between the surface and the interior and a significant increase in the liquid Co volume fraction near the surface. The increase of liquid Co in the surface region perturbs the balance of the liquid Co distribution, which in turn leads to migration of Co from the surface with more liquid Co towards the core with less liquid Co [2-4]. Therefore, a continuous Co gradient with a lower Co content near the surface is created.

For the WC-Co material treated under decarburizing atmosphere, it should have an initial carbon content that is more than C_S and preferably more than C_L. During the decarburization heat treatment, a small decrease in the carbon content near surface will lead to a carbon gradient between the surface and the interior and a significant decrease of liquid Co volume fraction near the surface. The decrease of liquid Co near surface breaks the balance of the liquid Co distribution and therefore induces the migration of Co from the interior region with more liquid Co towards the surface region with less liquid Co. Hence, a Co gradient with higher Co content near the surface is developed.

Note that there are three key underlying principles intrinsic to this method. One is that the liquid will flow from regions with a high volume fraction of liquid to that with a low fraction of liquid. The second is that the gradient of the volume fraction of liquid can be induced in-situ by introducing a carbon gradient in the material. The third is that a gradient in the volume fraction of liquid, as a function of the carbon gradient, is greatest within the temperature range in the three-phase zone in the phase diagram. The process for manufacturing FG WC-Co is thus designed to utilize those three principles in sync to maximize their effects on creating gradient microstructures. In the following sections, the feasibility of this process is demonstrated by both carburizing and decarburizing treatments of conventional fully sintered straight WC-Co.

3.2 Carburization Heat Treatment Process

The carburization heat treatment process is designed for creating a Co gradient near the surface of WC-Co composites. To validate the concept of this process, the heat treatments were conducted at three temperatures: 1400^{o}C, 1300^{o}C and 1250^{o}C. As noted previously in Section 3.1, 1300^{o}C was selected because it is within the three-phase temperature window. In comparison, 1400^{o}C is the typical liquid sintering temperature in the WC-Co(l) two-phase region, while at 1250^{o}C the system is completely solid. The treated samples were compared with the untreated samples to examine the effects of heat treatment.

3.2.1 Experimental

WC-Co powders with 10 wt% Co by weight were used in this study with a slightly substoichiometric carbon content (5.425 wt%). Tungsten powders were added to commercial WC powder to reduce the total carbon content. The powder mixtures were ball milled in heptane for four hours in an attritor mill. The milled powders were dried in a Rotovap at 80^{o}C and then cold-pressed at 200 MPa into green compacts with the dimension of 2x0.6x0.7 cm^{3}. The green compacts were sintered in vacuum at 1400^{o}C for one hour. The sintered specimen was cut into two halves before heat treatment. To avoid the influence of the atmosphere during sintering on surface compositions, only the cross sections of the cuts were used for analysis of the effects of heat treatment.

Carburizing heat treatments of the sintered samples (after being cut into halves) were conducted in atmospheres of mixed methane (CH_4) and hydrogen (H_2) with a ratio (P_{CH4}/P_{H2}^{2}) of 1/150 atm^{-1} at different temperatures for 60 min.

For analyzing microstructure and compositions of the samples, cross-sections of these specimens were polished and etched with Murakami's reagent. Cobalt concentration profiles perpendicular to the surface were measured using the energy dispersive spectroscopy (EDS) technique. Each data point of the cobalt composition reflects an averaged value obtained by scanning a 10x140 μm^2 rectangular area that was parallel to the surface. The rectangular area for measurement was spaced in 10 μm increment in the direction perpendicular to the surface. In this way, the measurement was performed to the depth of 150 μm from the original surface. The carbon content was excluded from quantitative analysis since EDS is not a suitable technique. The standard deviation of the data is approximately ± 0.36% of the average value of 10%, which is obtained by performing 40 repeated measurements on a standard WC-10 wt% Co specimen with uniform microstructure. These measurements were made at different locations on the cross-section of the standard specimen.

3.2.2 Results and Discussions

Figures 3.2 shows the effects of heat treatment temperature when the carbon potential of the atmosphere (expressed by P_{CH4}/P^2_{H2}) and heat treatment time were held constant. Before heat treatment, the microstructure of the WC-10Co specimen (Figure 3.2a) was homogeneous and there was no free carbon or η-phase in the microstructure. After heat treatment at 1300^{o}C, a microstructural gradient (Figure 3.2b) developed from the surface inward. This was demonstrated by the reduced amount of the phase with darker contrast (cobalt phase in the surface region) than that in the inner. This suggests that the cobalt content in the surface region is lower than that in the inner region. Free carbon was not observed, indicating that the carburization process was not excessive.

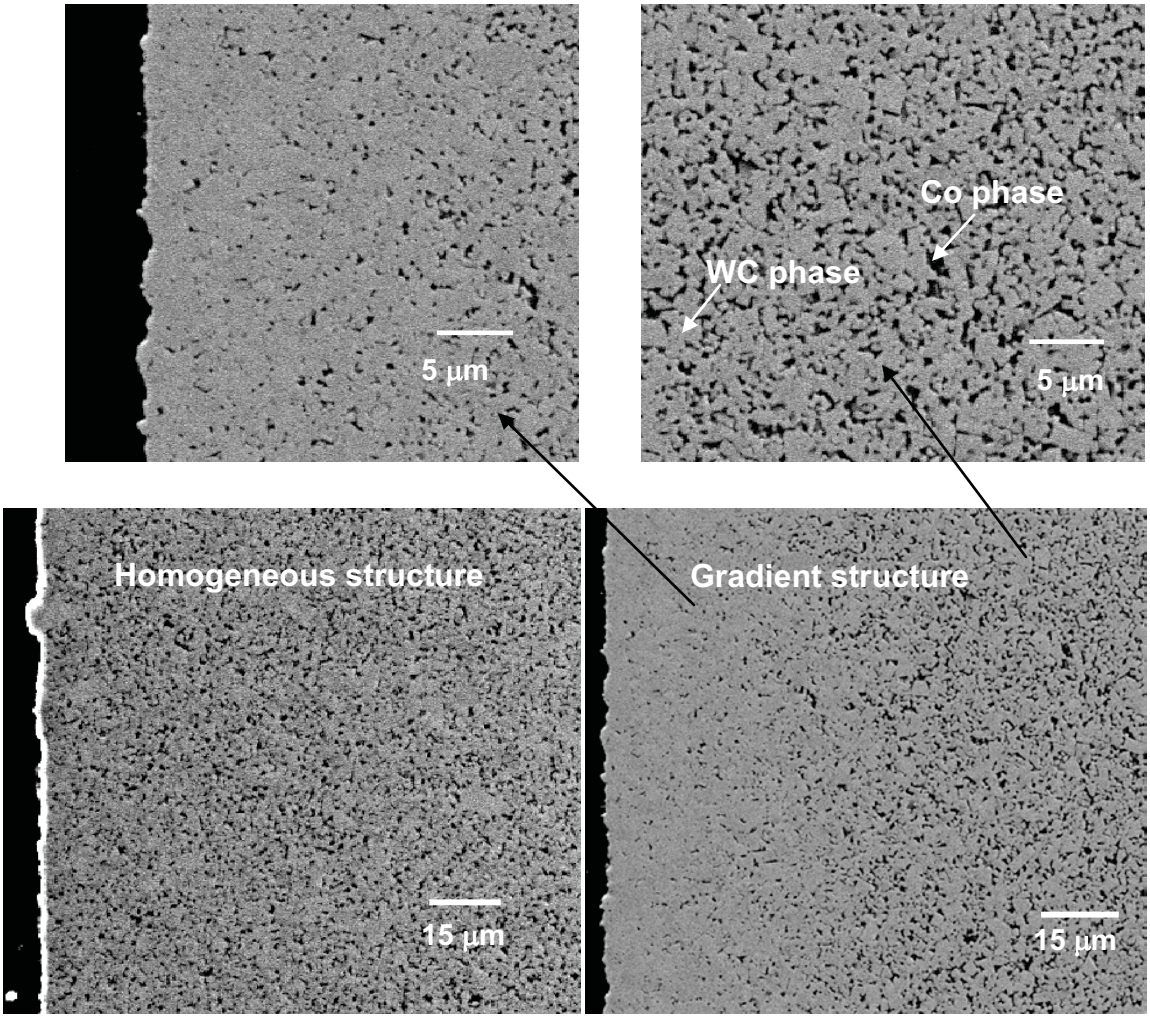

(a) (b)

Figure 3.2 Cross-sectional SEM micrographs of polished cross-sections of WC-10Co samples (a) before and (b) after heat treatment at 1300°C for 60 minutes in an atmosphere with $P_{CH_4}/P_{H_2}^2$ ratio of 1/150 atm^{-1}.

Figure 3.3 shows the Co concentration profiles of the heat treated WC-10Co specimens and the effects of temperature. For the specimen heat treated at 1300°C, there is a continuous Co gradient, while the Co profile in the specimen before treatment is flat. It is shown that within a depth of approximately 50 μm, the Co concentration increases gradually from about 5 wt% in the surface region to 10 wt% in the bulk of the sample. However, this trend of a Co gradient was not seen in the specimens treated at 1400 or 1250°C. When the specimen was heat treated at 1400°C (where total Co is in liquid) in the same atmosphere, a significant amount of free carbon was formed near the surface while no gradient was observed. Furthermore, when the specimen was treated at 1250°C in the same atmosphere, the microstructure showed essentially no change from its initial condition. There was neither a Co gradient nor free carbon phase that could be found.

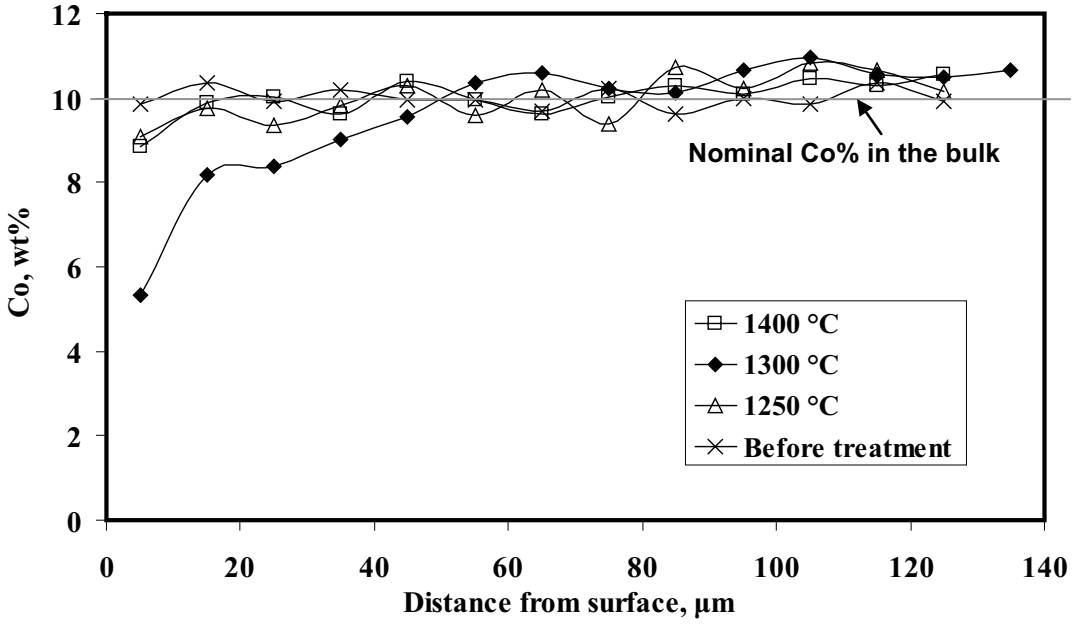

Figure 3.3 Cobalt concentration profiles of the sintered WC-10Co samples before and after heat treatments at temperatures of 1250, 1300 and 1400°C in the atmosphere of P_{CH4}/P_{H2}^2 ratio of 1/150 atm^{-1} for 60 minutes.

3.2.3 Mechanism of Cobalt Gradient Formation

The experimental results of this study clearly demonstrated that a Co-gradient in the surface region can be created by heat treating fully sintered WC-Co in a carburizing atmosphere. The formation of the Co gradient is the result of two processes: carbon diffusion due to the carbon gradient, and liquid Co migration induced by a gradient of the liquid phase as a function of the carbon content.

The mechanism of the Co gradient formation in the proposed process is explained schematically in Figure 3.4. In the WC-Co system with 10 wt% Co, over the temperature range from 1270^{o}C to 1325^{o}C, there is region in which Co(l)-Co(s)-WC(s) co-exist (Figure 3.1), and a small increase in carbon content will lead to a significant increase in the amount of liquid Co. Assuming specimen WC-10Co is heat treated at 1300°C, the initial overall-carbon-content of the specimen is at C_i (as denoted in Figure 3.1) and the corresponding initial carbon composition in Co phase throughout the material is $[C]_i$ (as denoted in Figure 3.4). Since the initial overall-carbon-content (C_i) of WC-Co sample is located in the Co(s)-WC(s) two-phase region, there is no liquid phase existing prior to the process at any given temperature within the range of the triple phase field (1300^{o}C, for instance). Before carburization begins, the carbon and cobalt contents are uniform throughout the entire specimen; thus the volume fractions of liquid cobalt and solid cobalt (V_S and V_l) in the surface region are equal to those in the core region, Figure 3.4a. Thus, the distribution of liquid cobalt is uniform between the surface and the interior. During heat treatment in a carburizing atmosphere, the carbon concentration in the cobalt phase near the surface is increased to $[C]_{Surf}$ (Figure 3.4b) as a result of the diffusion of carbon into the material, even though the carbon composition in the not yet affected core

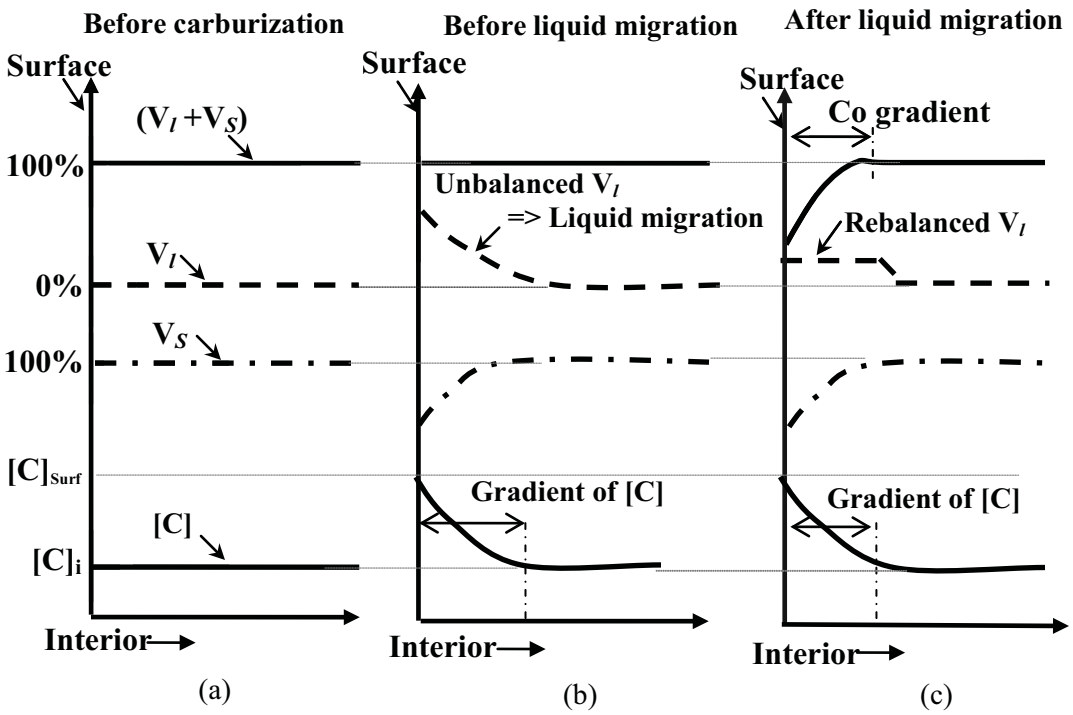

Figure 3.4 Schematic plots illustrating the formation of a Co gradient as a result of migration of liquid Co during carburizing heat treatment at 1300°C. (a) profiles of C concentration in Co phase ([*C*]), liquid Co volume fraction (V_l), solid Co volume fraction (V_s) and total amount of Co (V_l+V_s) before carburization, showing uniform distribution of C, Co, liquid Co and solid Co. (b) profiles of gradients of [*C*], V_l and V_S after carburization but before liquid migration occurs, showing imbalance of liquid Co distribution between carburized surface region and interior region. The imbalance of liquid Co distribution drives liquid Co to migrate from liquid-rich surface to liquid-poor interior. (c) profiles of the gradients of [*C*] and (V_l+V_s) after liquid migration, showing formation of Co reduced zone due to inward migration of liquid Co.

region is still homogeneous at $[C]_i$. Subsequent inward diffusion of carbon will result in the carbon profile shown in Figure 3.4b, where the carbon concentration ([*C*] in Figure 3.4) decreases as a function of depth from $[C]_{Surf}$ to the nominal value of $[C]_i$. When the carbon concentration in the Co phase is increased to a threshold value corresponding to the overall-carbon-content of C_S (as seen in Figure 3.1), the solid cobalt phase is partially transformed to liquid according to the phase equilibrium of W-C-Co system (Figure 3.1). It results in the increase in V_l and the decrease in V_S in the surface region; hence gradients

in V_S and V_l develop (Figure 3.4b). Consequently, the liquid cobalt will migrate from the surface region with more liquid cobalt towards the core region that has less liquid cobalt. It is noted that after reaching the equilibrium liquid cobalt distribution, the volume fraction of liquid cobalt in the surface region (with a lower total cobalt content and higher carbon content) is equal to that in the core region (with higher cobalt content and lower carbon content). Therefore, with the progress of surface-carburization, a cobalt gradient with reduced cobalt content in the carburized surface region is created, as shown in Figure 3.4c.

In contrast, a Co gradient was not formed when the WC-10Co specimen was heat treated at the typical liquid phase sintering temperature of 1400°C, at which there is a two-phase equilibrium between WC and liquid cobalt (Figure 3.1). Even though a carbon gradient would still form under the same carburizing atmosphere, it is difficult to induce liquid Co migration because there are little differences in terms of the volume fraction of the liquid phase at this temperature (Figure 3.5). As a result of the carburization treatment, near the surface region the carbon is saturated. Therefore, free carbon phase was observed in the peripheral surfaces of the specimen where the carbon content is oversaturated. Beyond this carbon saturated region, there is still a carbon gradient (Figure 3.5b). Based on our previous results [2-4], a liquid phase will usually migrate from a region with a higher carbon concentration to a region with a lower carbon concentration during the sintering of WC-Co, due to the effect of carbon concentration on the interfacial energy between the liquid phase and the solid WC grains. It is therefore reasonable to expect that a Co gradient may form as a result of the heat treatment. However, a Co gradient was not observed in the specimen that was treated at 1400°C. This can be understood on the basis

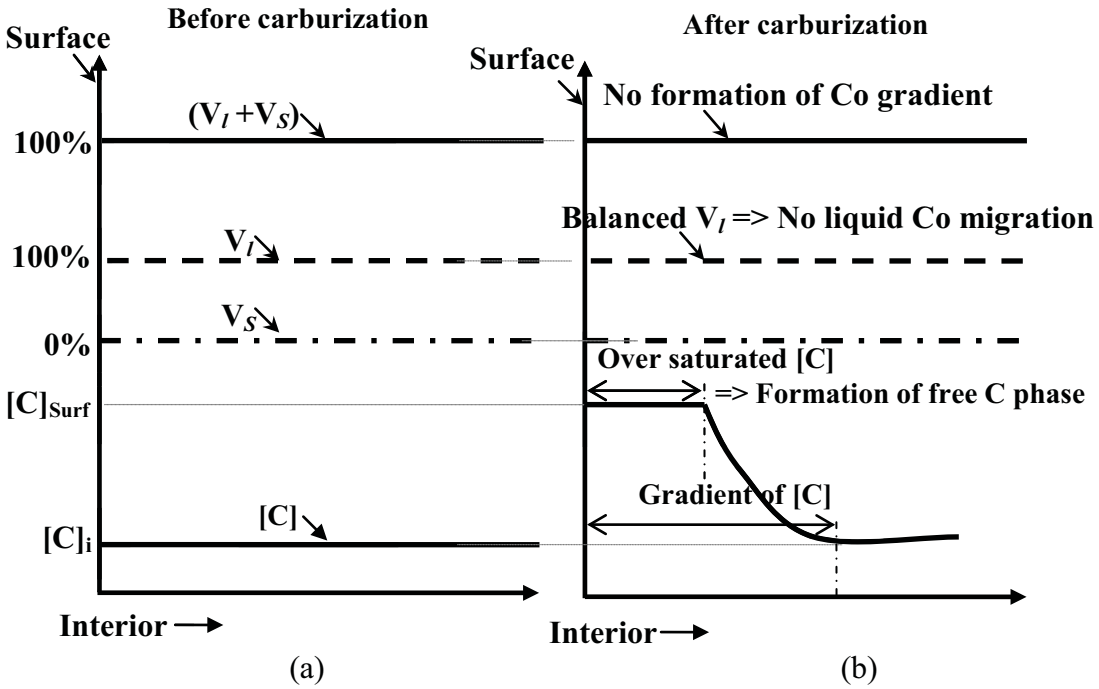

Figure 3.5 Schematic plots illustrating carburizing heat treatment at 1400°C. (a) profiles of C concentration in Co phase ([*C*]), liquid Co volume fraction (V_l), solid Co volume fraction (V_s) and total amount of Co (V_l+V_s) before carburization, showing uniform distribution of C, Co, liquid Co and solid Co. (b) profiles of [*C*], V_l and V_S after carburization, showing the uniform liquid Co distribution between the carburized surface region and the interior region thus no formation of Co gradient.

that the effect of carbon on the redistribution of the Co phase is limited. The previous work [4] has established that the differences in cobalt content induced solely by the difference in carbon content ranging from the stoichiometric carbon content to a super-stoichiometric carbon content (at the left boundary of the WC(s)-Co(l)-Graphite(s) field (Figure 3.1)) was less than 1.0 wt% Co. Therefore, any cobalt gradient that might form due to the difference in carbon content at this temperature is relatively minor. Further, when a specimen is held at 1400°C for a period of time that is sufficiently long for carbon diffusion and homogenization, there would be no gradient in the volume fraction of the liquid phase.

Finally, compared with the Dual Phase (DP) carbide process that was introduced in Section 2.3.2.1, the formation of a Co gradient in the new process is accomplished through a different mechanism. In our process, there is no η-phase present at any time during sintering and/or heat treatment. The heat treating temperature is uniquely selected to be within the three phase zone. In the DP carbide process, η-phase is required before heat treatment, and often continues to exist in the core region after carburization heat treatment. The heat treating temperature is, and must be, sufficiently high in the liquid phase sintering range to allow the reaction of η-phase with carbon. The reaction releases a significant amount of liquid Co, which will redistribute, resulting in a gradient within the material.

3.3 Decarburization Heat Treatment Process

The decarburizing atmosphere heat treatment process is designed for creating an enriched Co gradient in the surface region of WC-Co composites. A systematic experimental study was conducted to examine the effects of the cooling rate, atmosphere and carbon content of WC-Co on the formation of Co gradient.

3.3.1 Experimental

Straight WC-Co materials with two different carbon contents were used in this study. Symbols $10Co_{(C+)}$ and 10Co are used to designate specimens with super-stoichiometric carbon (5.66 wt%) content and stoichiometric carbon content (5.51 wt%), respectively. Commercially available WC-Co mixed powders with 10 wt% Co were used as the starting raw material for 10Co, while graphite powder was added to the WC-Co mixed powders to increase the total carbon content to above the stoichiometric value for

$10Co_{(C+)}$. Powder mixtures were ball milled in heptane for 4 hours in an attritor mill. After milling, the powders were dried in a Rotovap at 80°C and then pressed under 200 MPa into green compacts with dimension of $2 \times 0.6 \times 0.7$ cm^3. The samples were liquid-phase sintered in vacuum at 1400°C for 1 hour. Those specimens were then heat treated in atmospheres designed to generate Co gradient under various atmospheres at 1300°C.

The fully sintered specimens were heat treated in a tube furnace. The atmosphere in the reaction tube was either decarburizing or neutral, controlled by adjusting the ratios of methane (CH_4) to hydrogen (H_2) in the gas mixture using digital mass flow meters. The treatment was conducted at 1300°C, except for Run 6 at 1315°C. The temperature of 1300°C was selected such that the treatment would take place in the phase region in which WC, liquid Co and solid Co coexist, as illustrated in the vertical section of the ternary phase diagram of W-Co-C system with 10wt%Co (Figure 3.1).

In the initial tests, the specimens were directly heated to 1300°C and held at that temperature for 1 hour and then cooled either rapidly or slowly in the decarburizing atmosphere. No gradient structure was observed in these specimens. It can be understood based on the surface decarburization of the specimens during heating up, which increases the liquid forming temperature of the surface region to above the selected holding temperature, resulting in no or very low fractions of liquid Co in the surface region, thus blocking any liquid Co migration.

A different heat treatment procedure was then designed. Specimens were heated to 1400°C at 20°C/min and held at this temperature for 2 minutes, in order to ensure that there is liquid phase on and near the surface. The specimens were then cooled down to selected holding temperatures (1315°C for Run 6, 1300°C for other runs) at 10°C/min and

held at that temperature for 60 minutes. Thereafter, the samples were cooled down to room temperature with selected cooling rates, 5°C/min above 1200°C for slow cooling or 50°C/min above 1200°C for rapid cooling. Below 1200°C, the cooling rates were not controlled. However, the actual cooling rates at the temperature below 1200°C were18-25 °C/min until 800°C, 6-9°C/min until 500°C, then 3-4°C/min until room temperature. After heat treatment, the cross-sections of the treated specimens were polished and examined using optical microscopy and scanning electronic microscopy techniques.

After heat treatment, the Vickers hardness values as measured in the center of the specimens using a 30 Kg load were 1334 and 1343 Kg/mm^2 for $10Co_{(C+)}$ and $10Co_{(o)}$ materials, respectively. The WC grain size measured in the center of the specimen was approximately 1.3 μm (intercept length) for both materials. Table 3.1 summarizes the heat treatment conditions conducted in this study. The presence or absence of Co-capping in different specimens is also listed.

Table 3.1 Heat treatment conditions and observed Co-capping

Run #	Composition	Hold temperature	Atmosphere	Cooling	Co-capping & its morphology
1	$10Co_{(C+)}$	1300°C	decarburizing	slow	yes continuous
2	$10Co_{(C+)}$	1300°C	decarburizing	rapid	yes continuous
3	$10Co_{(C+)}$	1300°C	neutral	slow	no
4	$10Co_{(C+)}$	1300°C	neutral	rapid	no
5	10Co	1300°C	decarburizing	slow	yes non-continuous
6	10Co	1315°C	decarburizing	slow	yes continuous

Note: a) Atmosphere: $P_{CH_4}/P_{H_2}^2 = 1/2000$ atm^{-1} for decarburizing one; $P_{CH_4}/P_{H_2}^2 = 1/1000$ atm^{-1} for neutral one.
b) Cooling: 5°C/min for slow one; 50°C/min above for rapid one.

3.3.2 Results and Discussion

3.3.2.1 Effect of Cooling Rate

First, the effects of cooling rate were examined by comparing test Runs 1 and 2 as shown in Table 3.1. The carbon content, atmosphere, and temperature were kept to be the same for the tests Run 1 and Run 2. However, the cooling rate used in Run 1 was lower (5°C/min above 1200°C) than that in Run 2 (about 50°C/min above 1200°C). It was observed that a thin layer of Co, referred to "Co-capping", formed in both cases.

Figures 3.6 and 3.7 are the microscopic images of the specimen in Run 1 before and after the heat treatment, clearly demonstrating the presence of Co-capping. In these micrographs, WC appears in gray surrounded by Co matrix in slightly darker contrast. Free-carbon phase was also visible as small black spots.

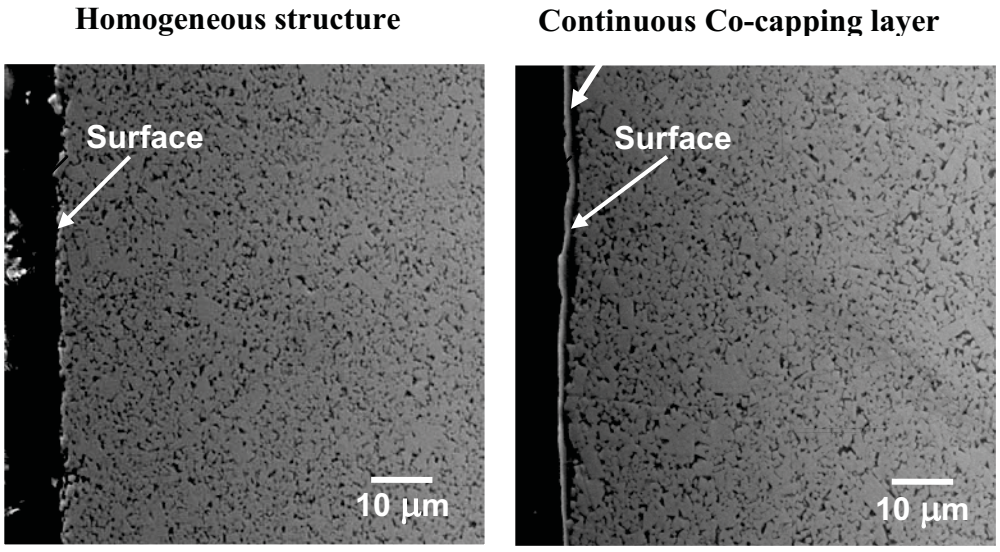

Figure 3.6 Cross-sectional SEM micrographs of the super-stoichiometric specimen (from Run 1) (a) before treatment and (b) after decarburizing heat treatment followed by slow cooling.

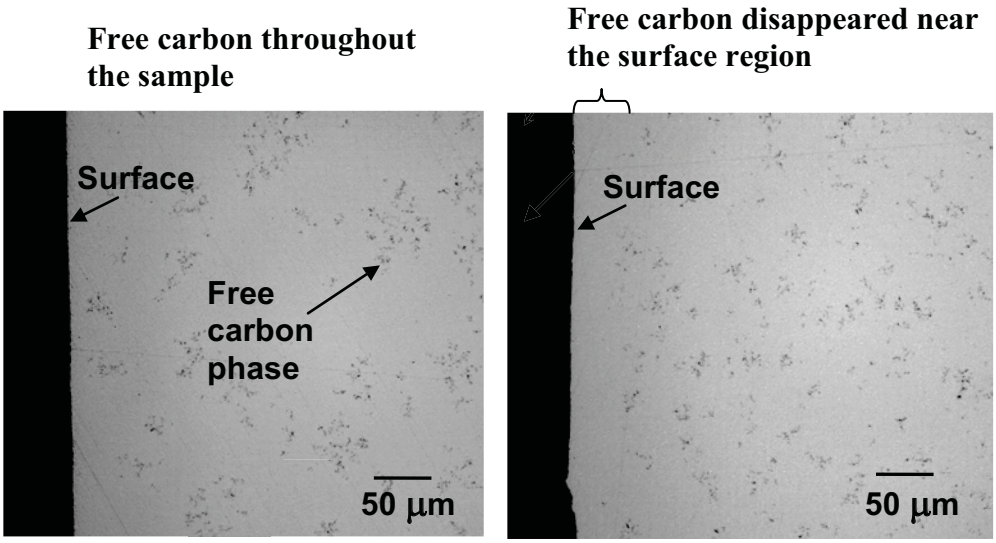

Figure 3.7 Cross-sectional optical micrographs of the super-stoichiometric specimen (from Run 1) (a) before treatment and (b) after decarburizing heat treatment followed by slow cooling.

Before the heat treatment, the microstructure of the specimen of Run 1 was uniform. There was free-carbon distributed throughout the microstructure because the total carbon content of the specimen was substantially above the stoichiometric value (as shown in Figures 3.6a and 3.7a). After the heat treatment, a thin continuous layer of Co phase, namely Co-capping layer, formed on the outermost surface (Figure 3.6b). Note that the carbon phase in the inner part was unaffected, while the carbon phase disappeared in the peripheral surface region (Figure 3.7b), indicating a decarburization of the surface region during the heat treatment in the decarburizing atmosphere. The microstructure of the specimen of Run 2 (Figure 3.8) is similar to that of Run 1 with Co-capping, indicating that the cooling rate changing from 5°C/min to 50°C/min had little influence on the formation of Co-capping.

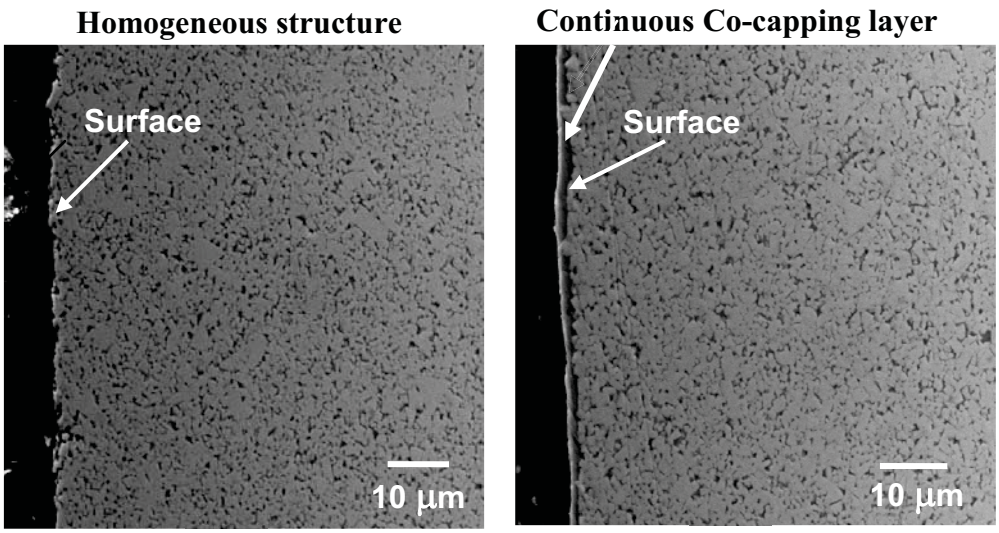

Figure 3.8 Cross-sectional SEM micrographs of the super-stoichiometric specimen (from Run 2) (a) before treatment and (b) after decarburizing heat treatment followed by rapid cooling.

3.3.2.2 Effect of Atmosphere

The effects of atmosphere on Co-capping were studied by comparing the results of heat treatments in decarburizing (Runs 1 and 2) and neutral atmosphere (Runs 3 and 4). The carbon activity in the neutral atmosphere with the P_{CH4}/P_{H2}^2 ratio of 1/1000 atm^{-1} was approximately equal to that in the specimen at the holding temperature, such that neither carburizing nor decarburizing would occur during heat treatment in the neutral atmosphere.

After the treatment in the neutral atmosphere, followed by either slow cooling (Run 3) or rapid cooling (Run 4), Co-capping was not observed, as shown in Figure 3.9 for Run 3 and Figure 3.10 for Run 4. The examination of the microstructures of Runs 3 and 4 showed that the free-carbon phase throughout the material was unaffected, indicating that neither carburizing nor decarburizing occurred during the heat treatment in the selected

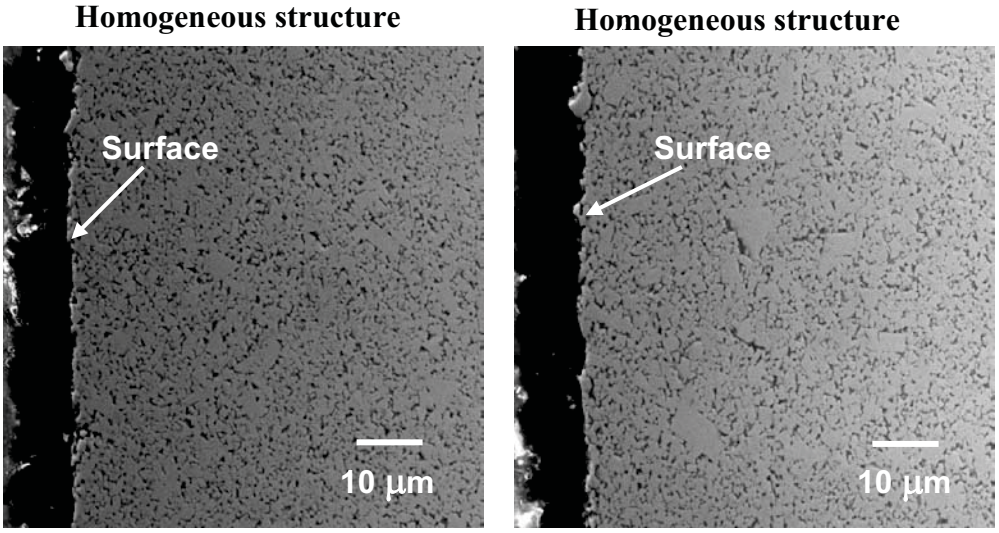

(a) (b)

Figure 3.9 Cross-sectional SEM micrographs of the super-stoichiometric specimen (from Run 3) (a) before treatment and (b) after heat treatment in neutral atmosphere followed by slow cooling.

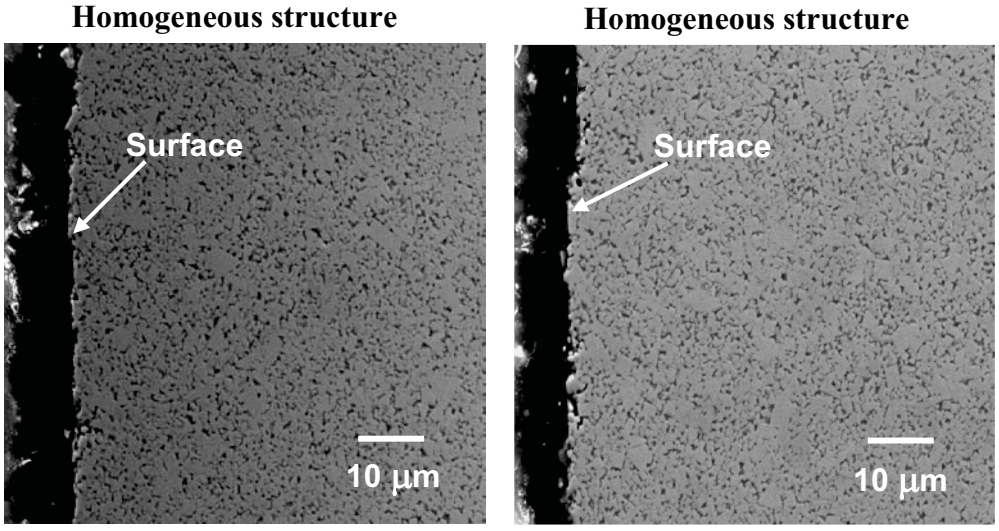

(a) (b)

Figure 3.10 Cross-sectional SEM micrographs of the super-stoichiometric specimen (from Run 4) (a) before treatment and (b) after heat treatment in neutral atmosphere followed by rapid cooling.

neutral atmosphere. By considering this result with that of Runs 1 and 2, which was performed under decarburizing atmosphere, it can be inferred that without surface decarburization, Co-capping would not form. In other words, the decarburizing atmosphere and the resultant surface decarburization are critical for the formation of Co-capping.

3.3.2.3 Effect of Carbon Content in Specimen

In the test Run 5, the specimen with stoichiometric carbon (designated as 10Co) was treated under the same conditions as for the super-stoichiometric specimen ($10Co_{(C+)}$) in Run 1. The microstructure of the 10Co specimen before and after treatment is shown in Figure 3.11. Before the treatment, the structure was uniform and there was no free-carbon. After the treatment, Co-capping was observed in various sections on the surface. However, the Co-capping did not form a continuous layer as observed in the $10Co_{(C+)}$ specimen. Except for this non-continuous Co-capping layer, the microstructure showed little change from its initial state. In the test Run 6, the heat treatment temperature was increased to 1315^{o}C, while the other experimental conditions were maintained as in Run 5. It was found that a continuous Co-capping layer formed after the heat treatment (Figure 3.12).

3.3.3 Mechanism of Cobalt Gradient Formation

Based on the above experimental results, a mechanism for the formation of Co-capping is proposed based on the migration of liquid cobalt phase. The driving force for the redistribution of liquid Co during sintering or heat treatment at high temperatures is the reduction of interfacial energy. It was mentioned in Section 2.4, liquid Co migration

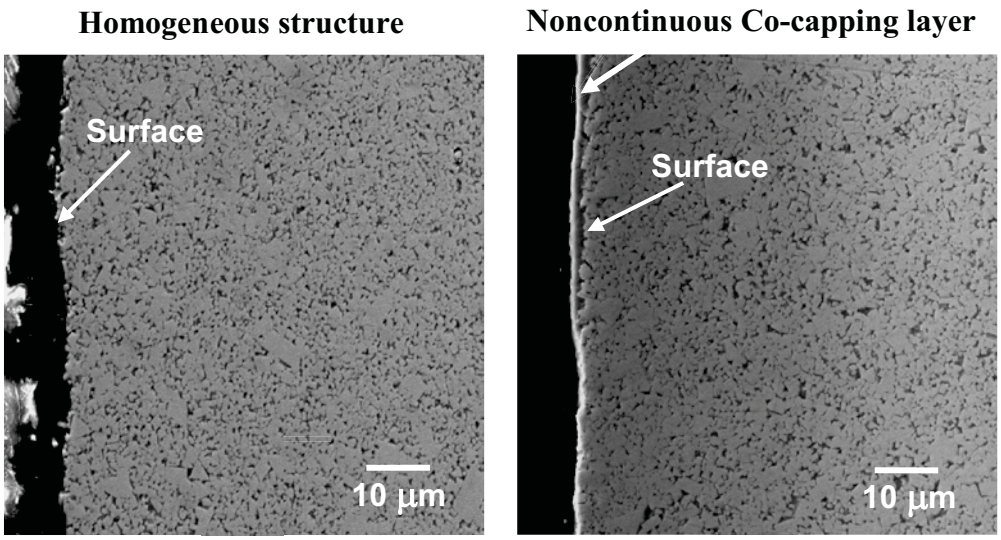

Figure 3.11 Cross-sectional SEM micrographs of the super-stoichiometric specimen (from Run 5) (a) before treatment and (b) after decarburizing heat treatment at 1300°C followed by slow cooling.

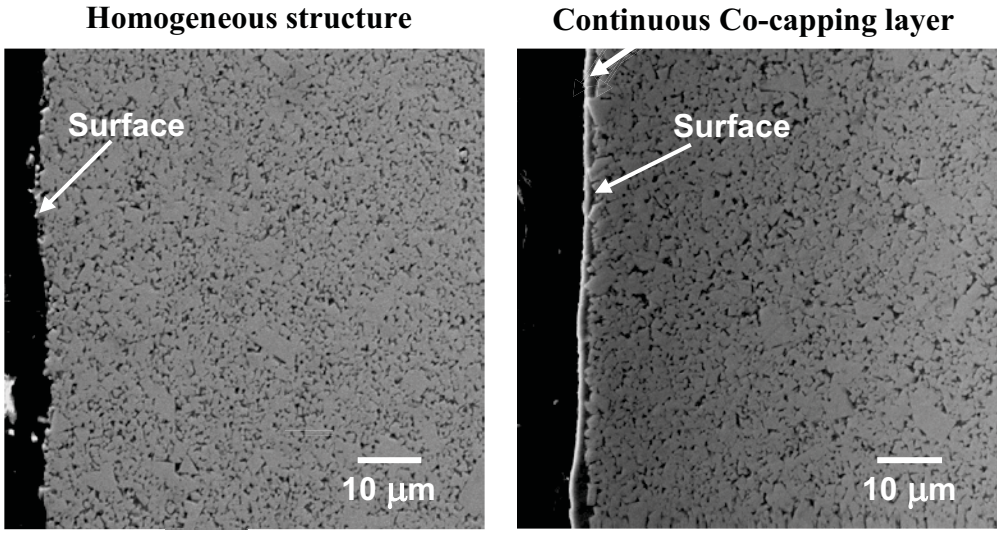

Figure 3.12 Cross-sectional SEM micrographs of the specimen with super-stoichiometric carbon content (from Run 6) (a) before treatment and (b) after decarburizing heat treatment at 1315°C followed by slow cooling.

or liquid Co redistribution is an interfacial-energy-driven flow dependent on three main factors – volume fraction of liquid Co, grain size of WC, and carbon content in liquid Co for straight WC-Co systems. During liquid phase sintering, liquid cobalt tends to migrate from a region with more liquid Co, coarser grain size, and higher carbon content towards a region with less liquid Co, finer WC grain size, and lower carbon content in liquid cobalt.

In the case of Co enrichment and Co-capping during the heat treatment in decarburizing atmosphere, it is reasonable to consider that the observed outward liquid Co migration is driven by the decrease of liquid Co in the surface region induced by the surface-decarburization, of which the mechanism can be explained with the help of the schematics in Figure 3.13. Initially, assuming that a WC-Co specimen is held at a temperature T (for example, 1300°C) between the liquidus and solidus temperatures, the volume fractions of liquid Co and solid Co (V_l and V_s) are uniform in the whole specimen. In other words, the distribution of liquid Co is balanced between the surface region and the interior region, as shown in Figure 3.13a. With the progress of the surface decarburization, the carbon content of liquid Co in the surface region decreases and the solidification temperature of liquid Co in this region is increased accordingly to above the present temperature T, as shown in Figure 3.13b. Thus, the liquid phase in the surface region is undercooled due to the surface decarburization, which will consequently solidify. The solidification of the undercooled liquid Co in the surface region decreases the volume fraction of the liquid Co and increases the volume fraction of solid Co, resulting in less liquid Co in the surface region than that in the interior region, as shown in Figure 3.13c. The imbalance of liquid Co distribution between the surface region and the interior

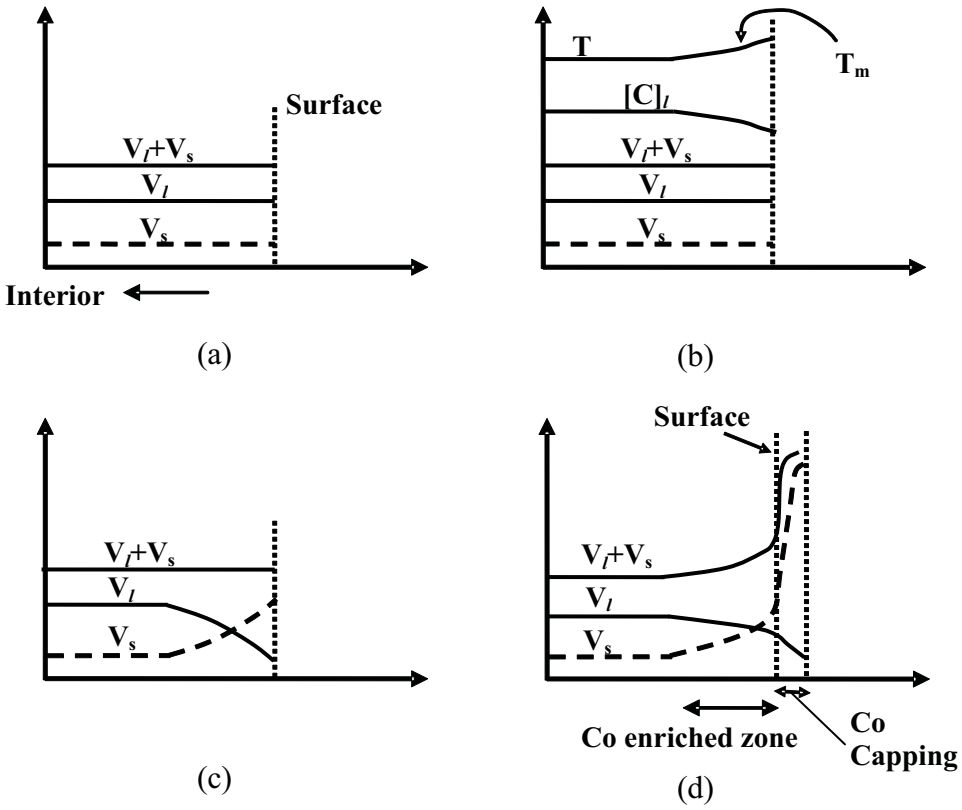

Figure 3.13 Schematic plots showing the formation of Co enriched zone and Co-capping due to the migration of liquid Co during heat treatment in decarburizing atmosphere. (a) profiles of liquid Co volume fraction, V_l, and solid Co volume fraction, V_S, before decarburization. (b) profiles of solidification temperature, T_m, and carbon content, $[C]_l$, after decarburization. (c) profile of liquid Co volume fraction, showing the broken balance of liquid Co distribution. (d) profiles of volume fractions of liquid Co and solid Co, showing the formation of Co enriched zone and/or Co-capping due to outward migration of liquid Co.

region drives the liquid Co to migrate from the interior towards the surface until the balance of liquid Co between the two regions is re-established. Further, the Co migrated from the interior region will be also decarburized in the near surface region and solidifies, the balance of liquid Co will be broken again and more liquid Co will migrate from interior towards the surface. Thus, with the progress of the surface decarburization, a Co enriched zone and/or Co-capping can be formed, as shown in Figure 3.13d.

The observed effects of various factors on the formation of Co-capping in this study can be reasonably explained using the above proposed mechanism. As described in Section 3.3.2.1, it was found that the cooling rate did not affect the morphology of Co-capping. This is understandable because the Co-capping in this study was formed while being held at a fixed temperature. As described in Section 3.3.2.2, no Co-capping was formed in neutral atmosphere. This is also understandable because Co would not migrate towards the surface when there was no surface decarburization.

Further, in contrast to that, a continuous Co-capping was formed on the specimen with super-stoichiometric carbon content, a noncontinuous Co-capping was formed on the stoichiometric specimen at the same holding temperature, while a continuous Co-capping was formed on the stoichiometric specimen at a higher holding temperature. This phenomenon can be explained by the different amounts of liquid Co in the specimens of the two compositions. As shown in the phase diagram of WC-Co (Figure 3.1), at the same holding temperature of 1300°C, the amount of liquid Co is higher in the specimen with super-stoichiometric carbon composition than that in the stoichiometric specimen. In fact, at 1300°C, all Co in the super-stoichiometric specimen is in liquid state, while around 50% of Co in the stoichiometric specimen is in solid state, based on the phase diagram. Less liquid Co in the stoichiometric specimen is considered to slow the kinetic rates of surface decarburization and liquid migration, thus resulting in less and non-continuous Co-capping microstructure. At the temperature of 1315°C, however, all Co in the stoichiometric specimen is in liquid state. Thus, the kinetic rates of surface decarburization and liquid migration are sufficiently fast for the formation of a continuous Co-capping layer.

Based on the proposed mechanism, there are two critical factors for the Co enrichment and/or Co-capping to form in straight WC-Co materials. One is that the atmosphere needs to be decarburizing; and the other is that the temperature needs to be in the 3-phase region, i.e., 1275-1325°C according to the phase diagram of WC-Co system. Since the conventional liquid phase sintering of WC-Co is usually conducted in vacuum, the carbon activity of the residual gas in the furnace chamber is expected to be very sensitive to many difficult-to-control parameters such as moisture level, raw materials, crucibles, and adsorbed air in the chamber. The carbon activity of the residual gas is also expected to vary from one location to another in the furnace chamber on different surfaces of a single product. Thus, it is understandable that the formation of Co-capping may vary from part to part and from one furnace run to another. Therefore, it is extremely difficult to predict whether Co-capping will form on a specific WC-Co product in a specific sintering run under conventional vacuum sintering conditions. In order to prevent Co-capping from forming, nondecarburizing atmosphere should be employed at least during the cooling from sintering temperatures. The pressure in the furnace chamber should not be too low as during the conventional vacuum liquid-phase-sintering process to control the carbon activity. Caution must also be taken, however, to prevent excess carburization of the sintered products.

3.4 Conclusions

An atmosphere heat treatment process for manufacturing FG WC-Co with Co concentration gradient in the surface region was developed. Gradients with either reduced Co content or enriched Co content were formed on the surface of WC-Co specimens as a result of carburizing or decarburizing heat treatment, respectively. The treating

temperature for both the carburization and decarburization processes should be within the range in which solid WC, solid Co, and liquid Co coexist. The process was designed based on the principles of liquid phase migration and the dependence of the liquid volume fraction on carbon gradient in the three phase zone. The formation of the Co gradient or Co redistribution was attributed to the imbalance of liquid phase distribution and the subsequent re-establishment of the balance of liquid distribution through the migration of liquid Co from the liquid-rich region towards the liquid-poor region.

3.5 References

[1] Guillermet AF. Metall Mater Trans A 1989;20A:935.

[2] Fan P, Eso OO, Fang ZZ, Sohn HY. Int J Refract Met H 2008;26:98.

[3] Fan P, Guo J, Fang ZZ, Prichard P. Int J Refract Met H 2009;27:256.

[4] Fan P, Guo J, Fang ZZ, Prichard P. Metall Mater Trans A 2009;40:1995.

CHAPTER 4

EXPERIMENTAL STUDY

In this chapter, systematic experiments were carried out to gain a comprehensive understanding of the carburization heat treatment process. It is organized as follows: the first section is focused on investigating the effects of key process parameters (heat treating atmosphere and heat treating time) on the kinetics of Co gradient formation during the carburization process. The second section is focused on studying the effects of key material variables (Co content and WC grain size) on the kinetics of gradient formation during the process. The third section extends the application of the carburization process to the ultrafine grain WC-Co materials containing grain growth inhibitors.

4.1 Effects of Key Process Factors

In Chapter 3, the thermodynamic feasibility of the carburization heat treatment process in making functionally graded WC-Co has been demonstrated. The carburization process depends on the choice of process parameters, such as the carbon potential of the treating atmosphere and the length of treating time. These factors determine the graded structure that can be formed in the final WC-Co products. The effects of these factors will be presented and discussed in this section.

4.1.1 Experimental

WC-Co powder with 10% Co by weight was used as raw materials for this study. WC-10Co specimens with slightly substoichiometric carbon content (5.36 wt%) were prepared. Tungsten powder was added to the WC-Co mixed powder to reduce the total carbon content. The mixture of the powders was ball milled in heptane for four hours in an attritor mill. The milled powder was dried in a Rotovap at 80^{o}C and then cold pressed at 200 MPa into green compacts of 2x0.6x0.7 cm^3 in dimensions. The green compacts were sintered in vacuum at 1400^{o}C for one hour. The cross sections of the as-sintered specimens were polished and etched with Murakami's reagent for 10 seconds to determine if there was any Co_3W_3C (η) phase or free (uncombined) carbon phase in the microstructure. The examinations of the microstructure of the as-sintered WC-10Co samples indicated that there was neither η nor free carbon phase formed during the sintering. Each sintered specimen was cut into two halves before heat treatment. To avoid the influence of the atmosphere during sintering on surface compositions of specimens, only the cross sections were used for analyzing the gradients after heat treatments.

The carburizing heat treatments of sintered samples were conducted in atmospheres consisting of mixtures of methane (CH_4), hydrogen (H_2) at 1300^{o}C. To study the effect of carburizing atmosphere, mixed gases with varied ratios ($P_{CH_4}/P^2_{H_2}$) ranging from 1/150 atm^{-1} to 1/35 atm^{-1} were controlled by using digital mass flow controllers. The effect of time was investigated by holding at 1300^{o}C for 15 minutes to 360 minutes.

Cobalt concentration profiles perpendicular to the surface were measured using the energy dispersive spectroscopy (EDS) technique. Each data point of the cobalt composition reflects an averaged value obtained by scanning a 10x140 μm^2 rectangular

area that was parallel to the surface. The rectangular area for measurement was spaced in 10 μm increment in the direction perpendicular to the surface. In this way, the measurement was performed to the depth of 150 μm from the original surface. The carbon content was excluded from quantitative analysis since EDS is not a suitable technique for measuring carbon content accurately. The standard deviation of the data is approximately ± 0.36% of the average value of 10%, which is obtained by performing 40 repeated measurements on a standard WC-10 wt% Co specimen with uniform microstructure. These measurements were made at different locations on the cross-section of the standard specimen.

4.1.2 Results and Discussions

4.1.2.1 Effect of P_{CH4}/P_{H2}^{2} Pressure Ratio of the Atmosphere

The effect of atmosphere was studied by varying the ratio of partial pressures of methane to hydrogen (P_{CH4}/P^{2}_{H2}). Specific ratios were 1/150, 1/75, 1/50, 1/35 atm^{-1}. The WC-10Co samples were heat treated in those atmospheres for 60 minutes at 1300°C. The examination of the microstructures of the treated composites showed that all samples are free of uncombined carbon phase except the specimen treated under P_{CH4}/P^{2}_{H2} ratio of 1/35 atm^{-1} indicating that this atmosphere condition is excessive.

Figure 4.1 displays the measured Co concentration profiles of the heat treated samples under different atmosphere conditions. When the specimen was heat treated using a relatively low P_{CH4}/P_{H2}^{2} ratio of 1/150 atm^{-1}, the Co content is lowest near the surface and it increases with depth from the surface to the core of the specimen until the cobalt content approaches the nominal value of 10 wt%. When the specimens were heat treated at relatively high P_{CH4}/P_{H2}^{2} ratios of 1/75, 1/50 and 1/35 atm^{-1}, the Co content

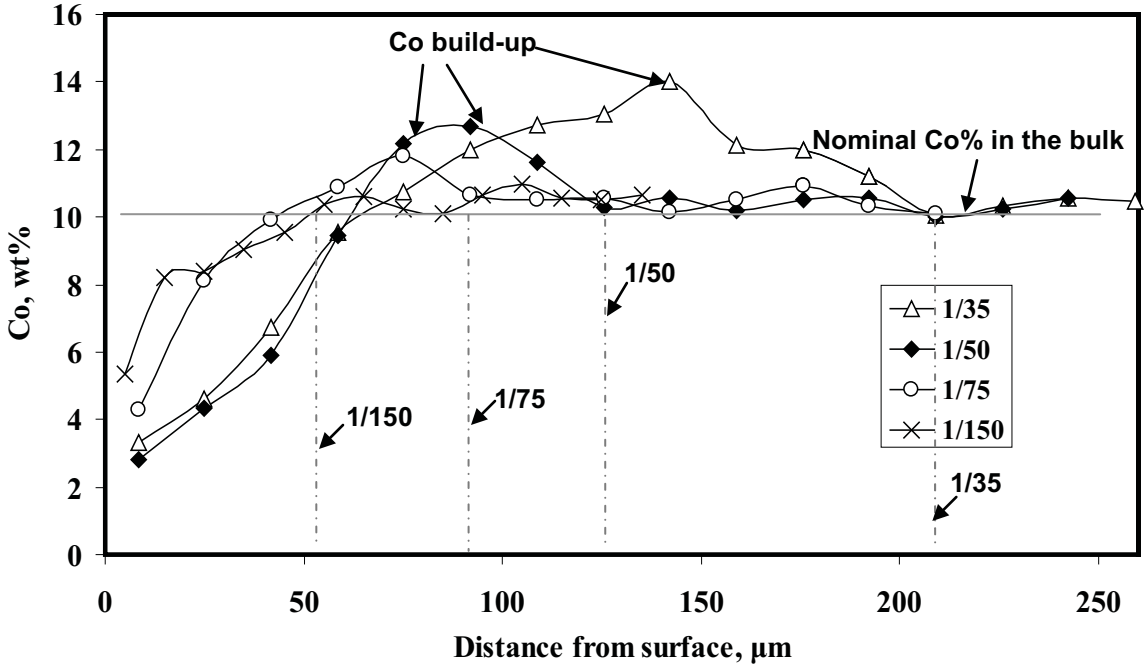

Figure 4.1 Cobalt concentration profiles of the sintered WC-10Co samples after heat treatments in varying atmospheres at 1300°C for 60 minutes. The series of numbers represent the $P_{CH4}/P_{H2}{}^2$ ratio of atmosphere.

profiles increased gradually from the lowest Co content near the surface to a maximum value that is higher than the nominal Co value – a build-up (as indicated in Figure 4.1); it then decreased and leveled off at the nominal Co content.

It is believed that the build-up of Co is a result of the relative kinetic rates of carbon diffusion and liquid migration. Previous studies by the present authors have shown that liquid migration is a rapid process [1]. The rate of carbon diffusion, however, is relatively slow compared to that of liquid migration giving rise to the build-up of liquid Co at the diffusion front. This can be understood by posturing if the diffusion of carbon is rapid, the carbon difference in the material will be quickly homogenized and the redistribution of Co phase would not have occurred. In fact, the phenomenon of Co build-up is one

circumstantial evidence that suggests that the kinetics of the formation of Co gradient is controlled by the slow carbon diffusion process. Recognizing that the carbon diffusion is the rate controlling step is important for modeling the kinetics of the process.

To quantitatively evaluate the effects of the $P_{CH4}/P_{H2}{}^2$ ratio of the atmosphere on the formation of gradient, two measurable parameters - amplitude of cobalt gradient (A_G) and thickness of the gradient zone (X_G) - are extracted from each of the Co concentration profiles in Figure 4.1. The amplitude of Co gradient is defined as the difference between the nominal Co content and the lowest Co content as a fraction of the nominal content of the bulk. The thickness of the Co gradient is defined as a measure to determine the distance from the surface to which the cobalt content is affected by the process. In cases when there is no observable Co build-up, the thickness of the gradients is the distance from the original surface to the position where the Co content reaches its nominal Co concentration as in the bulk of the specimen. While in the cases when there is an observable Co build-up, the thickness is the distance from the surface including both the low Co layer and the Co build-up.

Figure 4.2 plots the results and shows that both the thickness and amplitude of the gradients increase with $P_{CH4}/P_{H2}{}^2$ ratio. The above results can be qualitatively understood based on the decomposition of methane and its effect on the carbon concentration on surface. Methane decomposes according to the following reaction:

$$CH_4 \Leftrightarrow 2H_2 + [C]$$

where [C] expresses the carbon atoms dissolved in the Co phase on the surfaces of samples.

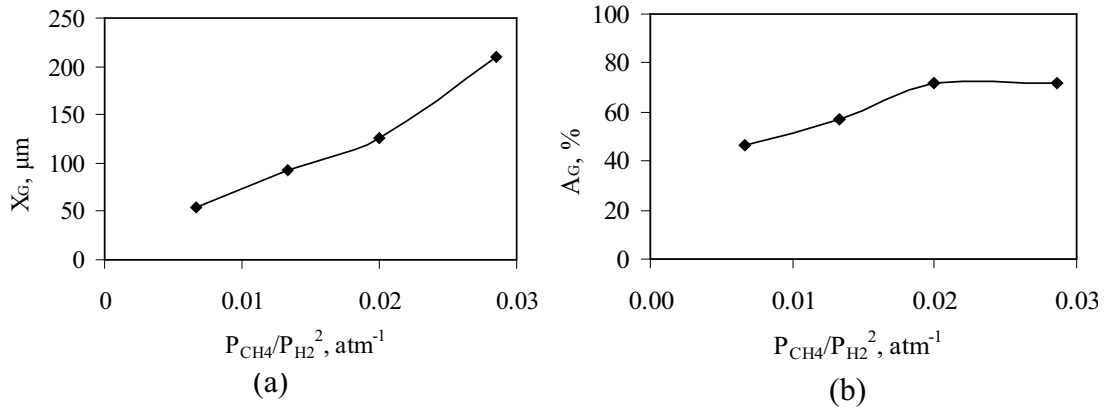

Figure 4.2 The dependences of (a) thickness of gradient zone, X_G and (b) amplitude of Co gradient, A_G as a function of P_{CH4}/P_{H2}^2 ratio of the atmosphere.

Therefore, the carbon potential (C_P) of the treating atmosphere can be calculated by:

$$C_P = K_P \frac{P_{CH_4}}{P^2{}_{H_2}} \tag{4.1}$$

where P_{CH4} is the partial pressure of gas methane (CH_4) and P_{H2} is the partial pressure of gas hydrogen (H_2). K_P is the equilibrium constant of the reaction at a given temperature. According to equation (4.1), the carbon potential of the atmosphere, C_P is proportional to the ratio (P_{CH4}/P_{H2}^2) of the atmosphere provided that the treating temperature is maintained constant. Thus, under the condition of this study, higher P_{CH4}/P_{H2}^2 ratio (representing higher carbon potential) will generate higher surface carbon composition, hence a greater difference of carbon concentration between the surface and the core of the specimen, i.e., a larger driving force for carbon diffusing. Consequently, Co will migrate further into the specimen resulting in greater thickness and amplitude of cobalt gradient. As mentioned earlier, the above qualitative explanation is rather straightforward. To

quantitatively predict the thickness and the amplitude, modeling of the effects of P_{CH4}/P_{H2}^2 ratio of the atmosphere will be needed.

4.1.2.2 Effects of the Length of Time of Heat Treating

Figure 4.3 shows the effect of heat treatment time on the Co gradient. The WC-10Co samples were heat treated in an atmosphere with constant P_{CH4}/P_{H2}^2 of 1/150 atm^{-1} at 1300°C. The holding time at the temperature varied from 15 to 360 minutes. Again, specimens were examined to ensure there is no free carbon phase in the material. Co gradients were observed in each of the treated samples with similar profiles as described in the Section 4.1.2.1. One observable difference among the gradients developed under varying lengths of time is that when the specimens were heat treated for shorter time,

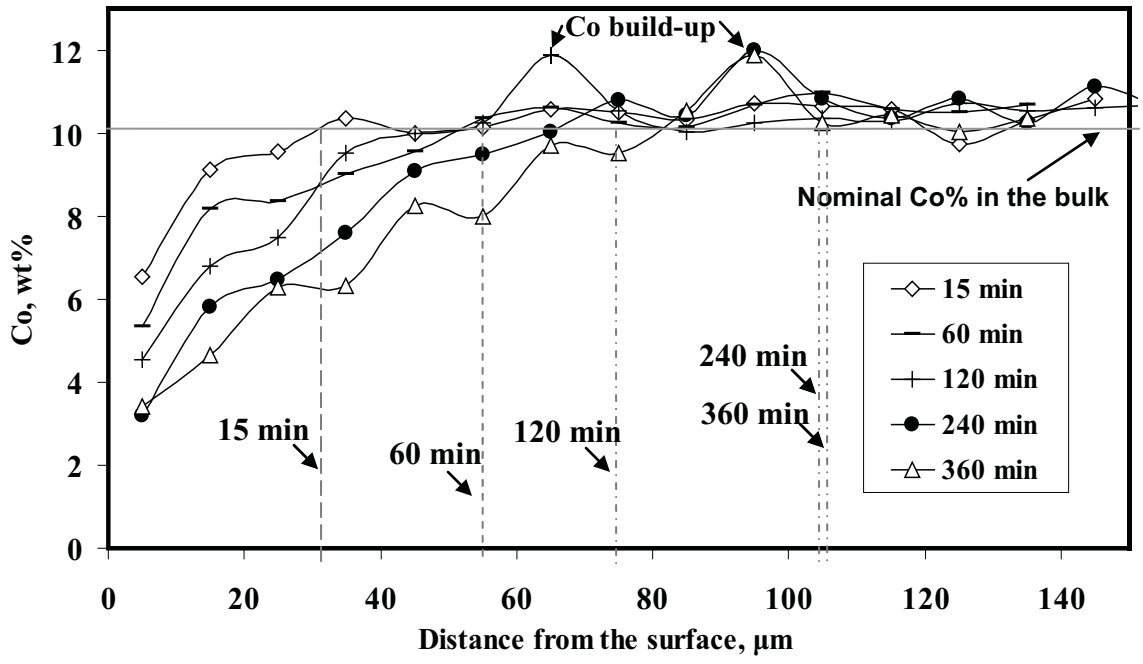

Figure 4.3 Cobalt concentration profiles of the WC-10Co samples which were heat treated at 1300°C in the atmospheres of fixed P_{CH4}/P_{H2}^2 ratio of 1/150 atm^{-1} for various lengths of time.

namely, 15-60 minutes, there was no significant Co build-up. However, when the specimens were heat treated for longer time up to 120-360 minutes, the Co build-up was evident. This phenomenon is again attributed to the relative rates of carbon diffusion versus liquid migration as mentioned earlier.

The effects of time were investigated by measuring the thickness and the amplitude of the gradients after the heat treatments and the results are shown in Figure 4.4. Logically the thickness and the amplitude of the gradients increase with increasing time. The effect of time is attributed to its effect on carbon diffusion. Figure 4.4, however, also shows that there was little change in neither thickness nor amplitude of the Co gradients as the heat treating time was increased from 240 to 360 minutes. This can be understood based on the fact that the diffusion of carbon must go through Co phase. After 240 minutes, the total Co content at the surface is decreased to as low as 3 wt% (Figure 4.4), thus the effective cross-section area of the Co phase which is the only path for carbon diffusion was dramatically reduced. Therefore the kinetics of the overall process will also change dramatically.

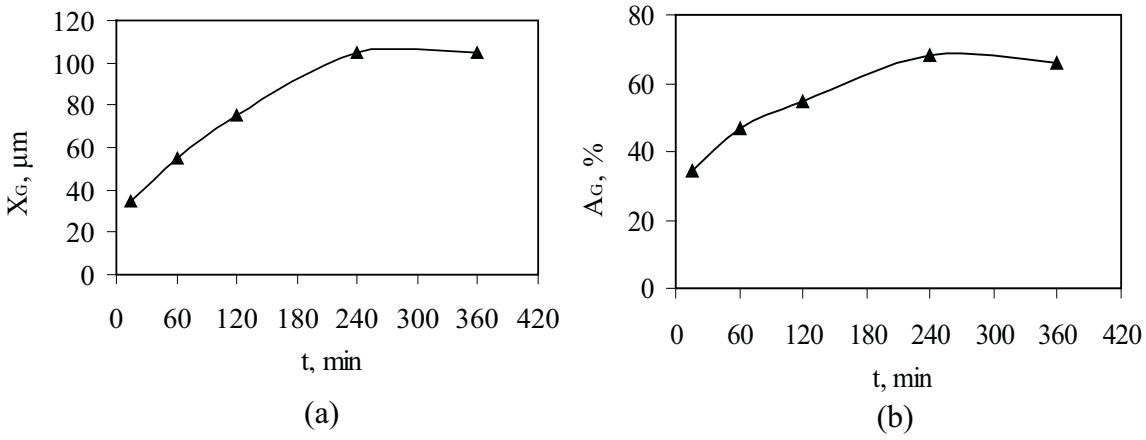

Figure 4.4 The dependences of (a) thickness of gradient zone, X_G and (b) amplitude of Co gradient, A_G as a function of the length of treating time, t.

Figure 4.5 correlates the square of the measured thickness of gradient (X_G^2) with time (t). It shows that X_G^2 increases linearly with t. In other words, the increase of the thickness of Co gradient obeys the parabolic law of diffusion with time; whereas when the time is extended to 360 minutes, the linear relationship is no longer followed. First, the parabolic relation between the gradient thickness and time suggests once again that the process is carbon diffusion controlled. Second, the deviation from the linear relation at longer time suggests that, while the kinetics of gradient formation may be still controlled by the carbon diffusion process, at longer times the diffusivity of carbon as well as the availability of diffusion path have changed substantially resulting in the slowdown of the overall kinetic rate of the process.

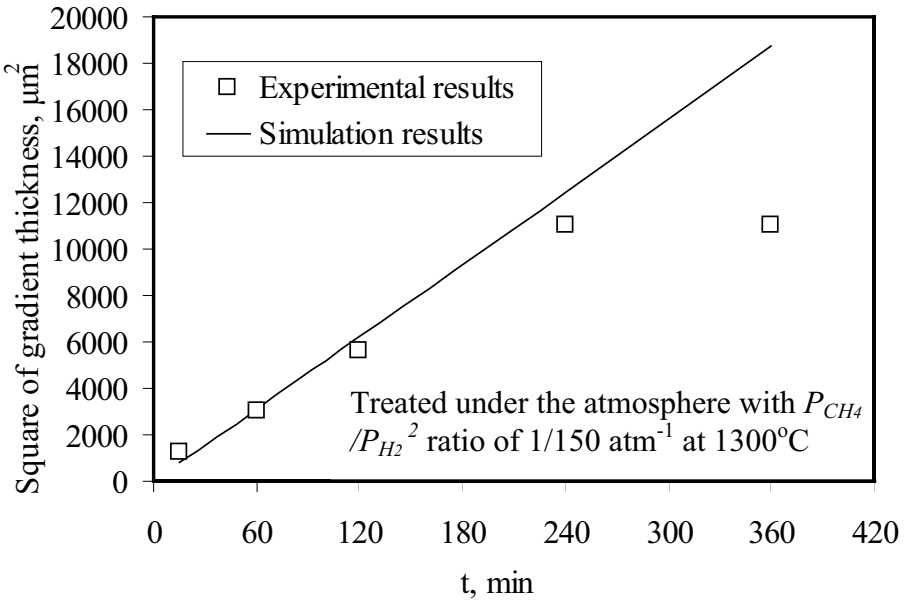

Figure 4.5 Comparison of experimentally measured thicknesses of Co gradient with simulation results.

4.1.3 Conclusions

Continuous Co gradients with different thicknesses and amplitudes were developed under variable atmosphere conditions and lengths of heat treatment time. The experimental findings described in this section clearly showed that the key process parameters including composition of the atmosphere and time have significant effects on the formation of Co gradients. It was shown experimentally that higher carbon potential of atmosphere and longer time of carburizing treatment lead to thicker Co gradients with greater amplitude. The thickness of the gradient followed a parabolic law with time, indicating that the overall kinetics of the process is determined by the diffusion of carbon.

4.2 Effects of Key Material Factors

The material variables, such as Co content and the grain size of WC phase, are also important factors that affecting the gradient formation during the carburizing heat treatment process. For the proposed process to be applicable to a wide range of WC-Co materials, it is equally important to study the effects of the key material factors on the formation of gradients. This section will present and discuss the effects of the material variables.

4.2.1 Experimental

4.2.1.1 Material Preparation

A set of WC-Co powders with different grain sizes and cobalt contents, labeled as $WC_{(f)}$-10Co, $WC_{(m)}$-10Co, $WC_{(c)}$-10Co, $WC_{(c)}$-6Co as well as $WC_{(c)}$-16Co, were prepared in this study. The subscripts (*c*, *m* and *f*) represent the powders with coarse, medium and fine grain size respectively; the number preceding the Co denotes the weight percentage

of Co binder phase. Commercially available WC and Co powders were used as raw materials. Three types of WC powders with different grain sizes were used. The carbon content of all the WC-Co powders is slightly substoichiometric. Tungsten powder was added to reduce the total carbon content below the stoichiometric value. The carbon deficiency was designed to make sure that no η-phase would form in the sintered material. Powder mixtures were ball milled in heptane for 4 hours in an attritor mill. After milling, the powders were dried in a Rotovap at 80^{o}C and then pressed under 200 MPa presses into green compacts with dimensions of $2 \times 0.6 \times 0.7$ cm^3. The green compacts were sintered in vacuum at 1400^{o}C for 1 hour.

Table 4.1 summarizes the WC grain size, Co content, and specific magnetic saturation (SMS) of all the sintered samples. The WC grain size was measured based on the scanning electronic micrographs of the cross-sections of the as-sintered sample by means of the linear incept method. The carbon composition of the as-sintered alloys was determined by the measurements of SMS using the saturation induction measuring system. SMS were commonly measured for measuring the carbon composition of the sintered material during the manufacturing of cemented carbides since SMS

Table 4.1 Microstructures and compositions of as-sintered WC-Co materials

Material	Grain size (μm)	Composition		
		Cobalt content (wt%)	Carbon composition	
			SMS (%)	Comments
$WC_{(f)}$-10Co	0.72	10	84.06	Sub-stoichiometic
$WC_{(m)}$-10Co	1.02	10	84.02	Sub-stoichiometic
$WC_{(c)}$-10Co	1.55	10	84.77	Sub-stoichiometic
$WC_{(c)}$-6Co	1.62	6	84.90	Sub-stoichiometic
$WC_{(c)}$-16Co	1.60	16	84.09	Sub-stoichiometic

increases with the increasing carbon content in the Co phase [2]. The carbon content in Co phase instead of the gross carbon content was used to characterize the carbon compositions of the samples. This is done for the reason that the kinetics of carbon diffusion and liquid migration is dependent on the carbon content in Co phase rather than total carbon content that involves carbon in both Co and WC phase. From Table 4.1, it shows that: (1) the samples $WC_{(f)}$-10Co, $WC_{(m)}$-10Co, $WC_{(c)}$-10Co have different grain sizes but the same Co content and similar carbon composition; (2) the samples $WC_{(c)}$-6Co, $WC_{(c)}$-10Co, $WC_{(c)}$-16Co differ in Co contents but are similar in grain size and carbon composition.

4.2.1.2 Postsintering Carburizing Heat Treatment

The postsintering heat treatments were carried out in a tube furnace with flowing mixture gas of methane and hydrogen. The fully dense WC-Co samples (Table 4.1) were heated to the temperature of 1300^{o}C at a rate of 20^{o}C/min and held at 1300^{o}C for a fixed time (60 minutes), then cooled down to room temperature by turning off the power (cooling rate of 50^{o}C/min above 1200^{o}C). The treating atmospheres were controlled by varying the carbon potentials (expressed by P_{CH4}/P_{H2}^{2}) ranged from 1/150 atm^{-1} to 1/35 atm^{-1} using the digital mass flow meters. The various atmosphere conditions and materials to be heat treated are listed in Tables 4.2 and 4.3.

4.2.1.3 Characterization

After heat treatment, the cross-sections of specimens were polished to measure the Co concentration profiles perpendicular to the surface using the Energy Dispersive Spectroscopy (EDS) technique. Each data point of the cobalt composition is an averaged

Table 4.2 Heat treatment conditions and materials for studying effects of grain size

Samples	Treating temperature (^oC)	$P_{CH_4}/P_{H_2}^2$ ratio of the treating atmosphere (atm^{-1})	Treating time (minutes)
$WC_{(f)}$-10Co, $WC_{(m)}$-10Co, $WC_{(c)}$-10Co	1300	1/35	60
		1/50	
		1/75	
		1/150	

Table 4.3 Heat treatment conditions and materials for studying effects of Co content

Samples	Treating temperature (^oC)	$P_{CH_4}/P_{H_2}^2$ ratio of the treating atmosphere (atm^{-1})	Treating time (minutes)
$WC_{(c)}$-6Co, $WC_{(c)}$-10Co, $WC_{(c)}$-16Co	1300	1/40	60
		1/75	
		1/150	

value obtained by scanning a 10x140 μm^2 rectangular area that was parallel to the surface. The rectangular area for measurement was spaced in 10 μm increments in the direction perpendicular to the surface. In this way, the measurements were performed to the depth of 300 μm from the original surface. The carbon content was excluded in the quantitative analysis considering that EDS is not suitable for measuring carbon quantitatively. The standard deviation of the data is approximately $\pm$ 0.36%, which is obtained by performing 40 repeated measurements on a standard WC-10wt%Co specimen with uniform microstructure. The 40 measurements were conducted by scanning identical size of areas (10 μm by 140 μm) at different locations on the cross-section of the standard specimen.

4.2.2 Results and Discussions

In this section, experimental results are presented to show the effects of Co content and WC grain size on the kinetics of the process of forming the Co graded structure. Noting that the experimental design of this study is based on the one-factor-at-a-time method and there is only a single factor varying while the others are kept constant. For example, for study the grain size effects, the samples used in comparison only have difference in grain size and they were treated in the same furnace run in order to assure identical treatment condition.

4.2.2.1 Effects of Grain Size and Atmosphere

The effect of grain size was studied by preparing specimens $WC_{(f)}$-10Co, $WC_{(m)}$-10Co and $WC_{(c)}$-10Co with different grain sizes (0.72, 1.02 and 1.55 μm) but the same carbon and Co compositions (Table 4.1). To examine whether the influences of grain size are consistent under different heat treatment conditions, atmospheres with varying ratios of partial pressures of methane to hydrogen (P_{CH4}/P_{H2}^2) were used to treat those specimens at 1300°C for 60 minutes (listed in Table 4.2).

Figure 4.6 shows the measured Co concentration profiles of all the treated specimens under different atmospheric conditions. As seen from the Co concentration profiles (Figure 4.6), continuous Co gradients were developed in each of the specimens exhibiting a similar trend: the Co content increased gradually from the lowest Co content near the surface to a maximum value that was higher than the nominal Co content in the bulk – a build-up; it then decreased and leveled at the nominal value. Moreover, it was found that this Co build-up was less significant in the samples treated under the atmosphere of relatively low P_{CH4}/P_{H2}^2 ratio compared to those treated at relatively high P_{CH4}/P_{H2}^2

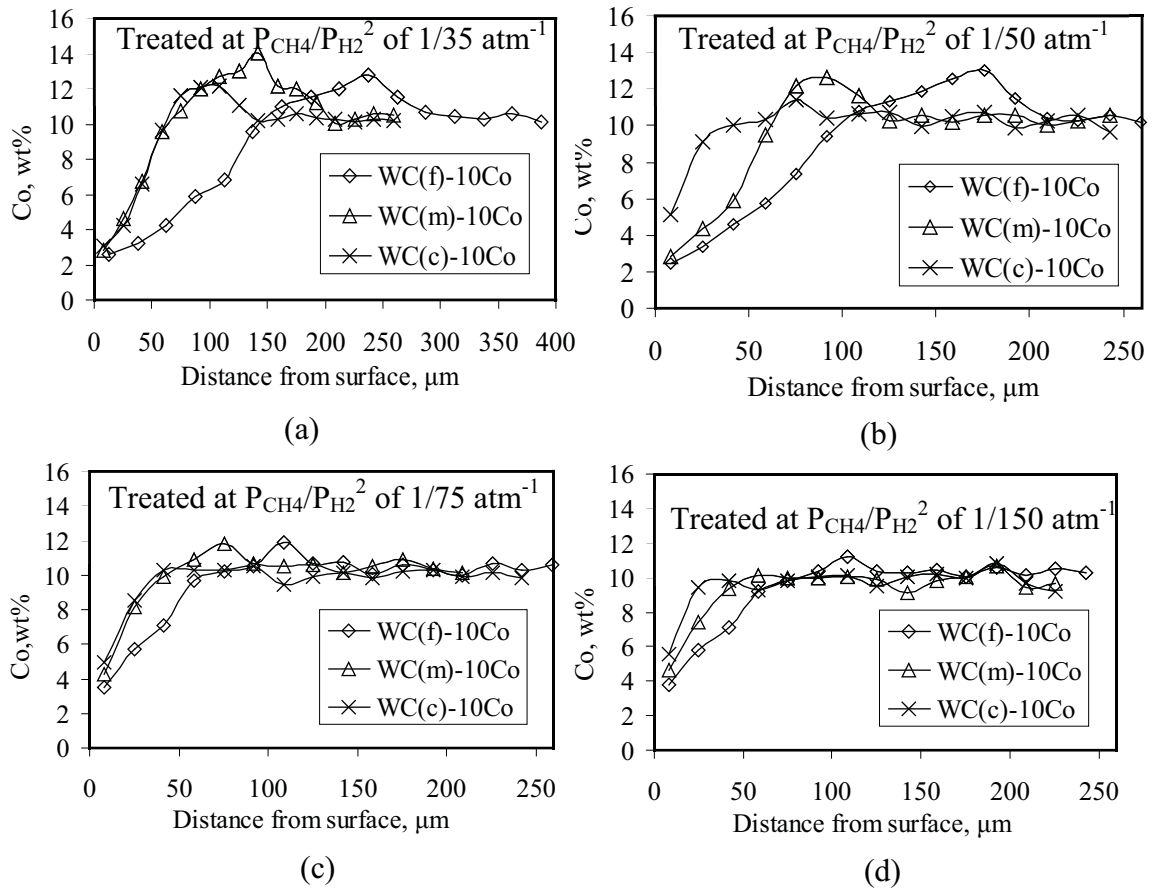

Figure 4.6 Cobalt concentration profiles of the $WC_{(f)}$-10Co, $WC_{(m)}$-10Co, $WC_{(c)}$-10Co samples with varying grain sizes. The specimens were heat treated at 1300°C for 60 minutes in the atmospheres with P_{CH4}/P_{H2}^2 ratios of (a) 1/35; (b) 1/50; (c) 1/75 and (d) 1/150 atm^{-1}.

ratio. Earlier studies [3] as described in Section 4.1 have contributed the build-up of cobalt to the relative rates of carbon diffusion versus liquid migration: relatively slow diffusion and rapid migration result in the pile up of the liquid phase.

To quantitatively evaluate the effects of grain size on the formation of gradient, two measurable parameters - the amplitude of Co gradient (A_G) and the thickness of the gradient zone (X_G) - are extracted from each of the Co concentration profiles in Figure 4.6. The amplitude of Co gradient is defined as the difference between the nominal Co

content and the lowest Co content as a fraction of the nominal content of the bulk. The thickness of the Co gradient is defined as a measure to determine the distance from surface to which the cobalt content is affected by the process. In case when there is no observable Co build-up, the thickness of the gradient is the distance from the original surface to the position where the Co content reaches its nominal Co content as in the bulk of the specimen. While in the case when there is an observable Co build-up, the thickness of the gradient is the distance from the surface including both the low Co layer and the Co build-up.

Figure 4.7 plots the measured results and showed that, for a given atmosphere, the sample with finer grain size develops a gradient of deeper depth and larger amplitude than the sample with coarser grain size. The same tendency was observed in all the atmosphere conditions applied in this study. Moreover, it was observed that for the same material, both the thickness and amplitude of the gradient increase with the P_{CH4}/P_{H2}^2 ratio of the atmosphere, which agrees with our previous results.

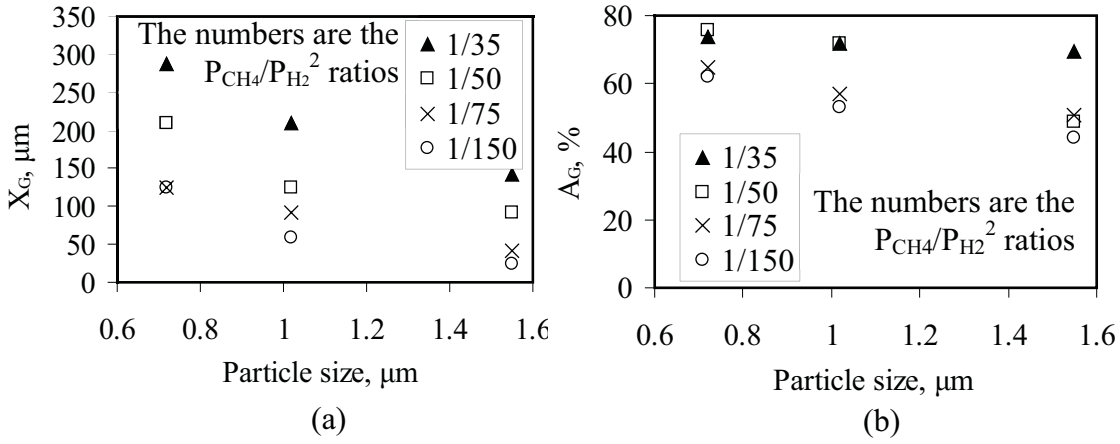

Figure 4.7 The dependences of (a) thickness of gradient zone, X_G and (b) amplitude of Co gradient, A_G as function of grain size and atmosphere.

4.2.2.2 Effects of Co Content and Atmosphere

Figure 4.8 shows the effects of Co content on the gradient formation. The $WC_{(c)}$-6Co, $WC_{(c)}$-10Co and $WC_{(c)}$-16Co samples containing different initial nominal Co contents (6, 10 and 16% in weight percent) but similar in grain size and carbon composition (Table 4.1) were used. Again, to examine the consistency of the effects of Co content under different atmosphere conditions, it applied different atmospheres with P_{CH4}/P_{H2}^2 ratios of 1/40, 1/75, and 1/150 atm^{-1} for treating these samples at 1300°C for 60 minutes (Table 4.3).

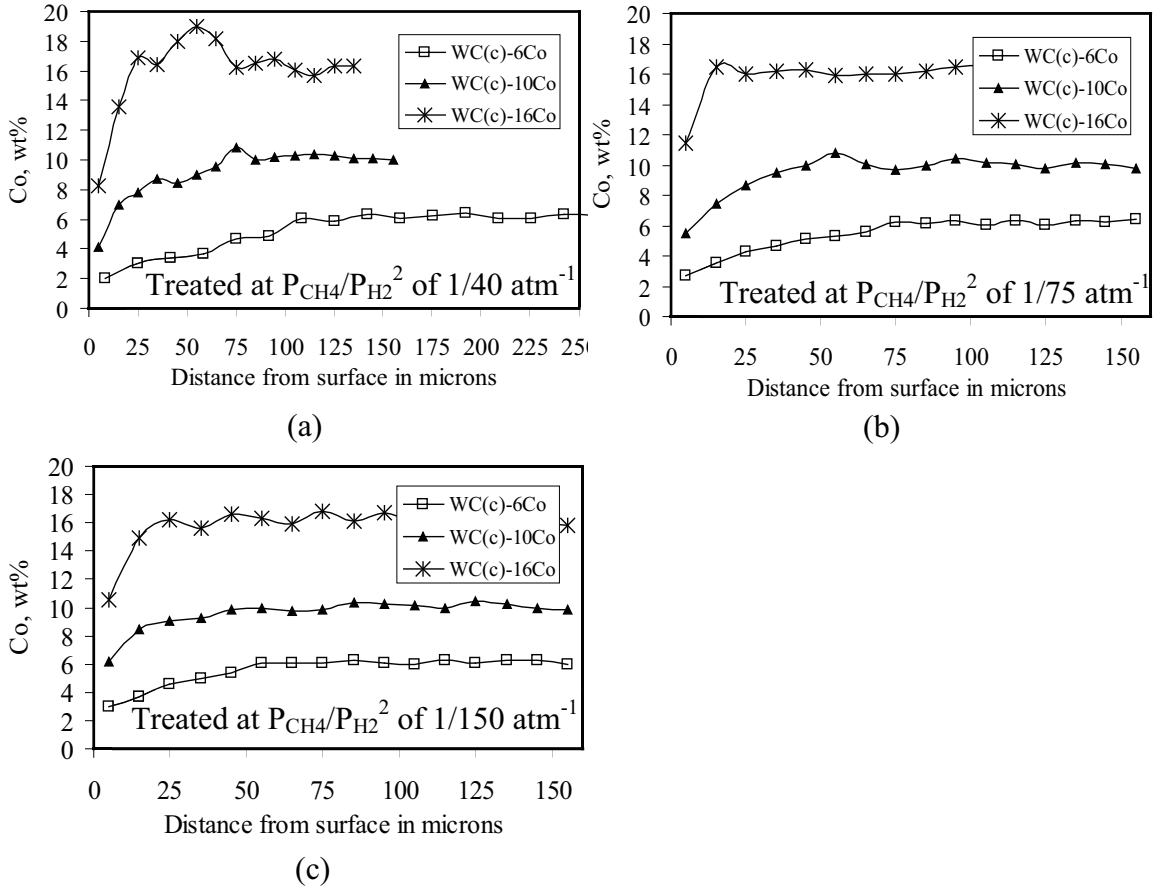

Figure 4.8 Cobalt concentration profiles of the $WC_{(c)}$-6Co, $WC_{(c)}$-10Co, $WC_{(c)}$-16Co samples of varying Co contents. The specimens were heat treated at 1300°C for 60 minutes in the atmospheres with P_{CH4}/P_{H2}^2 ratios of (a) 1/40; (b) 1/75 and (c) 1/150 atm^{-1}.

Co gradients were observed in each of the treated samples with similar profiles as described in Section 4.2.2.1. Similarly, when the specimens were treated using the relatively low P_{CH4}/P_{H2}^2 ratio, there was no evident Co build-up. However, when the specimens were heat treated under the atmosphere of relatively high P_{CH4}/P_{H2}^2 ratio, Co build-up was significant. The phenomenon of the Co built-up can be explained by the same reason that has already been mentioned (Section 4.2.2.1). Quantitatively, the effect of Co content was investigated by measuring the thickness and the amplitude of the gradient formed during the carburization and the results were graphed in Figure 4.9. It reveals that when the materials were treated under the same condition, the material with lower Co content tends to form a gradient of larger amplitude and wider thickness compared to that with higher Co content. It shows the same behavior when the samples were treated by the other atmospheres. Furthermore, it was observed that, for a particular sample, the thickness and amplitude of the gradients increase with the increasing P_{CH4}/P_{H2}^2 ratio of the atmosphere, which matches the findings reported in Section 4.2.2.1.

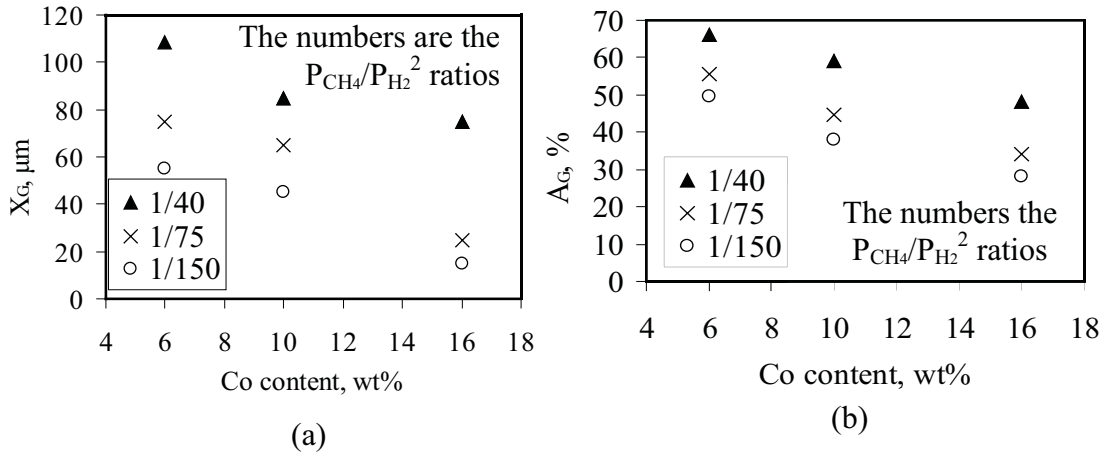

Figure 4.9 The dependences of (a) thickness of gradient zone, X_G and (b) amplitude of Co gradient, A_G as function of Co content and atmosphere.

The experimental results obtained in this study and previously reported findings demonstrated that the process parameters (atmosphere) and material variables (WC grain size and Co content) have significant influences on the formation of the Co gradients. It has been illustrated in Section 4.1 [3] that the gas atmosphere affects the surface carbon composition. A higher P_{CH4}/P_{H2}^2 ratio of the atmosphere will lead to higher surface carbon composition, hence a greater difference of carbon concentration between the surface and the core of the specimen, i.e., a larger driving force for carbon diffusing. Due to that, Co will migrate further into the specimen resulting in greater thickness and amplitude of Co gradient. Since the formation of the gradients has been shown to be controlled by the carbon diffusion process, it is reasonable to believe that the influences of grain size and Co content are related to their effects on the diffusion coefficient of carbon in the material, which will be further discussed.

4.2.3 Conclusions

A wide range of WC-Co samples with varying Co contents or grain sizes were liquid phase sintered to full densification and subsequently carburizing heat treated. Continuous Co gradients with different thicknesses and amplitudes were developed in these materials. It was demonstrated experimentally that the key material parameters including Co content and grain size have significant influences on the formation of Co gradients. In general, for a given atmosphere condition and heat treating time, thicker Co gradients with greater amplitude tend to form in the WC-Co composite with lower Co content and finer grain size.

4.3 Effects of Grain Growth Inhibitor

As mentioned in the introduction of this dissertation (Section 2.1.4), it has become a trend to add grain growth inhibitors, such as VC, Cr_3C_2 to prevent grain growth of WC grains for developing ultrafine grain WC-Co. Such additives, however, increase the hardness at the expense of the fracture toughness of the material [4-6]. Developments in functionally graded WC-Co provide a potential solution to this problem by combining the functionally graded structure and the ultrafine grain structure in WC-Co materials to obtain desirable combinations of mechanical properties.

To obtain the graded structure, a possible way is through the postsintering carburizing-heat-treatment process. Despite the postsintering carburization heat treatment process has been demonstrated effective in producing Co compositional gradient for the straight WC-Co without other additions [3, 7-11], it may not be directly applied to create such gradient in fine grain WC-Co containing grain growth inhibitors. The reason is that the addition of the grain growth inhibitors change the thermodynamics of the WC-Co system [12]. The primary purpose of this study is to extend the utility of carburization heat treatment process to the ultrafine WC-Co materials doped with grain growth inhibitors.

In this section, fully dense Cr_3C_2 doped WC-Co materials were prepared via the traditional liquid phase sintering process. The specimens were then heat treated via a separate process after sintering. Experiments and thermodynamic analysis were carried out to validate the feasibility of the carburizing heat treatment process in creating gradients in the W-C-Co-Cr system. The mechanism of Co gradient formation in this system was also discussed.

4.3.1 Experimental

Cr_3C_2-doped WC-Co specimens (labeled as 10Co-0.3Cr_3C_2) as well as straight WC-Co specimens (refers to 10Co) were used in this study. Commercially available WC and Co powders with 10 wt% Co were the raw material for 10Co, while 0.3 wt% Cr_3C_2 powder was added to the WC-Co mixed powder to prepare 10Co-0.3Cr_3C_2. The powder mixtures were ball milled in heptane for four hours in an attritor mill. After milling, the powders were dried in a rotary vapor at 80^{o}C and then cold-pressed at 200 MPa into green compacts of $2 \times 0.6 \times 0.7$ cm^3 in dimension. Subsequently, the green compacts were vacuum sintered to full densification at 1400^{o}C for 1 hour.

After sintering, differential scanning calorimetry (DSC) analysis for 10Co and 10Co-0.3Cr_3C_2 specimens was carried out in Q600 SDT (TA Instrument). The samples were placed in an alumina crucible with lid. The system was evacuated initially and purged with ultra high purity argon gas. The samples were heated to 1450^{o}C at a heating rate of 20^{o}C/min.

The post-sintering carburizing heat treatments for the fully dense 10Co-0.3Cr_3C_2 specimens were carried out in a tube furnace with a fixed flowing gas mixture of hydrogen (H_2) and methane (CH_4). The heat treatments were conducted at three different temperatures: 1300, 1260 and 1200^{o}C. After heat treatment, cross-sections of both the as-sintered and as-treated 10Co-0.3Cr_3C_2 specimens were polished and characterized using optical microscope and scanning electron microscopy (SEM).

To determine the compositional gradient, cobalt and chromium concentration profiles perpendicular to the surface was measured using the energy dispersive spectroscopy (EDS) technique. Each data point of the cobalt or chromium content was an average

value obtained by scanning a 10x140 μm^2 rectangular area that was parallel to the surface. The rectangular area for measurement was spaced in 10 μm increments in the direction of the depth from the surface. The measurements were performed to the depth of 200 μm from the surface. WC grain size was also measured based on SEM images of the microstructures using linear intercept method. The measurement error is approximately 7%.

4.3.2 Results

4.3.2.1 DSC Analysis

It is well known that the addition of grain growth inhibitor, such as Cr_3C_2, lowers the melting temperature of W-C-Co system [12]. As mentioned earlier in the introduction (Section 2.1.4), the carburizing heat treatment process is required to be between the eutectic and peritectic temperatures of the Co binder phase. However, the data on the melting temperature of the 10Co-0.3Cr_3C_2 sample used in this study are absent. In order to choose a suitable temperature for carburizing the 10Co-0.3Cr_3C_2 sample, we conducted a DSC analysis for measuring the melting temperatures.

The DSC plots of 10Co and 10Co-0.3Cr_3C_2 specimens were presented in Figure 4.10. It showed that the 10Co-0.3Cr_3C_2 sample starts to melt at the temperature of 1233^oC (denoted as T_S in Figure 4.10a) which is about 40^oC lower than that of the 10Co sample (Figure 4.10b). According to phase diagram of Figure 3.1, the melting temperature range for the 10Co sample is between 1275 to 1325^oC. Therefore, the melting range for 10Co-0.3Cr_3C_2 accordingly shifts to the range of 1235 to 1285^oC. The temperature of 1260^oC was then selected to treat the 10Co-0.3Cr_3C_2 sample.

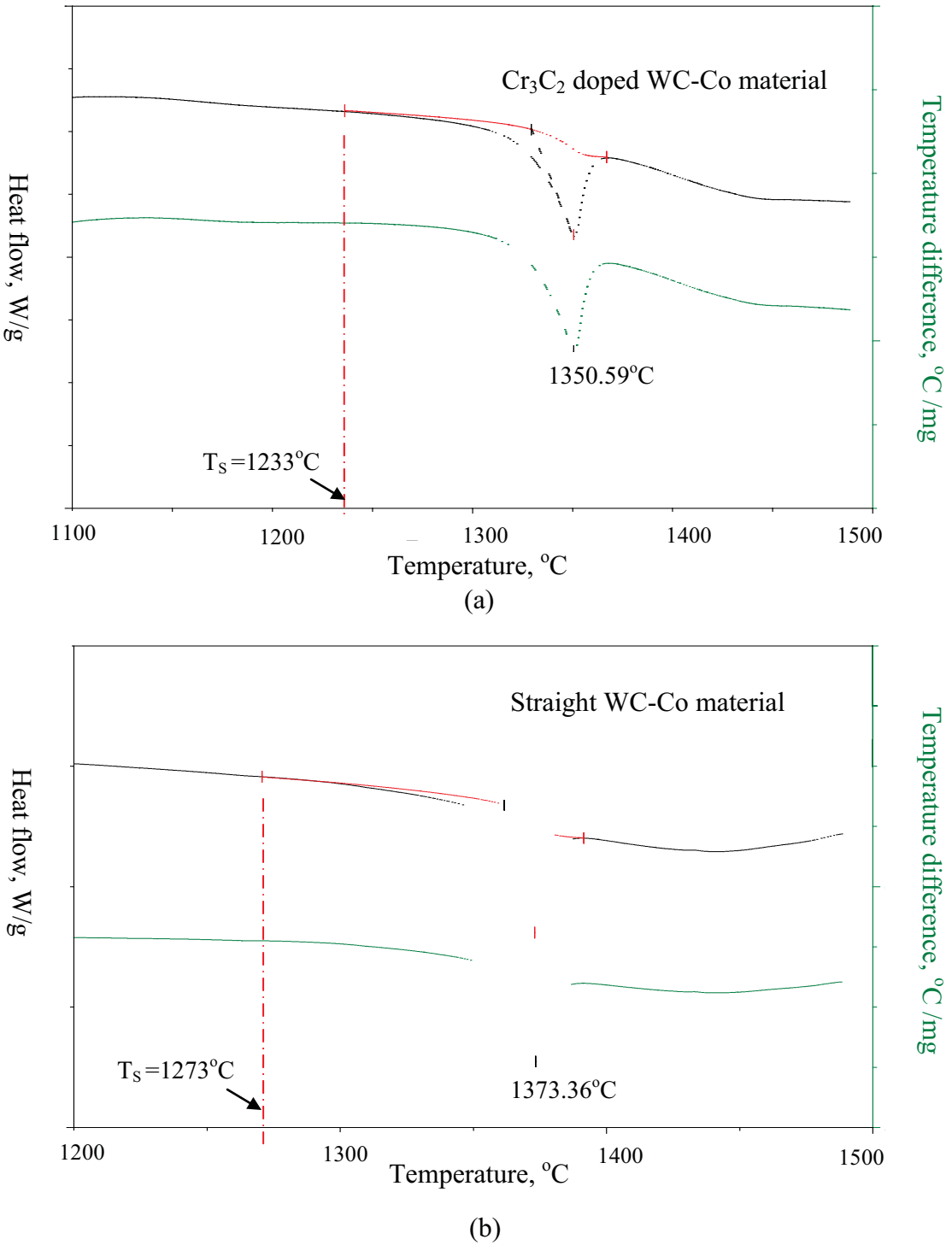

Figure 4.10 DSC analysis of (a) 10Co-0.3Cr_3C_2 and (b) 10Co samples before heat treatment.

4.3.2.2 Microstructures

The 10Co-0.3Cr_3C_2 samples were carburized at three different temperatures of 1200, 1260 and 1300^oC. The results of DSC analysis indicate that 1260^oC is within the melting temperature range of Co binder phase. For comparison purpose, the temperatures (1300^oC and 1200^oC) falling outside of that range were also used to treat the samples. The ratio of the partial pressures of gases in the atmosphere as measured by P_{CH4}/P_{H2}^2 was constant at 1/150 atm^{-1} and the heat treatments were held at each treating temperature for 60 minutes.

Figures 4.11 and 4.12 showed the microstructures of the 10Co-0.3Cr_3C_2 samples before and after heat treatment, respectively. In the SEM images, WC appears as gray particles surrounded by dark Co matrix phase. Before heat treatment, the amount of Co phase was equal between the near surface region and the core region indicating an initial uniform distribution of Co content (Figure 4.11). In contrast, after treatment at 1260^oC, it

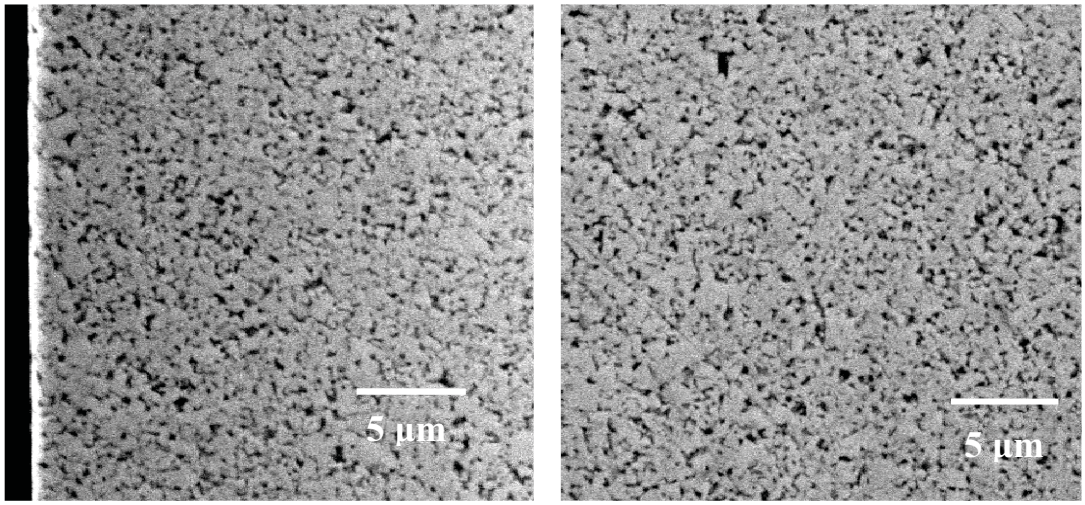

(a) (b)

Figure 4.11 SEM images of (a) the surface region and (b) the core region of 10Co-0.3Cr_3C_2 sample before heat treatment.

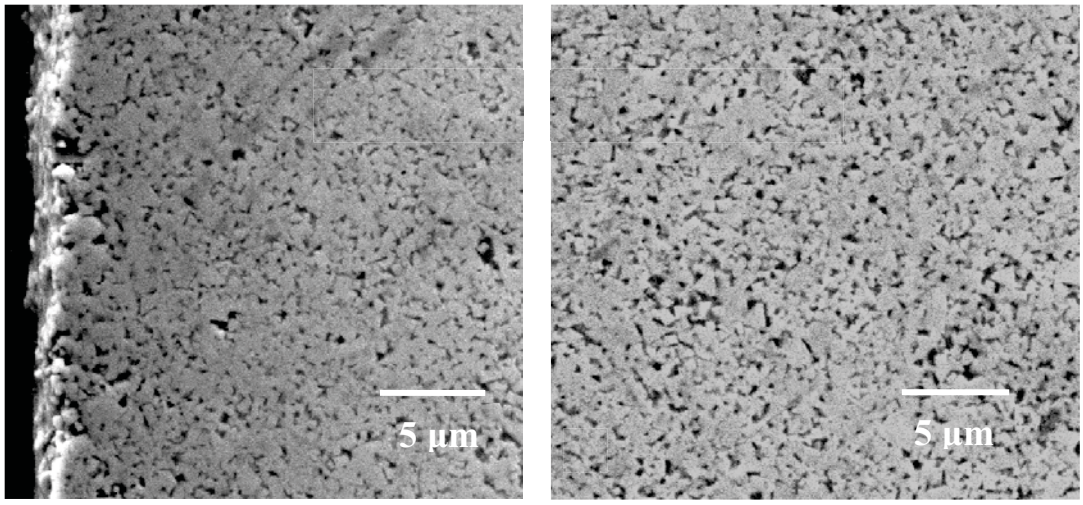

(a) (b)

Figure 4.12 SEM images of (a) the surface region and (b) the core region of the 10Co-0.3Cr_3C_2 sample after heat treatment in the atmosphere of P_{CH4}/P_{H2}^2 ratio of 1/100 atm^{-1} at 1260°C for 1 hour.

was seen less Co phase near surface than in the core of the material suggesting that a cobalt gradient was developed as a result of the heat treatment (Figure 4.12).

When the 10Co-0.3Cr_3C_2 specimen was heat treated at the temperature of 1300°C that is much higher than the melting temperature range, it was observed a significant amount of free graphite phase in the surface region while no obvious gradient of Co was found. Furthermore, as the same sample treated at 1200°C lower than the melting temperature range, the microstructure showed little change from its initial condition and there was neither Co gradient nor free graphite phase that could be found.

4.3.2.3 Co Profiles

Figure 4.13 shows the Co concentration profiles of the 10Co-0.3Cr_3C_2 specimens before and after treatments. The results of the Co concentration profiles agree well with

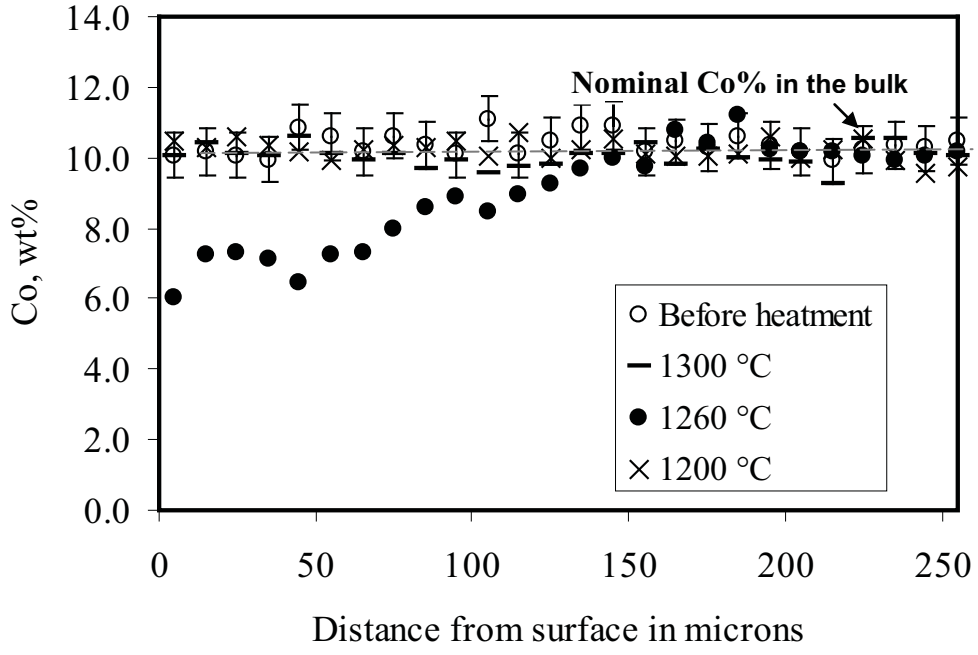

Figure 4.13 Cobalt concentration profiles of sintered 10Co-0.3Cr_3C_2 samples before and after heat treatments at temperatures of 1300, 1260 and 1200°C in the atmosphere with P_{CH4}/P_{H2}^2 ratio of 1/100 atm^{-1} for 1 hour.

the microstructure as described above. For the 10Co-0.3Cr_3C_2 sample treated at 1260°C, there is a continuous gradient developed in the surface region while the Co profile without treatment is flat. It was shown that the Co closest to the surface is as low as 6wt% and then the content of Co increases gradually from the surface into the interior until the Co content reaches the nominal value (10.0 wt%) in the bulk. However, this trend of Co gradient was not found in the specimens treated at 1200 and 1300°C and their Co profiles showed little change from their initial state. The experimental results as presented so far proved that the carburizing treatment is viable in developing gradients within the Cr_3C_2 doped WC-Co material.

4.3.2.4 Measurements of Cr contents and grain sizes

During measuring the Co concentration profiles, it was also observed that the distribution of Cr dissolved in Co phase after the heat treatment was different from its initial state. The composition of Cr in Co phase before heat treatment was generally homogeneous at 3.0 wt% (Figure 4.14). The standard deviation of the data is approximately to be $\pm$ 0.65 wt% of the average value of 3.0 wt%. However, after the carburizing treatment, the composition of Cr is statically higher near surface than in the bulk.

The results of the mean grain sizes at the surface and in the interior of the 10Co-0.3Cr_3C_2 samples were summarized in Table 4.4. It revealed that without heat treatment the average grain sizes near surface and in the interior of the sample are almost equal at

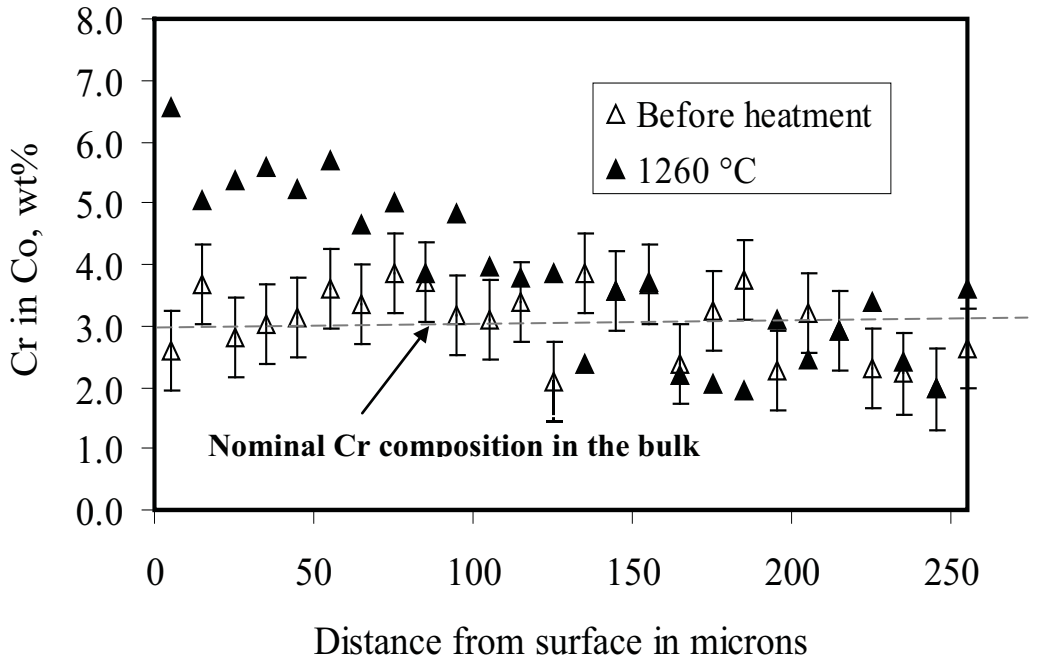

Figure 4.14 Chromium concentration profiles of sintered 10Co-0.3Cr_3C_2 samples before and after heat treatment in the atmosphere of P_{CH4}/P_{H2}^2 ratio of 1/100 atm^{-1} at 1260°C for 1 hour.

Table 4.4 Results of measured grain sizes of the 10Co-0.3Cr_3C_2 specimen before and after heat treatment at 1260°C.

10Co-0.3Cr_3C_2		Grain sizes (μm)
Before treatment	Surface	0.37 ± 0.03
	Interior	0.35 ± 0.03
After treatment	Surface	0.41 ± 0.03
	Interior	0.44 ± 0.04

0.36 μm. After the treatment, the WC grains in the surface and core region of the material respectively are grown to 0.41 and 0.44 μm. The grain growth after the heat treatment was attributed to the Ostwald ripening of WC phase as a result of the heat treatment. Further, it showed that there is almost no difference in the grain growth rate between the surface and the core of sample during the heat treatment.

4.3.3 Discussions

4.3.3.1 Thermodynamic Analysis of W-C-Co-Cr System

The thermodynamic analysis of phase equilibria of W-C-Co-Cr system [12] leads us to expect that a similar Co graded structure can be created in the Cr_3C_2 added WC-Co material using the existing carburization process for straight WC-Co material. Figure 4.16 shows a phase diagram of W-C-Co-Cr with constant compositions of 1.44 % Cr and 16 % Co in atomic weight. Compared to the phase diagram of W-C-Co system (Figure 3.1), the phase relations of WC-Co undergo certain changes upon the adoption of Cr_3C_2. Firstly, the melting point of Co binder phase shifts to lower temperature. Secondly, the straight lines (namely the peritectic and eutectic temperatures as denoted in Figure 3.1) have been changed to two four-phase-regions, namely WC-Co(s)-Co(l)-η and WC-Co(s)-

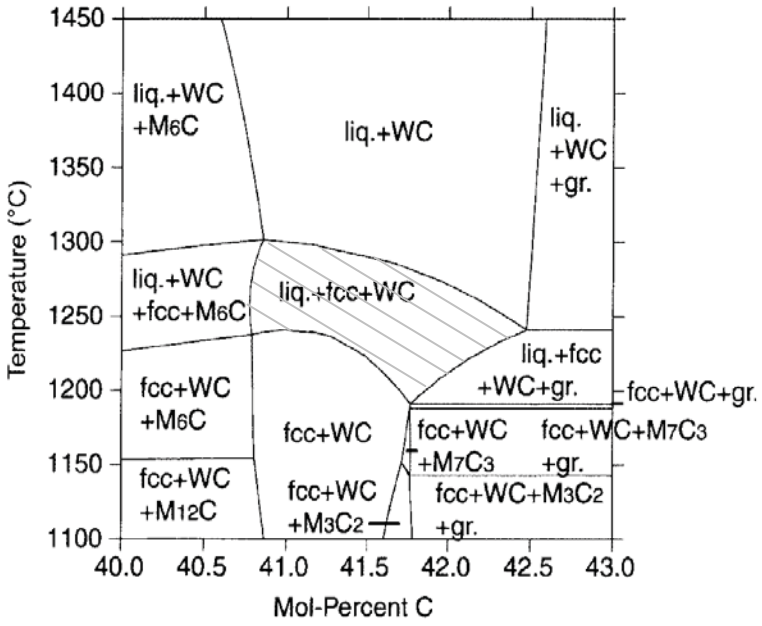

Figure 4.15 Vertical section of the ternary phase diagram of W-C-Co-Cr system with 1.44% Cr and 16% Co (atomic percent), adapted from [12].

Co(l)-graphite regions. Except for those changes, similar to the W-C-Co system, the W-C-Co-Cr system has a WC(s)-Co(s)-Co(l)-coexisting equilibrium region at the temperature range of 1180 to 1300^{o}C as indicated by the shaded area (Figure 4.16). It implied that the Cr_3C_2 doped WC-Co material has met the prerequisite for forming the graded structure.

4.3.3.2 Mechanism of Gradient Formation

The feasibility of the carburization approach in forming Co gradient in the system of W-C-Co-Cr was not only verified thermodynamically but also experimentally. It is to believe that the formation of Co gradient is related to the migration of liquid phase. Studies have documented [1] that the direction of the liquid migration depends on three main factors including the gradient in the volume fraction of liquid Co phase, WC grain

size gradient, and carbon content gradient. In general, liquid phase migrates from the regions with higher volume fraction of liquid Co phase to the regions with lower fraction of liquid Co phase, from the regions with coarser grain size to the regions with finer grain size, and from the regions with higher carbon content to the regions with lower carbon content. Next, we examined the contributions of each of the three key factors in inducing the liquid migration and forming the Co gradient. Firstly, with respect to the factor of grain size, experimental results have shown that the grain size near surface is a little smaller than and that in the core of material. In this case, the grain size gradient is supposed to hinder the liquid migration from the surface to the interior.

Secondly, regarding the factor of carbon content, the Co gradient observed in this study might be induced by the difference in the carbon content as it will drive the liquid Co flowing from the surface with higher carbon content to the core with lower carbon content. However, as has been mentioned in Section 3.2.3, the effect of carbon on the redistribution of the Co phase is limited. Work by the present author [1] has reported that the differences in cobalt content induced solely by the difference in carbon content ranging from the stoichiometric carbon content to a super-stoichiometric carbon content (at the left boundary of the WC(s)-Co(l)-Graphite(s) field (Figure 3.1)) was less than 1.0 wt% Co. The actual Co gradient formed in this study is about 4.0 wt%. Therefore, the carbon content gradient is either not a primary factor that creates the Co compositional gradient.

Lastly, in terms of the factor of the liquid volume fraction, it is very likely to be the dominant factor. It has mentioned in Section 4.3.3.1 that the W-C-Co-Cr system possess a WC(s)-Co(l)-Co(s)-coexisting range in which the volume fraction of liquid Co phase

has a strong dependency on the carbon content. This provides a probability to bring about a difference in the liquid volume fraction through creating a carbon content gradient. Upon the above discussions, we considered that the graded volume fraction of liquid phase is the dominant factor inducing the liquid migration and therefore the Co gradient. The mechanism proposed for explaining the gradient formation in the inhibitor added ultrafine WC-Co materials will be the same as that for the straight WC-Co materials, which has been described elsewhere in Section 3.2.3.

Moreover, a continuous gradient of Cr in Co phase was observed in Figure 4.14. Cr has a high solubility in both solid and liquid Co phase and thus in the case of this study Cr would dissolve completely in the Co binder phase at the treating temperature. Intuitively, Cr will transport inwardly with the inward migration of liquid Co phase. However, the concentration of Cr was observed to be higher near surface than the interior. This indicates that Cr diffuses outwards from the interior to the surface rather than flowing with the inward liquid migration. This can be understood by hypothesizing that it exists a thermodynamic coupling between the inward carbon diffusion and the outward Cr diffusion. The inward diffusion of carbon from the atmosphere into the material causes Cr to diffuse in the opposite direction from the carbon poor core region outwards to the carbon rich surface region. As a consequence, a Cr gradient with higher concentration near surface than in the interior develops. In fact, a similar phenomenon was observed during the sintering of cemented WC-Co containing (Ti,W)(C,N) under the denitriding atmosphere [13, 14]. It was reported that Ti was depleted in the surface region as a result of the surface denitriding treatment. This phenomenon was interpreted in many articles that it is the strong coupling of Ti and N causing the inward diffusion of Ti driven

by the outward diffusion of N, therefore the surface zone was observed to be depleted of Ti. However, it is worth noting that further evidence is needed to verify the coupling relations between C and Cr so as to explain the formation of Cr gradient in the present study.

4.3.3.3 Applications of the Surface Treatment Process

In this study, the successful application of the carburizing treatment process in the Cr_3C_2 added WC-Co materials provides a good example that the concept of surface atmosphere heat treatment process could be utilized to fabricate functionally graded materials (FGM) in many other material systems. It will be valuable to utilize this surface treatment process for manufacturing FGM because it is extremely cost effective. Hence, we summarized a series of steps to design the surface treatment process available for making FGM. The first step is to confirm whether the material in thermodynamics has satisfied the prerequisite for using the surface treatment technique, specifically, whether the material possesses the phase equilibria between solid and liquid phase. The second step is to choose an element that can control the phase conversion between the solid and liquid phase, for example carbon can do that for the Co phase in WC-Co material. The third step is to determine the liquid-solid-coexisting temperature range for the specific material system either by looking up the phase diagram or via directly measuring the melting temperatures using differential thermal analysis. Finally, a suitable heat treatment media (either gaseous, liquid or solid), which can supply the selected element for the heat treatment process is chosen.

4.3.4 Conclusions

This research has shown that via conducting a postsintering carburization heat treatment, a Co gradient can be created within the Cr_3C_2 added WC-Co material. The temperature for the carburizing heat treatment must be within the solid-Co-liquid-Co coexisting phase field. The formation of the Co gradient in W-C-Co-Cr system can be attributed to the same mechanism proposed for the W-C-Co system.

4.4 References

[1] Fan P, Guo J, Fang ZZ, Prichard P. Metall Mater Trans A 2009;40:1995.

[2] Fang Z, Eason JW. Int J Powder Metall 1993;29:259.

[3] Guo J, Fang ZZ, Fan P, Wang X. Submitted to Acta Mater 2011.

[4] Sadangi RK, McCandlish LE, Kear BH, Seegopaul P. Int J Powder Met 1999;35:27.

[5] Morton CW, Wills DJ, Stjernberg K. Int J Refract Met H 2005;23:287.

[6] Sun L, Jia CC, Cao RJ, Lin CG. Int J Refract Met H 2008;26:357.

[7] Guo J, Fan P, Fang ZZ. Proceedings of the 17th international Plansee seminar, Metallwerk, Reutte, Austria. 2009.

[8] Guo J, Fan P, Fang ZZ. Proceedings of Int Conf on Powder Metallurgy & Particulate Materials, Hollywood, FL. 2010.

[9] Fan P, Fang ZZ, Guo J, Wang X. Submitted.

[10] Fang ZZ, Fan P, Guo J. US Patent, pending.

[11] Guo J, Fan P, Wang X, Fang ZZ. Accepted by Int J Powder Met 2011.

[12] Frisk K, Markstrom A. Int J Mat Res 2008;99:287.

[13] Schwarzkopf M, Exner HE, Fischmeister HF. Metall Mater Trans A 1988;A105-106:225.

[14] Ekroth M, Frykholm R, Lindholm M, Andren HO, Agren J. Acta Mater 2000;48:2177.

CHAPTER 5

KINETIC MODEL

The postsintering carburization process has proved to be effective for producing FG WC-Co for a wide range of WC-Co grades; showing that the graded structure relies on the kinetic control of the process. To achieve a desired or designed gradient, a study of the kinetics of the overall process is indispensable. The mechanism of the gradient formation suggests that the kinetics of the gradation are the results of several subprocesses involved in the carburization process: (i) surface carburizing reaction, (ii) carbon diffusion in the semisolid-semiliquid material, (iii) carbon diffusion in the fully solid material, (iv) phase transformation of solid Co to liquid Co, and (v) the migration of liquid Co. This dissertation assumes that the carbon diffusion is rate controlling step for the kinetics of the overall process. Therefore, a diffusion controlled kinetic model is derived in the following section.

5.1 Description of the Model

The process model is established and illustrated with the schematic diagram of Figure 5.1. The concentration of carbon in the Co binder phase varies with the distance (x) from the surface. Before the process begins (t=0), initial carbon composition in Co phase throughout the material is uniform at $[C]_i$. Since the initial overall-carbon-content (C_i) of WC-Co sample is located in the Co(s)-WC(s) two-phase region (as denoted in Figure 3.1)

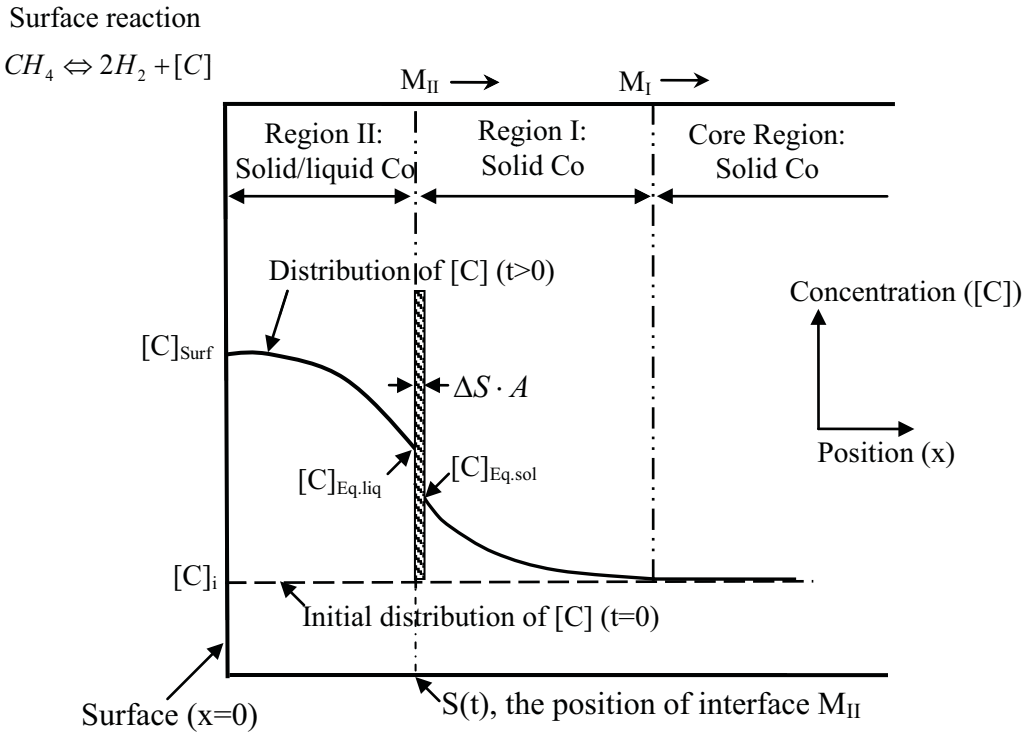

Figure 5.1 Schematic illustration of the model for describing the kinetics of gradient formation during the carburizing heat treatment process.

, there is no liquid phase existing prior to the process at any given temperature within the range of the triple phase field (1300^{o}C, for instance). Upon carburization (t>0), the overall-carbon-content of the material is increased to a value higher than C_i and correspondingly the carbon concentration in the Co phase near the surface is increased to $[C]_{Surf}$ (Figure 5.1) as a result of the diffusion of carbon into the material, even though the carbon composition in the not yet affected core region is still homogeneous at $[C]_i$. The difference in the carbon concentration in Co between the surface and the core of the specimen, expressed by ($[C]_{Surf}$ -$[C]_i$) provides the driving force for the inward carbon diffusion. A carbon gradient is thus formed near the surface region in which the carbon content decreases gradually from $[C]_{Surf}$ to $[C]_i$ as a function of depth from surface, x.

When the carbon concentration in the Co phase is increased to a threshold value corresponding to the overall-carbon-content of C_S (as seen in Figure 3.1), the solid Co phase is partially transformed to liquid according to the phase equilibrium of W-C-Co system (Figure 3.1).

As a result, two moving interfaces (M_I and M_{II}) are formed in the near surface region. As shown in Figure 5.1, the interface M_I represents the carbon diffusion front which separates the carburized surface region and the not yet affected core region; M_{II} represents the boundary between the region (Region I) that contains solid Co phase only and the region (Region II) that contains both solid and liquid Co.

The entire process of the Co gradient formation the consists of several subprocesses: the deposition of methane at the surface, solution of carbon in Co at the surface, the diffusion of carbon in the Co phase, the phase transformation of solid to liquid Co, and the migration of liquid phase once there is a gradient of the volume fraction of liquid Co phase. First, it is reasonable to assume that the processes of surface reaction and the solution of carbon in Co are not the rate controlling step otherwise there would be neither carbon nor cobalt gradient within the material. Second, the phase transformation from solid to liquid Co is generally a diffusion-controlled process and only the interfacial transition from solid to liquid needs to be considered as a part of the overall process. Lastly, the migration of the liquid phase from the surface area with higher volume fraction of liquid to the core area with lower volume fractions of liquid is also a relatively rapid process based on previous published research of the present author [1]. Considering the above, it is therefore assumed that diffusion is the rate controlling step of the whole process of the formation of Co gradient. The governing equations shall thus be

established based on the diffusion of carbon through the solid and liquid phase of Co. The first moving interface M_I is determined by the maximum distance of carbon diffusion, whereas the second interface M_{II} is determined by the diffusion of carbon through the liquid Co phase. By modeling the diffusion of carbon and therefore the carbon compositional profile, the positions of the two moving interfaces can be determined as a function of time, which in turn allows us to estimate the distance of Co migration, i.e. the thickness of the gradient.

5.2 Governing Equations

On a basis of the above assumptions, the process problem can be modeled as a one-dimensional diffusion-controlled, two-phase moving boundary problem. Diffusion controlled moving boundary problems occur in a wide range of physical and engineering processes that associate with heat transfer or mass diffusion incorporating a concurrent phase transformation [2-4]. In this dissertation, the governing equations are formulated according to Fick's second law.

Therefore, the diffusion equation in Region I can be expressed as:

$$\frac{\partial [C]_{Sol}}{\partial t} = D_S^{eff} \frac{\partial^2 [C]_{Sol}}{\partial x^2}, \text{ for } S(t) < x < L \tag{5.1}$$

where $[C]_{Sol}$ is the carbon concentration in solid Co phase in unit of molar fraction (mol %) which is a function of position, x and time t. D_S^{eff} is the effective diffusion coefficient of carbon in solid Co phase and is assumed to be constant independent of x. $S(t)$ as labeled in Figure 5.1 is the position of interface M_{II} at time, t. L is the position of the far boundary from the surface.

To obtain the diffusion equation for Region II which is a mixture of WC, solid Co, and liquid Co phase, only the diffusion in the liquid is considered because the diffusion in the solid is negligible. The governing equation for the diffusion in the Region II is thus expressed as:

$$\frac{\partial [C]_{Liq}}{\partial t} = D_L^{eff} \frac{\partial^2 [C]_{Liq}}{\partial x^2}, \text{ for } 0 < x < S(t) \tag{5.2}$$

where $[C]_{Liq}$ is the carbon concentration in liquid Co phase in molar fraction (mol%) varying with t and x. D_L^{eff} is the effective diffusion coefficient of carbon in the liquid Co phase and is assumed to be constant, which is independent of position, x.

Equations (5.1) and (5.2) have the following boundary equations:

$$[C] = [C]_{Surf}, \text{ for } x = 0,\ t > 0$$

$$[C] = [C]_i, \text{ for } x = L,\ t > 0$$

where $[C]_{Surf}$ is the carbon concentration at the surface. $[C]_{Surf}$, depending on the heat treating temperature and the carbon potential of the atmosphere, is assumed to be constant during the process.

The initial condition is given as:

$$[C] = [C]_i, \text{ for } 0 < x < L,\ t = 0$$

Considering the mass conservation at the moving interface M_{II}, the net flux of carbon within an infinite small volume ($\Delta S \cdot A$, where A is the cross-section area for flux) near M_{II} should be equal to the mass accumulation. Thus, the boundary equation is derived as:

$$D_S^{eff} \frac{\partial [C]_{Sol}}{\partial x} \Big| (x = S(t)) - D_L^{eff} \frac{\partial [C]_{Liq}}{\partial x} | (x = S(t)) = ([C]_{Eq.liq} - [C]_{Eq.sol}) \cdot \frac{dS(t)}{dt} \quad (5.3)$$

where $[C]_{Eq.liq}$ and $[C]_{Eq.sol}$ are the concentrations of carbon in liquid and solid Co respectively at M_{II}. Assuming the system is locally at thermodynamic equilibrium at M_{II}, $[C]_{Eq.liq}$ and $[C]_{Eq.sol}$ are the equilibrium carbon compositions that can be determined from the equilibrium phase diagram.

5.3 Analytical Solution

The governing equations (5.1)-(5.3) form a coupled system of nonlinear differential equations and can be solved analytically using error functions along with the boundary and initial conditions [2-4]. The solutions to the equations (5.1) and (5.2) are given by:

$$[C]_{Liq} = [C]_{Surf} - ([C]_{Surf} - [C]_{Eq.liq}) \cdot \frac{erf(\frac{x}{2\sqrt{D_L^{eff} \cdot t}})}{erf(\lambda)}, \text{ for } 0 < x < S(t) \quad (5.4)$$

$$[C]_{Sol} = [C]_i + ([C]_{Eq.sol} - [C]_i) \cdot \frac{erfc(\frac{x}{2\sqrt{D_S^{eff} \cdot t}})}{erfc(\lambda \cdot \sqrt{D_L^{eff} / D_S^{eff}})}, \text{ for } S(t) < x < L \quad (5.5)$$

where λ is a constant to be determined. The position of the interface, *S(t)* must be proportional to $\sqrt{t}$ to satisfy equations (5.4) and (5.5) for any *t*, i.e.,

$$S(t) = 2 \cdot \lambda \cdot \sqrt{D_L^{eff} \cdot t} \tag{5.6}$$

It should be noted that λ is a constant with respect to only t and x; but it would change depending on specific composition conditions such as the partial pressure ratio of gases in the atmosphere.

Differentiating equations (5.4), (5.5), and (5.6) and substituting them into equation (5.3), we obtain:

$$\frac{([C]_{Surf} - [C]_{Eq.liq})}{\exp(\lambda^2) \cdot erf(\lambda)} - \frac{([C]_{Eq.sol} - [C]_i)}{v \cdot \exp(v^2 \cdot \lambda^2) \cdot erfc(v \cdot \lambda)} = ([C]_{Eq.liq} - [C]_{Eq.sol}) \cdot \lambda \cdot \sqrt{\pi} \tag{5.7}$$

where $v = \sqrt{D_L^{eff} / D_S^{eff}}$. To obtain the unknown constant λ, the transcendental equation (5.7) will be solved iteratively using the so-called Newton's method [5], which is described as follows.

5.4 Dependence of Gradient as Function of Key Process Factors

This section focuses on establishing a quantitative relation between the gradients and the key process factors including $P_{CH4}/P_{H2}{}^2$ ratio of the heat treating atmosphere and time. This is accomplished based on the kinetic model as described above. Prior to carrying out the computations, the numeric parameters involved in the model need to be determined. Most of the parameters were determined through thermodynamic calculations. For some parameters that are not available in literature, they are estimated using a regression-fitting procedure based on the experimental data of this dissertation, which will be elaborated as follows.

5.4.1 Determination of Parameters

In order to solve equation (5.7), we must determine all the numerical parameters including the parameter λ, diffusion coefficients D_S^{eff} and D_L^{eff}, and all the composition values as shown in equation (5.7). We will first assign a value of $D_L^{eff}(i)$ and back calculate a corresponding $\lambda(i)$ from equation (5.7) using the technique of Newton's method. $\lambda(i)$ is then used to calculate a value $S(t)(i)$ that corresponds to the set of values of D_L^{eff} and λ based on equation (5.6). The value of $S(t)(i)$ is then compared to experimentally determined thickness of gradient. The absolute difference ($|\Delta|$) between the calculated $S(t)$ and the experimental value will be used as a criterion to determine the values of D_L^{eff} and λ. When $|\Delta|$ is less than 1.0, the iterative calculations will stop, otherwise the program continues to run until an acceptable set of D_L^{eff} and λ values are found.

To carry out the above algorithm, however, the values of $[C]_{Surf}$, $[C]_{Eq.liq}$, $[C]_{Eq.sol}$, $[C]_i$, and D_S^{eff} must be known. The equilibrium carbon compositions at the interface ($[C]_{Eq.liq}$ and $[C]_{Eq.sol}$) in molar fraction (mol%) can be determined from ternary Co-W-C phase diagram at 1300°C [6]. The ternary Co-W-C phase diagram is available in the literature based on calculations using commercial thermodynamic simulation software, such as Thermo-calc [7]. Figure 5.2a plots the relationship between the carbon concentrations in Co phase and the overall-carbon-content of WC-Co composite at 1300°C. Within the Co(s)-Co(l)-WC(s) equilibrium region, $[C]_{Eq.liq}$ is 10.56 mol% and $[C]_{Eq.sol}$ is 2.76 mol% as noted in Figure 5.2a.

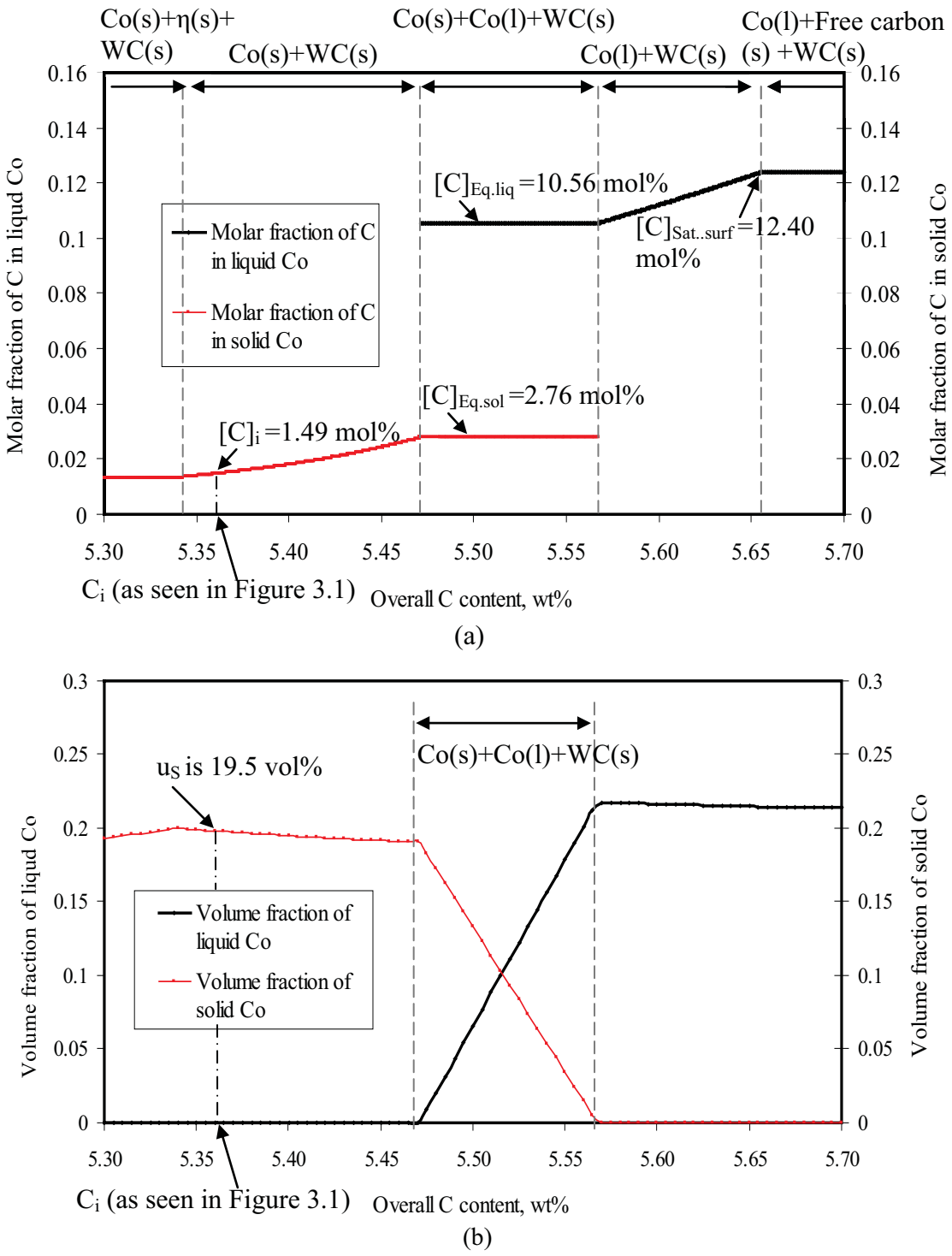

Figure 5.2 The dependences of (a) molar fractions of carbon ([*C*]) at 1300°C as a function of the overall-carbon-content of WC-Co with a constant Co content of 10.0 wt% and (b) volume fractions of solid Co (u_S) and liquid Co (u_L) at 1300°C as a function of the overall-carbon-content of WC-Co with a constant Co content of 10.0 wt%.

Similarly, the initial carbon composition in the cobalt phase, $[C]_i$ can be obtained from its raw material composition and the dependence of the carbon composition as a function of the overall-carbon-content. As the overall-carbon-content of WC-10Co sample studied in this paper is designed to be 5.36 wt%, $[C]_i$ is obtained as 1.49 mol% from Figure 5.2a.

Further, D_S^{eff} is needed for carrying out the algorithm to determine D_L^{eff} and λ. According to the experimental studies on the solid state dissolution of carbon in Co, the diffusion coefficient of carbon in solid cobalt is 40 $\mu m^2/s$ at 1300°C [8, 9]. However, considering the labyrinth effect [10, 11], the effective diffusion coefficient should be calculated as:

$$D_S^{eff} = (u_S)^2 \cdot D_S \tag{5.8}$$

where u_S is the volume fraction of solid Co phase. u_S can be determined from the molar volumes and mole fractions of WC, solid Co and liquid Co phases. The molar volumes of WC, solid Co and liquid Co were calculated based on the reported dependence of molar volume of each individual phase as a function of their compositions and temperatures [12]. As mentioned in this section, the compositions of the solid and liquid Co phase can be obtained from the W-C-Co ternary phase diagram and the results were shown in Figure 5.2a. Then the dependences of u_s versus the overall-carbon-content of WC-Co at 1300°C were obtained and plotted in Figure 5.2b, in which the volume fraction of solid Co phase (u_S) within Region II is obtained to be 19.5 vol%. Thus, the effective diffusion coefficient (D_S^{eff}) in Region II is given as 1.5 $\mu m^2/s$.

Another compositional parameter that needs to determine is $[C]_{Surf}$ - the carbon concentration in the Co at the surface. $[C]_{Surf}$ depends on the carbon potential in the atmosphere, namely the ratio of partial pressures of gases in the atmosphere. However, once the cobalt phase is saturated when the carbon potential is high enough, $[C]_{Surf}$ will remain constant at $[C]_{Sat.surf}$. Further increase of the overall-carbon-content will lead to the precipitation of free carbon phase. Using the same approach for calculating $[C]_{Eq.liq}$ and $[C]_{Eq.sol}$, the $[C]_{Sat.surf}$ is determined to be 12.40 mol% (as denoted in Figure 5.2a).

With the known $[C]_{Eq.liq}$, $[C]_{Eq.sol}$, $[C]_i$, D_S^{eff} , and $[C]_{Sat.surf}$, D_L^{eff} can be determined by fitting the calculated position of interface M_{II}, namely *S(t)*, with the experimentally measured thickness of gradient obtained under the atmosphere with the $P_{CH4}/P_{H2}{}^2$ ratio of 1/35 atm^{-1}. This is because when the sample is treated under this atmosphere, free carbon phase was precipitated near surface of the material suggesting that $[C]_{Surf}$ reached the value of $[C]_{Sat.surf}$ (12.40 mol%). Following the procedure described in the first paragraph of this section, D_L^{eff} was obtained to be 33.0 $\mu m^2/s$ since it gave the best-fitting results.

To determine the values of $[C]_{Surf}$ at other levels of carbon potential in the atmosphere, we need to rely on using all the known parameters as described above including the effective diffusion coefficient of carbon in the liquid phase D_L^{eff} , which had been determined to be 33.0 $\mu m^2/s$. The dependence of $[C]_{Surf}$ on $P_{CH4}/P_{H2}{}^2$ ratio of the atmosphere is assumed to follow a polynomial relationship as:

$$[C]_{Surf} = a_0 + a_1 \cdot P_r + a_2 \cdot (P_r)^2 \tag{5.9}$$

where a_0, a_1, and a_2 are empirical coefficients to be determined. As mentioned in Section 4.1.2.1, the ratio of the partial pressures of the gases in the atmosphere (P_r) is given as $P_{CH4}/P_{H2}{}^2$. To determine the empirical coefficients a_0, a_1, and a_2, another iterative algorithm based on Newton's method is used. At the beginning of the iterative procedure, an arbitrary value of $[C]_{Surf}$ is used in equation (5.7), which allows calculation of a new λ. Note that D_L^{eff} is already determined and is held as a constant, i.e, 33.0 $\mu m^2/s$. Based on the new λ, equation (5.6) is used to calculate *S(t)* which will be compared with the experimental value of the thickness of gradient. If the difference between the calculated *S(t)* and the experimental value is unsatisfactory, a new $[C]_{Surf}$ will be selected for a new iteration. The procedure will continue until it is found a $[C]_{Surf}$ value that yields satisfactory agreement between the experimental data and the predicted thickness of gradient.

Using the above procedure, values of $[C]_{Surf}$ for each corresponding gas ratio P_r were calculated. The calculated values of $[C]_{Surf}$ was then used to fit equation (5.9) using linear regression procedures. The polynomial coefficients were thus obtained as a_0=0.1100, a_1=-0.6722 and a_2=40.4915. Therefore, the dependence of $[C]_{Surf}$ as a function of P_r is expressed as:

$$[C]_{Surf} = 0.1100 - 0.6722 \cdot P_r + 40.4915 \cdot (P_r)^2 \qquad (5.10)$$

and also plotted in Figure 5.3. Using equation (5.10), we can predict the surface composition as a function of atmosphere $P_{CH4}/P_{H2}{}^2$. Therefore, it allows us to design Co gradients by varying the composition of the atmosphere, which will be discussed later.

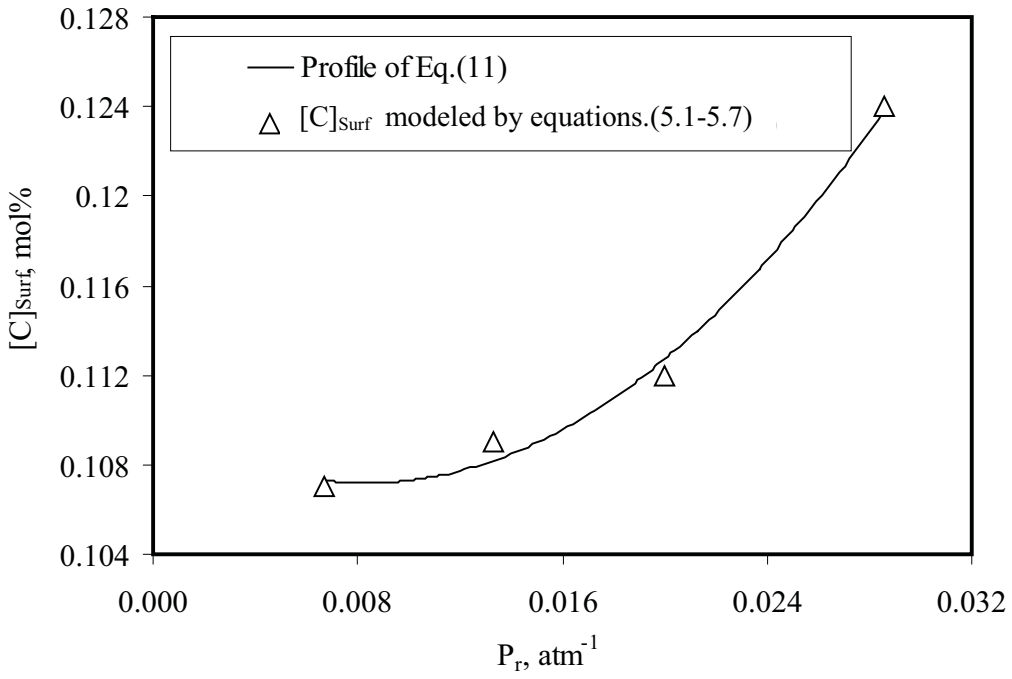

Figure 5.3 Predicted values of $[C]_{Surf}$ vs P_r and the simulated profiles for correlating $[C]_{Surf}$ and P_r.

5.4.2 Prediction of Gradient Thickness as Function of P_r and t

There are mainly two kinds of outputs from this model: (i) the distribution of carbon concentration and (ii) the position of the moving interface M_{II}. As an example, the calculated carbon profile vs distance (x) from the surface for the sample heat treated under the atmosphere of $P_{CH_4}/P_{H_2}^{\ 2}$ ratio of 1/150 atm^{-1} at 1300°C for 60 minutes is plotted in Figure 5.4. It shows the position of the interface M_{II} is 54.0 μm from the original surface, indicating that the thickness of the gradient zone would be approximately the same.

Simulations were performed to predict the thickness of gradient zones as a function of time. The calculated results are compared to the experimental data as shown in Figure 4.5 (Section 4.1.2.2). For samples heat treated for 15-240 minutes, the simulated results agree

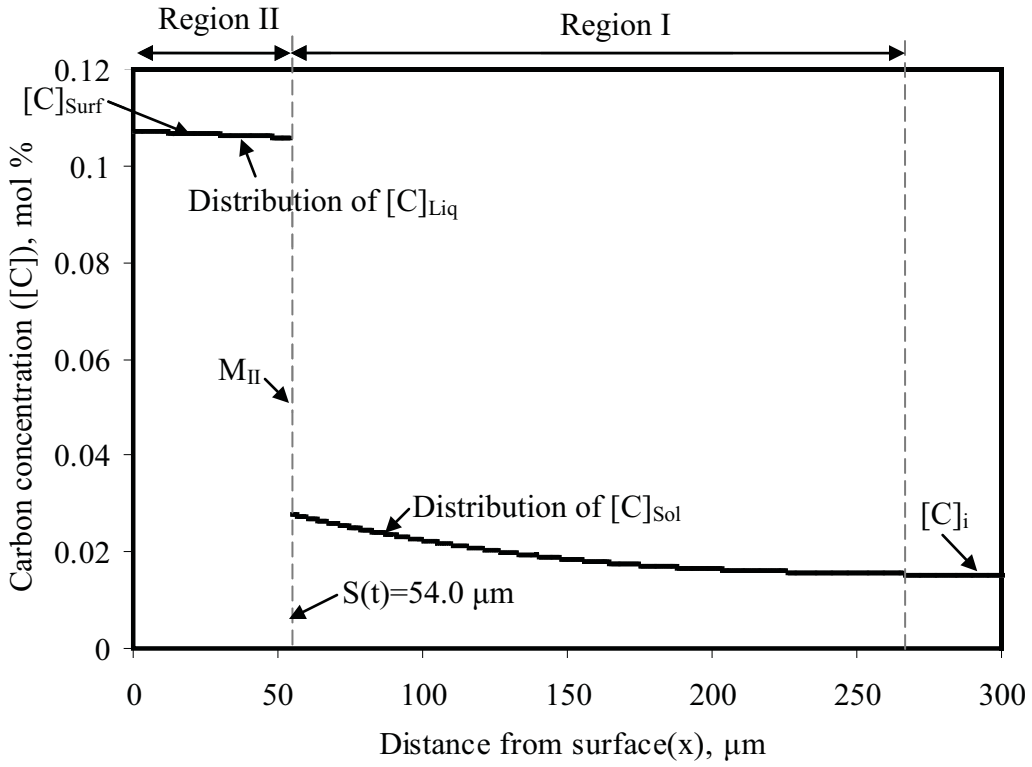

Figure 5.4 Simulated profiles of carbon composition in Co phase in the WC-10Co sample treated under the atmosphere of $P_{CH_4}/P_{H_2}^{\ 2}$ ratio of 1/150 atm^{-1} at 1300°C for 60 minutes.

well with the experimental data. However, there is a significant discrepancy between the two when the holding times are longer than 360 minutes. This is qualitatively understood on the basis that the cobalt content near the surface is very low after such an extended period of time due to the loss of cobalt for migration. In that case, the assumption of constant diffusion coefficient is no longer valid.

The mathematic model was also used to compute the thickness of the gradient as a function of atmosphere conditions. The simulated results of gradient thickness as a function of $P_{CH_4}/P_{H_2}^{\ 2}$ ratio of the atmosphere are plotted in Figure 5.5. The experimental

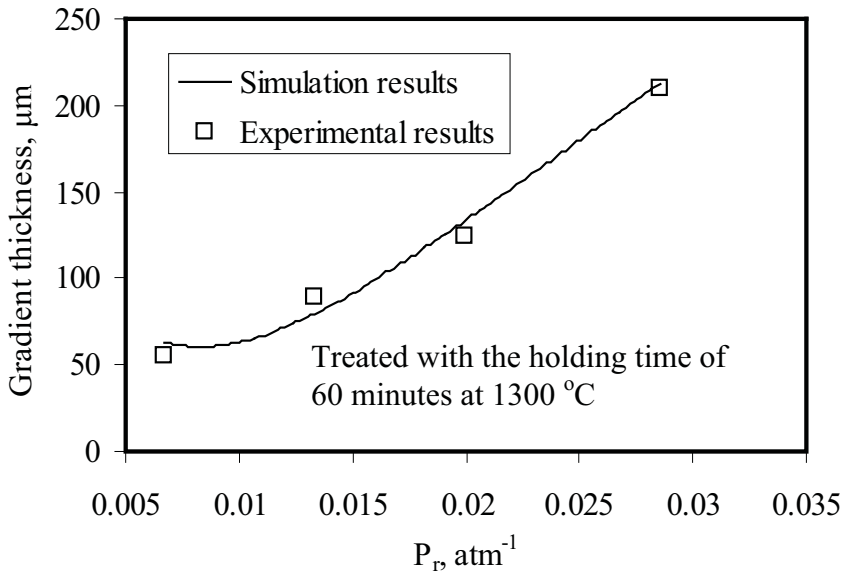

Figure 5.5 Comparison of experimentally measured thicknesses of Co gradients with simulation results.

values of the thicknesses of gradient are included in Figure 5.5 for comparison. Clearly the model and experimental results agree well.

From an industrial perspective, establishing the quantitative dependence of the thickness of the gradient on the two primary processing parameters is very important because it defines the envelope of processing parameters. To further illustrate the utility of the model, the simulated thicknesses of cobalt gradient as a function of both the atmosphere and time were computed and shown in Figure 5.6, in which each trend line shows the dependence of gradient thickness on the $P_{CH4}/P_{H2}^{\ 2}$ ratio of the carburizing atmosphere while holding the length of time of heat treatment constant. Figure 5.6 can be used for practical designs the preferable Co gradients by selecting proper heat treatment conditions.

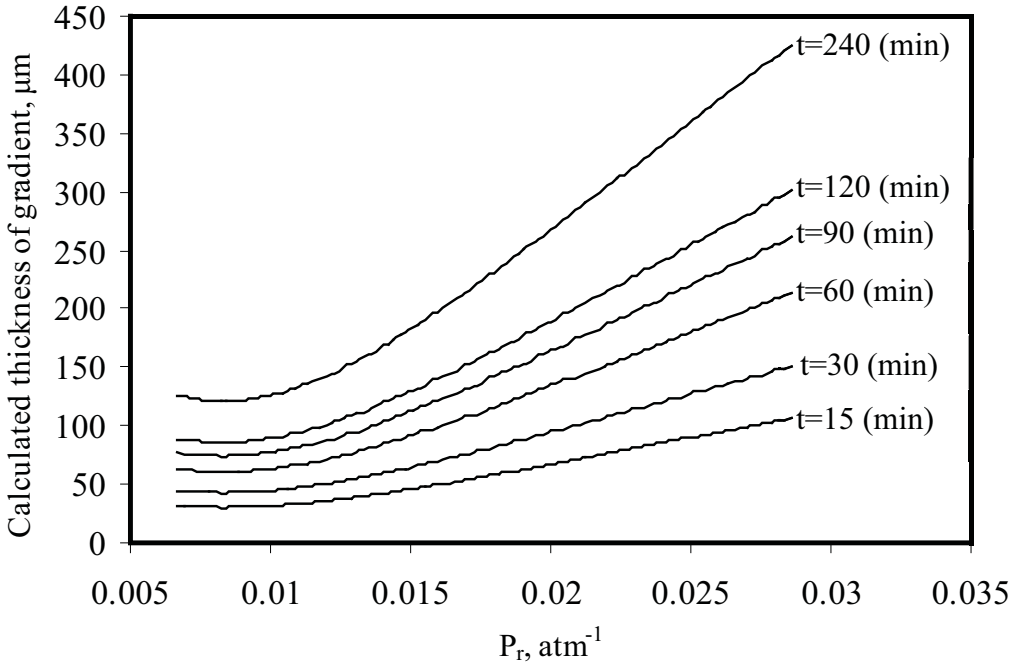

Figure 5.6 Simulated thicknesses of Co gradients as function of the atmosphere, P_r and time, t at the heat treating temperature of 1300°C.

5.5 Dependence of Gradient as Function of Key Materials Factors

In this section, the effects of key material factors (Co content and grain size) were modeled and simulated. This is done through a similar procedure proposed for analyzing the effects of the processing as described in Section 5.4.

5.5.1 Determination of Parameters

In order to predict the formation of gradient employing the kinetic model described above, the following parameters are taken as inputs to solve partial differential equations (1)-(3) analytically including:

(1) The equilibrium interface carbon compositions, $[C]_{Eq.liq}$ and $[C]_{Eq.sol}$, respectively;

(2) The surface and bulk carbon compositions, $[C]_{Surf}$ and $[C]_i$, respectively;

(3) The effective diffusion coefficient in solid and liquid Co phase, D_S^{eff} and D_L^{eff}, respectively.

The equilibrium carbon compositions at the interface ($[C]_{Eq.liq}$ and $[C]_{Eq.sol}$) in unit of molar fraction (mol%) can be determined from a ternary Co-W-C phase diagram at 1300°C [6]. The ternary Co-W-C phase diagram is available in literature based on calculations using commercial thermodynamic simulation software, such as Thermo-calc [7]. Figure 5.7 plots the relationship between the carbon concentrations in Co phase and

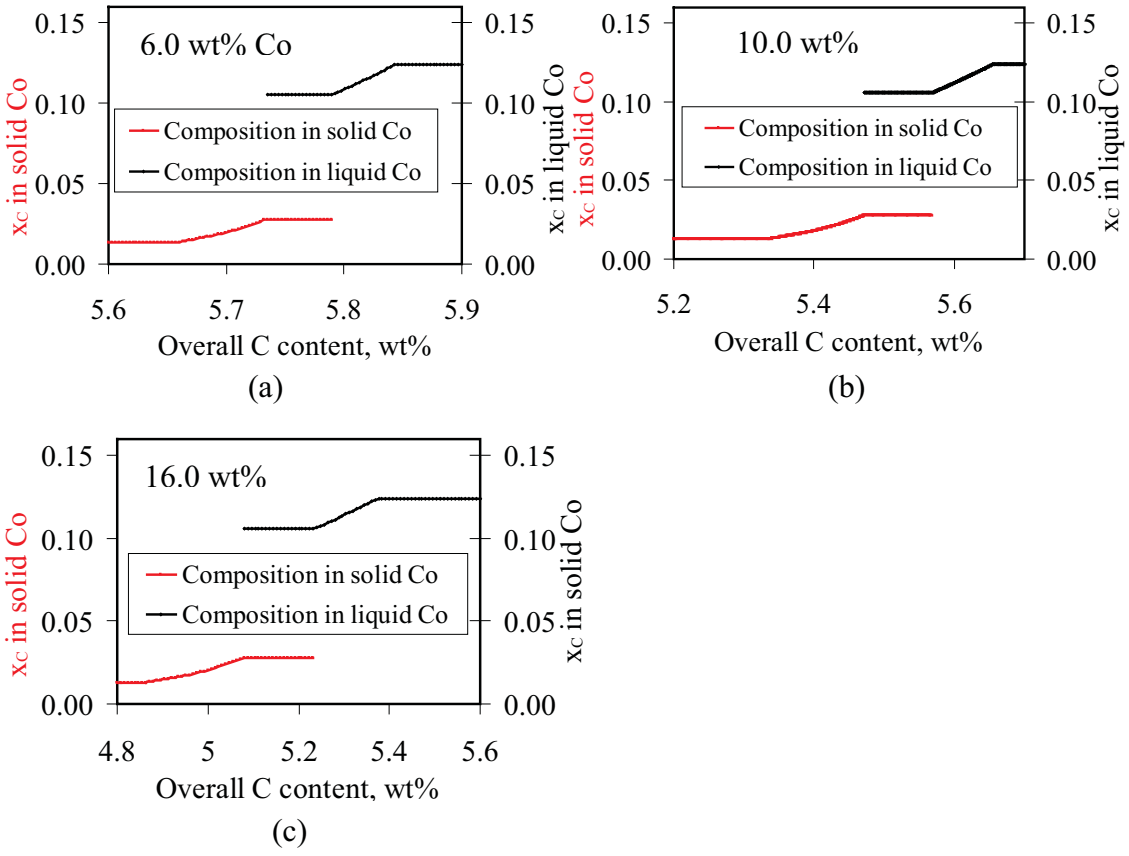

Figure 5.7 Molar fractions of carbon (x_C) in solid Co and liquid Co at 1300°C with constant Co contents of (a) 6.0 wt%, (b) 10.0 wt% and (c) 16.0 wt%.

the overall-carbon-content of WC-Co composites with constant Co contents of 6.0, 10.0 and 16.0 wt% at 1300°C. Within the Co(s)-Co(l)-WC(s) equilibrium region, $[C]_{Eq.liq}$ and $[C]_{Eq.sol}$ for each WC-Co sample used in this study are denoted in Figure 5.7 and listed in Table 5.1. Similarly, the initial carbon content in the cobalt phase, $[C]_i$ of each WC-Co sample can be obtained from its raw material composition (Table 4.1 in Section 4.2.1.1) and the dependence of the carbon composition as a function of the overall-carbon-content of Figure 5.7. The results of $[C]_i$ are given in Table 5.1.

Another compositional parameter that needs to be obtained is $[C]_{Surf}$ - the carbon concentration in the Co at the surface, which is a parameter dependent on the atmosphere $P_{CH4}/P_{H2}{}^2$ (namely, P_r). As described in Section 5.4.1, it has derived an empirical expression (ie., equation (5.10)) to describe the variation of $[C]_{Surf}$ as a function of P_r. Thus, using equation (5.10), the values of $[C]_{Surf}$ for the corresponding atmospheres (Tables 4.2 and 4.3 in Section 4.2.1.2) can be obtained and summarized in Table 5.2.

Further, D_S^{eff} needs to be known. It has been described in Section 5.4.1 that D_S^{eff} can be determined using equation (5.8) by considering the labyrinth effect on carbon diffusion in composite materials. To be able to employ equation (5.8), the volume fraction of solid Co phase (u_S) needs to be known. In this research, u_S was determined

Table 5.1 Values of carbon contents used in simulation

Samples	Initially overall carbon contents (wt%)	$[C]_{Eq.liq}$ (mol%)	$[C]_{Eq\cdot sol}$ (mol%)	$[C]_i$ (mol%)
$WC_{(f)}$-10Co	5.36	10.56	2.76	1.49
$WC_{(m)}$-10Co	5.36			
$WC_{(c)}$-10Co	5.36			
$WC_{(c)}$-6Co	5.67			
$WC_{(c)}$-16Co	4.91			

Table 5.2 $[C]_{Surf}$ at different atmosphere conditions

P_r (atm^{-1})	$[C]_{Surf}$ (mol %)
1/30	12.40
1/40	11.90
1/50	11.30
1/75	10.95
1/150	10.70

from the molar volumes and mole fractions of WC, solid Co and liquid Co phases. The molar volumes of WC, solid Co and liquid Co were calculated based on the reported dependence of molar volume of each individual phase as a function of their compositions and temperatures [12]. It has been mentioned in Section 5.4.1 that the compositions of the solid and liquid Co phase can be obtained from the W-C-Co ternary phase diagram with the results shown in Figure 5.7. Then the dependences of u_S versus the overall-carbon-content of WC-Co at 1300°C were obtained and depicted in Figure 5.8, according to which the volume fraction of solid Co phase within Region II, u_S is determined and exact values of D_S^{eff} for each individual sample are acquired in Table 5.3.

To determine the effective diffusion coefficient (D_L^{eff}) for carbon diffusion within Region II (see Figure 5.1), we assume it to be constant for a particular sample. D_L^{eff} is obtained through the following best-fitting procedure based on the experimental data of measured gradient thickness. As an example, the procedure for calculating D_L^{eff} of the $WC_{(f)}$-10Co sample is given as follows. Firstly, we will assign a arbitrary value of D_L^{eff}. The arbitrary value of D_L^{eff} along with the known parameters of $[C]_{Eq.liq}$ and $[C]_{Eq.sol}$, $[C]_i$,

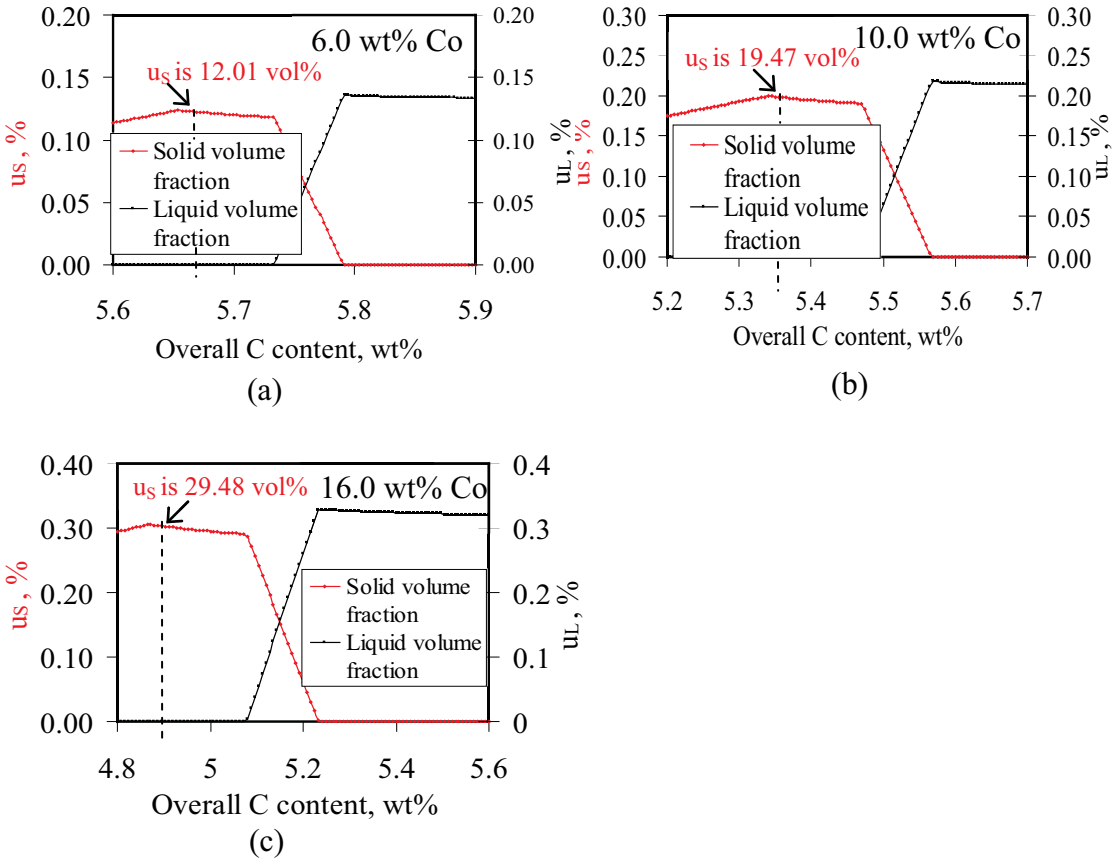

Figure 5.8 Volume fractions of solid Co (u_S) and liquid Co (u_L) at 1300°C as a function of the overall-carbon-content of WC-Co with constant Co contents of (a) 6.0 wt%, (b) 10.0 wt% and (c) 16.0 wt%.

Table 5.3 Values of u_S and D_S^{eff}

Samples	Co contents (wt%)	Region II	
		u_S (vol%)	D_S^{eff} (μm^2/s)
$WC_{(f)}$-10Co	10	19.47	1.517
$WC_{(m)}$-10Co	10	19.47	1.517
$WC_{(c)}$-10Co	10	19.47	1.517
$WC_{(c)}$-6Co	6	12.01	0.576
$WC_{(c)}$-16Co	16	29.48	3.476

$[C]_{Surf}$ and D_S^{eff} (Tables 5.1-5.3) are used as inputs to calculate the corresponding λ from equation (5.7). As there are four different atmosphere conditions used to treat the $WC_{(f)}$-10Co sample, it will have four $[C]_{Surf}$ values for each atmosphere condition and correspondingly we will obtain four values of λ, namely λ_1, λ_2, λ_3 and λ_4. Secondly, we use the λ_1, λ_2, λ_3 and λ_4 values to compute the gradient thicknesses of $S(t)$ based on equation (5.6) and so that it will arrive four $S(t)$ values that are $S(t)_1$, $S(t)_2$, $S(t)_3$, and $S(t)_4$ respectively. Thirdly, the calculated values of $S(t)_1$, $S(t)_2$, $S(t)_3$, and $S(t)_4$ are compared to the experimentally measured gradient thickness, namely $(X_G)_1$, $(X_G)_2$, $(X_G)_3$, $(X_G)_4$ for the purpose of computing the sum of difference (R^2) between the simulated results and the experimental data. R^2 is calculated by the following equation:

$$R^2 = \sum_{n=1}^{4} (S(t)_n - (X_G)_n)^2 \tag{5.11}$$

where n is the series of the atmosphere conditions and X_G is the measured gradient thicknesses that could be found in Tables 5.4-5.5. Fourthly, R^2 is taken as a criterion to determine D_L^{eff}, which means that the iterative calculations will not stop unless R^2 is minimized and finally an acceptable D_L^{eff} value is found.

Table 5.4 Experimentally measured gradient thicknesses of X_G

Gradient thickness X_G (μm) / Sample	P_r of atmosphere (atm^{-1})			
	1/35	1/50	1/75	1/150
	$(X_G)_1$	$(X_G)_2$	$(X_G)_3$	$(X_G)_4$
$WC_{(f)}$-10Co	287.5	209.6	125.41	125.41
$WC_{(m)}$-10Co	209.06	125.41	91.95	55
$WC_{(c)}$-10Co	142.14	91.95	41.76	25.03

Table 5.5 Experimentally measured gradient thicknesses of X_G

Gradient thickness X_G (μm) / Sample	P_r of atmosphere (atm^{-1})		
	1/40	1/75	1/150
	$(X_G)_1$	$(X_G)_2$	$(X_G)_3$
$WC_{(c)}$-6Co	108.68	75	55
$WC_{(c)}$-10Co	85	65	45
$WC_{(c)}$-16Co	75	25	15

Through the exactly same procedure as described above, D_L^{eff} for the rest of samples are acquired and their values were indicated in Figure 5.9. It also shows a comparison of the simulated gradient thickness and the experimentally measured gradient thickness. A good agreement is observed between the model and experimental results. It worth pointing out that for the $WC_{(c)}$-10Co sample, two sets of D_L^{eff} values (14.6 vs 11.0 $\mu m^2/s$) were obtained because this sample was treated in two groups of experiments (Tables 4.2-4.3 in Section 4.2.1.2). Even though the two values of D_L^{eff} were determined under different experimental conditions, they show a close agreement demonstrating that the model used for calculating the diffusion parameter is reliable.

5.5.2 Dependences of D_L^{eff} and D_S^{eff} on M_{Co} and d_{WC}

In previous models [11] for simulating component diffusion in composite materials, it is common to introduce a so-called labyrinth factor to multiply a bulk diffusivity to reduce the diffusion coefficient in matrix under the consideration that the diffusion in the matrix is partly blocked by the presence of dispersed grains [10]. This treatment is virtually based on two major hypotheses, namely, it only considers volume diffusion and the diffusion occurs only in the continuous matrix phase. The labyrinth factor, which has

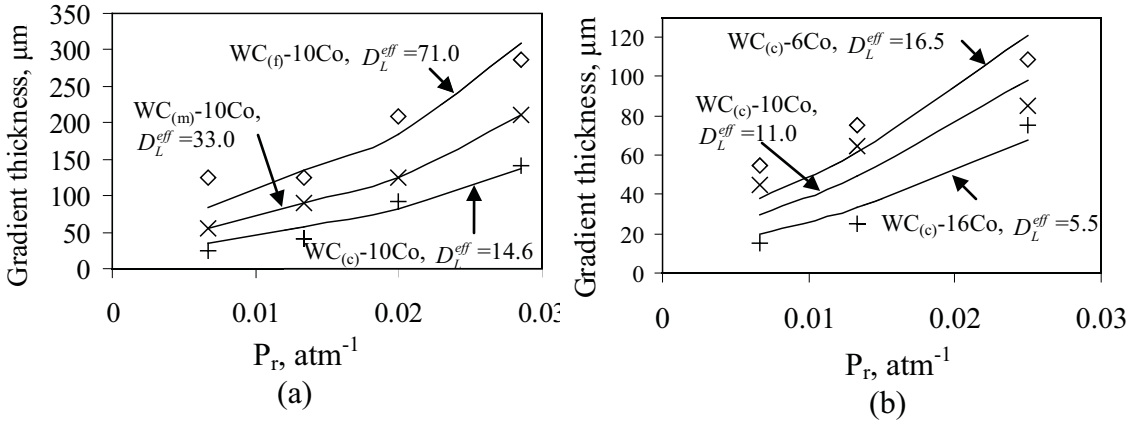

Figure 5.9 Comparison of experimentally measured gradient thickness vs simulated gradient thickness in samples of (a) $WC_{(f)}$-10Co, $WC_{(m)}$-10Co and $WC_{(c)}$-10Co and samples of (b) $WC_{(c)}$-6Co, $WC_{(c)}$-10Co and $WC_{(c)}$-16Co.

a value between zero to unity, depends on the fraction of dispersed grains, their morphology and size distribution. For some simple shapes and distributions of the grains, such as a random distribution of equally sized non-interacting spheres, the labyrinth factor (τ) can be calculated as [10, 11]:

$$\tau = u^2 \tag{5.12}$$

where u is the volume fraction of the matrix phase.

In this dissertation, we have tried to apply equation (5.12) to determine the diffusion coefficients (D_S^{eff} and D_L^{eff}) so as to predict the formation of gradients employing the established kinetic model. It turns out that the agreement between the simulations and the experimental results is however not satisfactory. Firstly, the simulations indicate that the material with higher nominal Co content will have larger volume fraction of Co phase and higher diffusion coefficient, therefore faster gradient growth. Yet, the experimental

observations of this study are completely opposite and the rate of gradient growth decreases rather than increases with Co content. Secondly, the simulations show that there is no difference in the gradients among the samples with varying grain size, which was not found in the experiments.

It seems that the labyrinth factor cannot explain the experimental results of the present work. We believe it is because here labyrinth factor does not apply to determine D_L^{eff} . It should be pointed out that it is still reasonable to use labyrinth factor to calculate D_S^{eff} for the diffusion in Region I (Figure 5.1) where the matrix Co is all in solid. However, if employing the labyrinth factor to calculate D_L^{eff} in the Region II composed of both solid and liquid Co, the labyrinth effect is no longer applicable because the labyrinth factor is proposed for the diffusion in continuous matrix phase (i.e., a fully solid or a fully liquid Co phase). In order to interpret the influences of Co content and grain size in this study, we believe the critical factor lies in the Co/WC and Co(solid)/Co(liquid) interface and they accelerate the kinetics of carbon diffusion. In fact, the transport of carbon can take place not only in the Co phase but also along the interfaces and in certain circumstance the interfaces can provide an easy path for faster diffusion. In that case, it is not difficult to understand that the material with finer the grain size and/or lower the binder content provides more interfacial area, thereby enhancing the kinetics of the carbon diffusion and promoting the gradient development. Hence, a Co gradient with wider thickness and greater amplitude is created in the materials with finer grain size and lower Co content.

The influence of Co content and WC grain size has been explained qualitatively. To quantitatively predict the formation of the gradient as function of material factors, a

simple way is to correlate diffusivities with these material factors. Following the procedures described previously in Section 5.4.1, we have obtained the modeled diffusion coefficients (D_L^{eff}) for the known grain size (d_{WC} in μm) and Co content (M_{Co} in weight percent) as listed in Table 5.6. It is clearly seen in Figure 5.10 that the value of D_L^{eff} varies linearly with $(d_{WC})^{-2}$ and $(M_{Co})^{-1}$. Then we assume an empirical relation to conclude the dependence of the diffusion coefficients on grain size and Co content:

$$D_L^{eff} = \frac{k}{d_{WC}^2 \cdot M_{Co}} \tag{5.13}$$

where k is a coefficient to be determined. From equation (5.13), k can be calculated with the measured d_{WC} and M_{Co} and the modeled D_L^{eff} . The calculated values of k are listed in Table 5.6 and it is found that k varies from 2.25 to 3.68. The scatter for the values of k may be attributed to the variations in measuring WC grain size and gradient thickness. Substituting an average value of k (k=3) into equation (5.13), the dependence of diffusion coefficient versus Co content and grain size is hence obtained to be:

$$D_L^{eff} = \frac{3}{d_{WC}^2 \cdot W_{Co}} \tag{5.14}$$

Table 5.6 Modeled values of D_L^{eff} and k

D_L^{eff} (μm^2/s)	M_{Co} (wt %)	d_{WC} (μm)	Calculated k
71	10	0.72	3.68064
33	10	1.02	3.43332
14.6	10	1.55	3.50765
16.5	6	1.62	2.598156
11	10	1.55	2.64275
5.5	16	1.60	2.2528

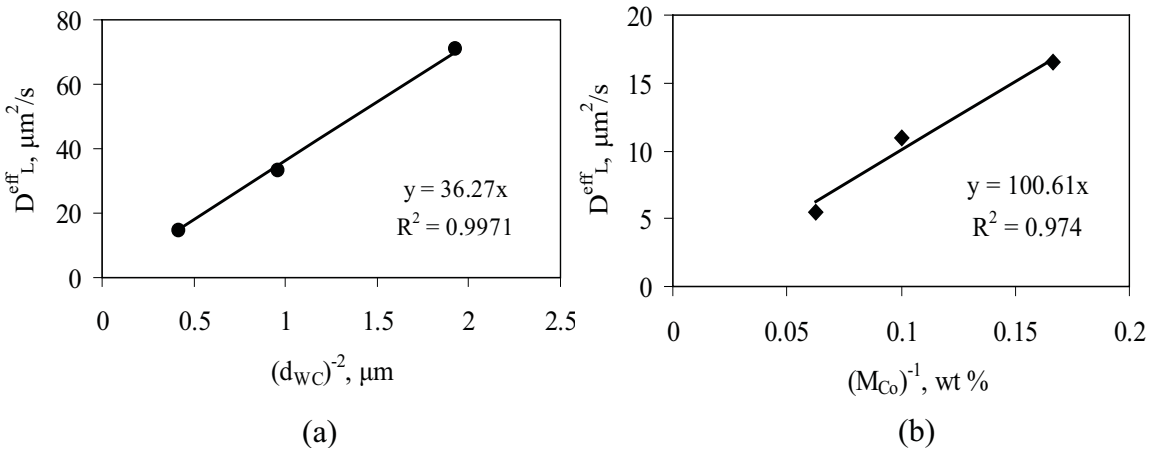

Figure 5.10 The plots of D^{eff}_L as function (a) $(d_{WC})^{-2}$ and (b) $(M_{Co})^{-1}$.

using equation (5.14), we can approximate D_L^{eff} as a function of the Co content and the grain size of the WC-Co material. With D_L^{eff} , we can design the gradients by using different WC-Co grades, which will be discussed in the following section.

5.5.3 Prediction of Gradient Thickness as Function of M_{Co} and d_{WC}

Following the procedure described above, simulations were performed to predict the effects of the key material factors. The calculated results of thicknesses of Co gradient as a function of Co content (M_{Co}) and WC grain size (d_{WC}) were shown in Figure 5.11, in which each trend line shows the dependence of gradient thickness on the grain size of materials while maintaining the Co content constant. Based on the theoretical simulations, a desired Co gradient can be designed by selecting the suitable WC-Co alloys.

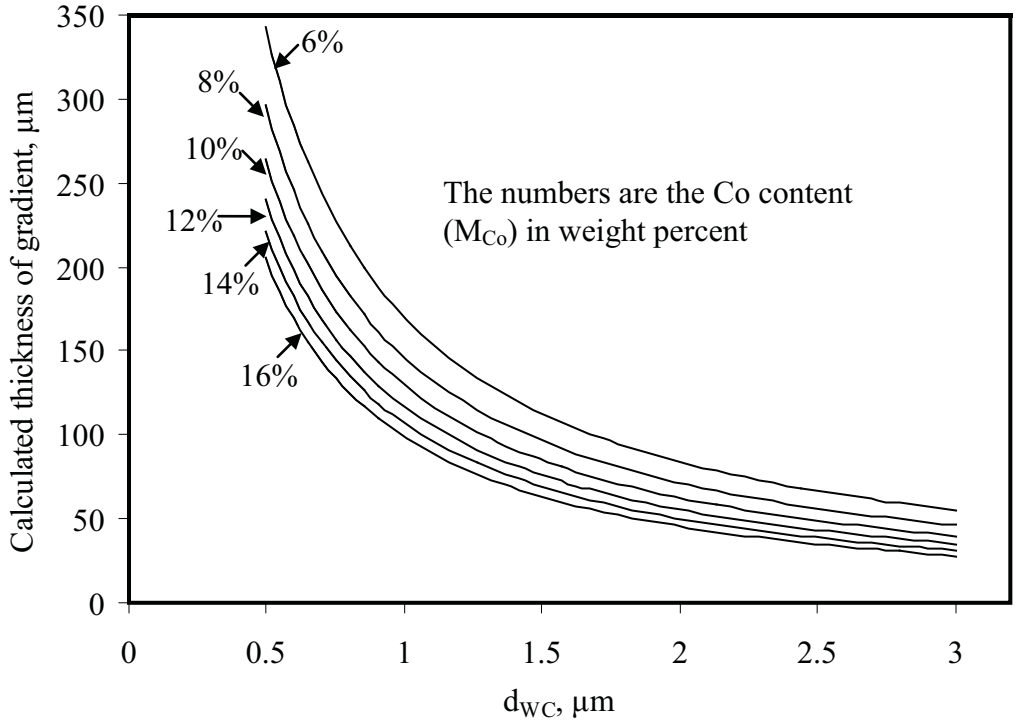

Figure 5.11 Simulated thickness of Co gradients as function of grain size (d_{WC}) and Co content (M_{Co}) formed under the atmosphere of $P_{CH4}/P_{H2}{}^{2}$ ratio of 1/50 atm^{-1} at 1300°C for 60 minutes.

5.6 Numerical Solution

The kinetic model can also be resolved numerically by a finite difference method. A numerical method developed by Zhou and North [13] was used in the present dissertation as a reference to validate the analytical method. This numerical method has been proved to be accurate and efficient for solving one-dimensional two-phase moving boundary problem. The detailed solution algorithm is given in the Appendix. The calculated results obtained by the numerical method are in good agreement with the solutions solved by the analytical method, which validated the reliability of this model.

5.7 Conclusions

A kinetic model has been established based on the assumption that the carbon diffusion process is rate-controlling step of the overall kinetics of gradient formation. The quantitative dependence of the thickness of gradient zone on both the key process parameters (atmosphere and time) and the key material variables (Co content and WC grain size) has been obtained. It enables the prediction of the final gradient developed under different heat treatment conditions and in different materials. The simulations were found to agree well with the experimental results.

5.8 References

[1] Fan P, Guo J, Fang ZZ, Prichard P. Metall Mater Trans A 2009;40:1995.

[2] Crank J. Free and moving boundary problems. London: Clarendon Press; 1984.

[3] Ockendon JR, Hodgkins WR. Moving boundary problems in heat flow and diffusion. London: Clarendon Press; 1975.

[4] Zerroukat M, Chatwin CR. Computational moving boundary problems. England: Research Studies Press; 1994.

[5] Burden RL, Faires JD. Numerical Analysis. Florence: Cengage Learning; 2010.

[6] Guillermet AF. Metall Mater Trans A 1989;20A:935.

[7] Sundman B, Jansson B, Andersson JO. CALPHAD: Computer Coupling of Phase Diagrams and Thermochemistry 1985;9:153.

[8] Cermak J, Rollert F, Mehrer H. Metallk 1990;81:81.

[9] Lavergne O, Robaut F, Hodaj F, Allibert CH. Acta Mater 2002;50:1683.

[10] Engstrom A, Hoglund L, Agren J. Metall Mater Trans A 1994;25A:1127.

[11] Frykholm R, Ekroth M, Jansson B, Agren J, Andren HO. Acta Mater 2003;51:1115.

[12] Uhrenius B. Int J Refract Met H 1993;12:121.

[13] Zhou YH, North TH. Model Simul Mater Sci Eng 1993;1:505.

CHAPTER 6

CONCLUSIONS

This dissertation describes the study of thermodynamics and kinetics of an atmosphere heat treatment process for creating Co gradients in WC-Co composites. Both the thermodynamic analysis and the experiments demonstrated that WC-Co with a reduced surface Co content can be produced by heat treating it in a carburizing atmosphere. WC-Co with an enriched surface Co content can be developed through heat treating it in a decarburizing atmosphere. For both the carburization and decarburization process, the temperature must be within the WC-Co(s)-Co(l) coexisting region. The mechanism of the Co gradient formation during the carburization (or the decarburization) process can be summarized as follows: (1) surface carburization (or decarburization) occurs; (2) solid (or liquid) Co in surface region partially or totally transforms to liquid (or solid); (3) liquid Co in surface region increases (or decreases); (4) balance of liquid Co distribution between surface and core regions is broken; (5) liquid Co migrates from surface (or core) region to core (or surface) region; and finally (6) Co gradient forms. The resulted gradient from this process depends on the control of the kinetics of the processes including carbon diffusion and liquid migration.

During the carburization process, the formation of the graded structure strongly depends on the key process parameters (treating atmosphere and holding time) and the key material variables (Co content, WC grain size). It was experimentally shown that

increasing the P_{CH4}/P_{H2}^{2} ratio of the atmosphere or extending the holding time increases the thickness and the amplitude of Co gradients. The thickness of the gradient follows a parabolic law with time, suggesting that the overall kinetics of the process is controlled by the diffusion of carbon in the Co binder phase. Furthermore, the WC-Co material with lower Co content or finer grain size tends to form a gradient with wider thickness and larger amplitude.

The carburizing atmosphere heat treatment process is also feasible for the grain growth inhibitor (Cr_3C_2) doped WC-Co materials as well as straight WC-Co materials. A similar cobalt gradient microstructure can be created within the Cr_3C_2 added WC-Co composites by heat treating the composites in carburizing atmospheres at temperatures within the Co(s)-Co(l)-coexisting phase region. The formation of the Co gradient in W-C-Co-Cr system can be attributed to the same mechanism as proposed for the straight W-C-Co system excluding the possible mechanisms due to grain size gradient and carbon content gradient. Note that the diffusion of carbon accompanies a coupling diffusion of chromium.

A model for simulating the kinetics of the formation of gradient in the carburization process was constructed based on the assumption that the proposed process is diffusion controlled. The governing equations in this model were derived by treating the carburization process as a one-dimensional diffusion-controlled, two-phase moving boundary problem. The governing equations along with the boundary equations were resolved analytically and numerically. Various composition and diffusion parameters involving in this model were obtained through the following two ways: (1) thermodynamic calculations; (2) regression-fit of the simulation results with the

experimental data was used to determine the parameters that were not easily available in literature.

In this model, a quantitative relationship between the atmosphere and the surface carbon concentration was established as follows:

$$[C]_{Surf} = 0.10996 - 0.67219 \cdot P_r + 40.4946 \cdot (P_r)^2$$

where P_r is the $P_{CH4}/P_{H2}{}^2$ ratio of the atmosphere and $[C]_{Surf}$ is the carbon concentration in the Co at the surface. In addition, a quantitative dependence of diffusion coefficient on Co content and WC grain size was established and is given below:

$$D_L^{eff} = \frac{3}{d_{WC}^2 \cdot W_{Co}}$$

where D_L^{eff} is the effective diffusion coefficient in liquid Co phase. d_{WC} and M_{Co} are the grain size and cobalt content of the material, respectively. Using the above equations, we can predict the formation of the gradient as function of process and material factors. The prediction of the gradient thickness agrees well with the experimental results.

Few examples are given in this dissertation to present the application of this research. In fact, the present research is expected to have broad applications within the field of WC-Co as well as similar composite materials. FG WC-Co materials produced using this innovative method are expected to exhibit superior performance in many applications and to have a profound impact on the manufacturing industries that use tungsten carbide tools.

APPENDIX

The numerical algorithm used to solve the differential equations (5.1-5.3) (in Section 5.2) is presented as follows.

A.1 Discretization of Space and Time

In order to compute values of carbon concentration ([C]), the space x and time t need to be discretized as illustrated schematically in Figure A.1. The space domain (x) is divided into N+1 equally spaced subdivisions with interval of length Δx, then we have:

$$\Delta x = L/(N+1) \tag{A.1}$$

$$x_j = j \cdot \Delta x \tag{A.2}$$

where j represents the mesh point within the space grid and j=0, 1, 2, 3, …, N+1. L is the far boundary of the space domain. At any time t, the position of the moving interface M_{II} (as seen in Figure 5.1) should lie in between two neighboring nodes $j=k$ and $j=k$+1 as schematically shown in Figure A.1. k is calculated as

$$k = FIX([S(t)]/\Delta x) \tag{A.3}$$

where *FIX* is a Matlab command to round the element (ie, $[S(t)]/\Delta x$) to the nearest integer. To indicate the positions of interface M_{II} within the two neighboring points, p is calculated as:

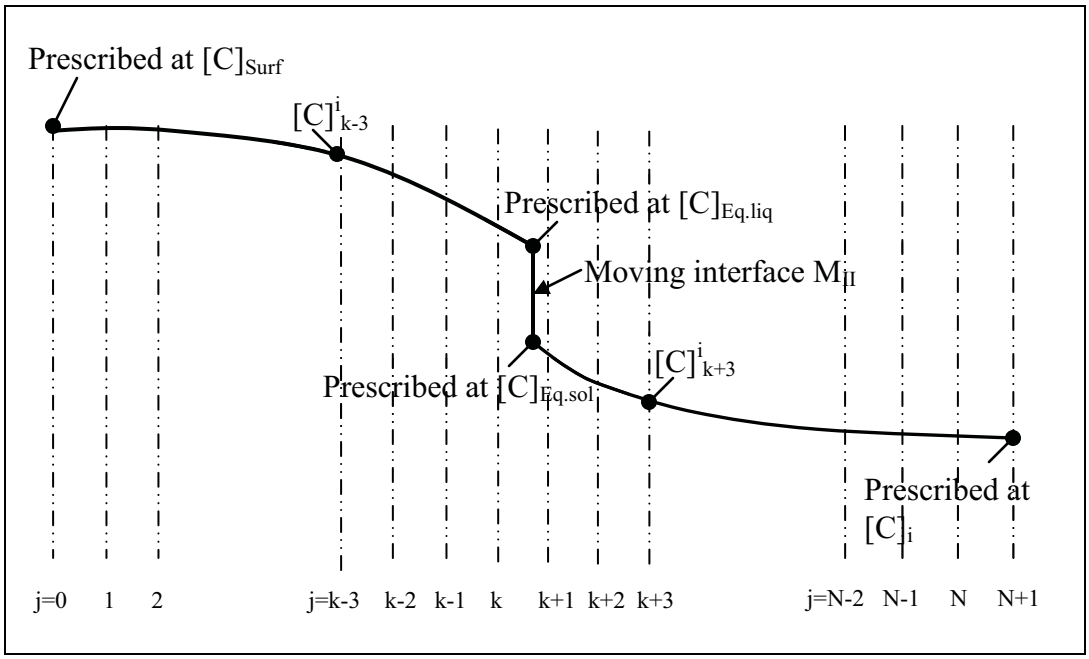

Figure A.1 Schematic illustration of the schemes of discretization.

$$p = \{S(t) - (k-1)\Delta X\} / \Delta X \tag{A.4}$$

where $0 \le p \le 1$.

Time step (Δt) is not a constant varying with the velocity of interface movement at a constant interface displacement, which is expressed as:

$$\Delta t = \frac{E \cdot \Delta x}{dx / dt} \tag{A.5}$$

where E is a constant. Since the interface moves very quickly in the initial period and then slows down, this treatment ensures that the time step will be small enough (in the initial stage) so that the calculation accuracy will be acceptable.

A.2 Approximate Diffusion Equation

The differential diffusion equations (5.1) and (5.2) are approximated by replacing the derivatives with discrete forms of finite difference expressions. To do this, the Lagrangian interpolation algorithm [1] is used. As described in the following section, series of finite difference expressions are derived in terms of position of the interface M_{II}, namely the value of p.

I. If p>0.5 – The finite difference expression for equation (5.1) is obtained as:

$$\frac{[C]_1^{i+1}-[C]_1^i}{\Delta t}=D_L^{eff}\frac{[C]_2^{i+1}-2[C]_1^{i+1}+[C]_{Surf}}{(\Delta x)^2} \tag{A.6}$$

$$\frac{[C]_j^{i+1}-[C]_j^i}{\Delta t}=D_L^{eff}\frac{[C]_{j+1}^{i+1}-2[C]_j^{i+1}+[C]_{j-1}^{i+1}}{(\Delta x)^2} \tag{A.7}$$

$$\frac{[C]_k^{i+1}-[C]_k^i}{\Delta t}=D_L^{eff}\frac{[C]_{Eq.liq}-2[C]_k^{i+1}+[C]_{k-1}^{i+1}}{(\Delta x)^2} \tag{A.8}$$

where i represents the mesh point of time grid. j represents the space grid and j=2, 3, … , k-2, k-1. The finite difference expression for equation (5.2) is given as:

$$\frac{[C]_{k+2}^{i+1}-[C]_{k+2}^i}{\Delta t}=D_S^{eff}\cdot\frac{2}{\Delta x^2}\left(\frac{[C]_{Eq.sol}}{(2-p)(3-p)}-\frac{[C]_{k+2}^{i+1}}{(2-p)}+\frac{[C]_{k+3}^{i+1}}{(3-p)}\right) \tag{A.9}$$

$$\frac{[C]_j^{i+1}-[C]_j^i}{\Delta t}=D_S^{eff}\frac{[C]_{j+1}^{i+1}-2[C]_j^{i+1}+[C]_{j-1}^{i+1}}{(\Delta x)^2} \tag{A.10}$$

$$\frac{[C]_N^{i+1} - [C]_N^i}{\Delta t} = D_S^{eff} \frac{[C]_i - 2[C]_N^{i+1} + [C]_{N-1}^{i+1}}{(\Delta x)^2} \tag{A.11}$$

where the space grid j=k+3, k+4, …, N-1. With the values of $[C]_{k+2}^{i+1}$ and $[C]_{k+3}^{i+1}$, the approximation of $[C]_{k+1}^{i+1}$ can be obtained by the following equation:

$$[C]_{k+1}^{i+1} = \frac{2[C]_{Eq.sol}}{(2-p)(3-p)} + \frac{2(1-p)[C]_{k+2}^{i+1}}{(2-p)} - \frac{(1-p)[C]_{k+3}^{i+1}}{(3-p)} \tag{A.12}$$

II. If p<0.5 – The finite difference expression for equation (5.1) is obtained as:

$$\frac{[C]_1^{i+1} - [C]_1^i}{\Delta t} = D_L^{eff} \frac{[C]_2^{i+1} - 2[C]_1^{i+1} + [C]_{Surf}}{(\Delta x)^2} \tag{A.13}$$

$$\frac{[C]_j^{i+1} - [C]_j^i}{\Delta t} = D_L^{eff} \frac{[C]_{j+1}^{i+1} - 2[C]_j^{i+1} + [C]_{j-1}^{i+1}}{(\Delta x)^2} \tag{A.14}$$

$$\frac{[C]_{k-1}^{i+1} - [C]_{k-1}^i}{\Delta t} = D_L^{eff} \frac{2}{(\Delta x)^2} \left(\frac{[C]_{k-2}^{i+1}}{(2+p)} - \frac{[C]_{k-1}^{i+1}}{(1+p)} + \frac{[C]_{Eq.Liq}}{(1+p)(2+p)} \right) \tag{A.15}$$

where the space grid j=2,3, …, k-1, k-2. The finite difference expression for equation (5.2) is given as:

$$\frac{[C]_{k+1}^{i+1} - [C]_{k+1}^i}{\Delta t} = D_S^{eff} \cdot \frac{[C]_{k+2}^{i+1} - 2[C]_{k+1}^{i+1} + [C]_{Eq.sol}}{\Delta x^2} \tag{A.16}$$

$$\frac{[C]_j^{i+1}-[C]_j^i}{\Delta t}=D_S^{eff}\frac{[C]_{j+1}^{i+1}-2[C]_j^{i+1}+[C]_{j-1}^{i+1}}{(\Delta x)^2} \tag{A.17}$$

$$\frac{[C]_N^{i+1}-[C]_N^i}{\Delta t}=D_S^{eff}\frac{[C]_i-2[C]_N^{i+1}+[C]_{N-1}^{i+1}}{(\Delta x)^2} \tag{A.18}$$

where the space grid j=k+2, k+3, …, N-2, N-1. With the values of $[C]_{k-2}^{i+1}$ and $[C]_{k-1}^{i+1}$, the approximation of $[C]_k^{i+1}$ can be calculated by the following equation:

$$[C]_k^{i+1}=-\frac{p[C]_{k-2}^{i+1}}{(2+p)}+\frac{2p[C]_{k-1}^{i+1}}{(1+p)}+\frac{2[C]_{Eq.liq}}{(2+p)(1+p)} \tag{A.19}$$

A.3 Approximate Interface Equation

Rearranging equation (5.3), it gives:

$$\frac{dS(t)}{dt}=\frac{1}{[C]_{Eq.Liq}-[C]_{Eq.sol}}\left(-D_L^{eff}\frac{\partial[C]_{Liq}}{\partial x}\Big|_{x=S(t)}+D_S^{eff}\frac{\partial[C]_{Sol}}{\partial x}\Big|_{x=S(t)}\right)$$

$$=f[S(t),t] \tag{A.20}$$

The modified Euler's method is applied to solve equation (A.20), namely:

$$S^{n=0}(t+\Delta t)=S(t)+\Delta t\cdot f[S(t),t] \tag{A.21}$$

$$S^{n+1}(t+\Delta t)=S(t)+(\Delta t/2)\cdot\{f[S(t),t]+f[S^n(t+\Delta t),t+\Delta t]\} \tag{A.22}$$

where n represents the series of the iteration and n=0, 1, 2…. The iteration at each time

step is performed until:

$$\left|\frac{S^{n+1}(t+\Delta t)-S^{n}(t+\Delta t)}{S^{n}(t+\Delta t)}\right|<10^{-6} \tag{A.23}$$

$f[S(t),t]$ and $f[S(t+\Delta t),t+\Delta t]$ from equations (A.21) to (A.23) are calculated by the following equations (A.24)-(A.29).

I. If p>0.5 – The mass flux at the interface from the liquid side is calculated as:

$$-D_L^{eff}\left.\frac{\partial[C]_{Liq}}{\partial x}\right|_{x=S(t)}=-\frac{D_L^{eff}}{\Delta x}\left(\frac{p[C]_{k-1}}{1+p}-\frac{(1+p)[C]_k}{p}+\frac{(1+2p)[C]_{Eq.Liq}}{p(1+p)}\right) \tag{A.24}$$

The mass flux at the interface from the solid side is calculated as:

$$-D_S^{eff}\left.\frac{\partial[C]_{Sol}}{\partial x}\right|_{x=S(t)}=-\frac{D_S^{eff}}{\Delta x}\left(\frac{(2p-5)[C]_{Eq.sol}}{(2-p)(3-p)}+\frac{(3-p)[C]_{k+2}}{(2-p)}-\frac{(2-p)[C]_{k+3}}{(3-p)}\right) \tag{A.25}$$

Thus, we have:

$$f[S(t),t]=\frac{1}{[C]_{Eq.Liq}-[C]_{Eq.sol}}(Eq.A.24-Eq.A.25) \tag{A.26}$$

II. If p<0.5 – The mass flux at the interface from the liquid side is calculated as:

$$-D_L^{eff}\left.\frac{\partial[C]_{Liq}}{\partial x}\right|_{x=S(t)}=-\frac{D_L^{eff}}{\Delta x}\left(\frac{(1+p)[C]_{k-2}}{2+p}-\frac{(2+p)[C]_{k-1}}{1+p}+\frac{(3+2p)[C]_{Eq.liq}}{(1+p)(2+p)}\right) \tag{A.27}$$

The mass flux at the interface from the solid side is calculated as:

$$-D_S^{eff}\left.\frac{\partial[C]_{Sol}}{\partial x}\right|_{x=S(t)} = -\frac{D_S^{eff}}{\Delta x}\left(\frac{(2p-3)[C]_{Eq.sol}}{(1-p)(2-p)} + \frac{(2-p)[C]_{k+1}}{(1-p)} - \frac{(1-p)[C]_{k+2}}{(2-p)}\right) \quad \text{(A.28)}$$

Thus, we have:

$$f[S(t),t] = \frac{1}{[C]_{Eq.Liq} - [C]_{Eq.sol}}(Eq.A.27 - Eq.A.28) \quad \text{(A.29)}$$

A.4 Algorithm

The starting point of the position of the interface $S(\Delta t)$ for a very small time step Δt is given as

$$S(\Delta t) = 2\lambda\sqrt{D_L^{eff} \cdot \Delta t} \quad \text{(A.30)}$$

where λ is the same variable as that used in illustrating the analytical method (Section 5.3). It can be calculated using exactly same way as in the analytical method that has been described. The numerical proceeds as follows:

(i) The initial position of the interface is calculated using equation (A.30) and p is determined from equation (A.4). The initial carbon concentration, $[C]_j^i$ (i=1) at each nodal point j is obtained with series of boundary and initial equations as given in Section 5.2.

(ii) The carbon concentration $[C]_j^i$ (i=2) at each nodal point, after the initial interface movement, is calculated using $[C]_j^i$ (i=1) and teh equations (A.6)-(A.19);

(iii) The new moving interface position $S(t+\Delta t)$ is calculated starting from the

previous position $S(t)$ and computed iteratively by the equations (A.21) and (A.22). The iterations will terminate in terms of the equation (A.23);

(iv) The redistribution of carbon concentration $[C]_j^i$ (i>2) from the previous concentrations $[C]_j^{i-1}$ (i>2) at each nodal point j is calculated using equations (A.6)-(A.19);

(v) Steps (iii) and (iv) are repeated until the process is completed.

A.5 References

[1] Burden RL, Faires JD. Numerical Analysis. Florence, KY: Cengage Learning; 2010.